UNIVERSITY OF CALIFORNIA
RIVERSIDE

Titanium Dioxide/Mesoporous Silica Supported Noble Metal Catalysts: Synthesis, Characterization and Catalytic Performance Studies

A Dissertation submitted in partial satisfaction
of the requirements for the degree of

Doctor of Philosophy

in

Materials Science and Engineering

by

Wang Ke

December 2020

Dissertation Committee:
Dr. Francisco Zaera, Chairperson
Dr. Pingyun Feng
Dr. Boniface P. T. Fokwa

The Dissertation of Wang Ke is approved:

_____

_____

_____

Committee Chairperson

University of California, Riverside

ACKNOWLEDGEMENTS

First of all, I would like to express my sincere gratitude to my Ph.D. advisor, Professor Francisco Zaera, for giving me this incredible opportunity to study and do research in his lab. His deep understanding of science, valuable advice and rigor toward research always impress me and help me to make progress. Without his guidance and help, this work would not have been possible.

I would also like to thank Professor Pingyun Feng and Professor Boniface Fokwa for serving as members of my oral exam and final defense committee.

In addition, I would like to thank Dr. Ilkuen Lee for characterizing my TEM and XPS samples, purchasing items, and solving problems for me. I am deeply grateful to all my labmates, including Dr. Xiangdong Qin, Yueqiang, Tianyi, Tongxin, etc., for their kind help. I also want to thank Dan Borchardt for running my NMR samples, Robert M. Palomino and Juan Pablo Simonovis at Brookhaven National Laboratory for measuring my XPS samples, and David H. Lyons for analyzing my ICP samples.

Finally, I would like to express my deepest appreciation to my parents for their endless love and care, as well as emotional and financial support throughout my life. Without them, I would not have made any achievements.

COPYRIGHT ACKNOWLEDGEMENTS

Some of the work in Chapter 3 has been published in Nano Letters. Some of the figures and excerpts have been adapted from the following publications with permission from the copyright owner via RightsLink.

(1) Ke, W.; Liu, Y.; Wang, X.; Qin, X.; Chen, L.; Palomino, R. M.; Simonovis, J. P.; Lee, I.; Waluyo, I.; Rodriguez, J. A.; Frenkel, A. I.; Liu, P.; Zaera, F. Nucleation and Initial Stages of Growth during the Atomic Layer Deposition of Titanium Oxide on Mesoporous Silica. *Nano Lett.* **2020**, *20* (9), 6884–6890.

(2) Zhu, Y.; Zaera, F. Selectivity in the Catalytic Hydrogenation of Cinnamaldehyde Promoted by Pt/SiO2 as a Function of Metal Nanoparticle Size. *Catal. Sci. Technol.* **2014**, *4* (4), 955–962.

(3) Weng, Z.; Chen, Z.; Qin, X.; Zaera, F. Sub-Monolayer Control of the Growth of Oxide Films on Mesoporous Materials. *J. Mater. Chem. A* **2018**, *6* (36), 17548–17558.

ABSTRACT OF THE DISSERTATION

Titanium Dioxide/Mesoporous Silica Supported Noble Metal Catalysts: Synthesis, Characterization and Catalytic Performance Studies

by

Wang Ke

Doctor of Philosophy, Graduate Program in Materials Science and Engineering
University of California, Riverside, December 2020
Dr. Francisco Zaera, Chairperson

Supported noble metal (e.g., Pt and Au) catalysts have been extensively studied in heterogeneous catalysis, since they are of great importance in chemical industries. It has been demonstrated that the metal-oxide interface can create new active sites, modify the electronic properties of the oxide, and further improve the reactivity and selectivity of catalytic reactions. Moreover, the metal catalysts are susceptible to irreversible deactivation through sintering, coking and leaching under reaction conditions. Therefore, we employed Atomic Layer Deposition (ALD) to prepare the TiO_2 films as a protective layer to stabilize the catalysts and enhance the catalytic performance in the meantime.

N_2 adsorption-desorption isotherm analysis proved that the TiO_2 films were grown in a layer-by-layer fashion, and the growth rate is estimated to be approximately 1 Å per cycle. X-ray photoelectron spectroscopy (XPS) results pointed that the titanium was fully oxidized. Infrared absorption spectra showed that new surface sites were created after the

TiO_2 deposition. Nuclear magnetic resonance (NMR) spectra suggested that the ALD process occurs preferentially at isolated silanol groups on SBA-15. Electron paramagnetic resonance (EPR), X-ray diffraction (XRD) and transmission electron microscopy (TEM) data indicated that the TiO_2 films are amorphous and reducible.

The TiO_2 films and noble metal nanoparticles were deposited on SBA-15 in two possible sequences. TEM images confirmed that the Pt nanoparticles were uniformly dispersed in the pores of SBA-15. Infrared absorption spectra showed that active sites for both Pt and TiO_2 are present. The nominal Pt loading (1 wt.%) is very close to the values measured by inductively coupled plasma-optical emission spectrometer (ICP-OES). The TiO_2 loadings are in good agreement with TiO_2/SBA-15 samples. The catalytic performance of supported Pt nanocatalysts was investigated by hydrogenation of cinnamaldehyde (CAL) and CO oxidation reactions. 1-TiO_2/Pt/SBA-15 exhibits relatively the best conversion of CAL and selectivity of cinnamyl alcohol (COL), indicating that the addition of TiO_2 films can improve the selectivity toward COL production. The enhanced catalytic performance is attributed to the creation of acidic sites and the changes of reactant adsorption modes. All the (1-4)-TiO_2/Pt/SBA-15 and Pt/(1-4)-TiO_2/SBA-15 samples show higher reactivity than Pt/SBA-15, suggesting the addition of TiO_2 can promote CO oxidation. Oxygen vacancies created in the interface between the reducible TiO_2 films and Pt nanoparticles is responsible for the enhanced reaction rate. The stability of the catalysts were investigated by running the hydrogenation reaction continuously for 3 times. The Pt nanoparticles were still well-dispersed in the pores of SBA-15, and no nanoparticle sintering was observed after 3 cycles

of reaction in the TEM images. The enhanced stability is possibly due to (1) encapsulation of Pt nanoparticles inside SBA-15; (2) ALD-TiO_2 protective layer; (3) SMSI effect.

The supported Au nanocatalysts were synthesized using a gold cationic complex precursor-$Au(en)_2Cl_3$. Characterization results and kinetic data of hydrogenation of CAL reaction are similar to Pt catalysts. Oxidation of benzyl alcohol was studied for Au catalysts. Although the selectivity toward benzaldehyde was not greatly improved after the addition of TiO_2, the stability of the Au/TiO_2/SBA-15 and TiO_2/Au/SBA-15 samples was still excellent.

Table of Contents

Chapter 1 Introduction 1

1.1 Noble metal nanocatalyst 1

1.2 Metal-oxide interface 2

1.3 Atomic layer deposition (ALD) 4

1.4 Catalytic reactions 5

Chapter 2 Instrumentation and catalyst characterization 7

2.1 Chemical reagents 7

2.2 ALD reactor 8

2.3 Catalyst characterization 9

2.3.1 Transmission electron microscope (TEM) 9

2.3.2 Fourier transform infrared spectroscopy (FTIR) 9

2.3.3 Inductively coupled plasma optical emission spectrometry (ICP-OES) 10

2.3.4 Adsorption-desorption isotherm analysis 11

2.3.5 X-ray photoelectron spectroscopy (XPS) 11

2.3.6 Electron paramagnetic resonance (EPR) 11

2.3.7 X-ray diffraction (XRD) 12

2.3.8 Nuclear magnetic resonance (NMR) 12

2.4 Catalytic test 12

Chapter 3 Atomic layer deposition of TiO_2 13

3.1 Introduction 13

3.2 Experimental 13

3.2.1 Deposition of TiO_2 film on SBA-15 13

3.2.2 Synthesis of porous TiO_2 by sol-gel method 13

3.3 Results and discussion 14

3.4 Conclusions 26

Chapter 4 Synthesis, characterization and catalytic performance studies of supported Pt nanocatalysts 27

4.1 Introduction 27

4.2 Experimental 28

4.2.1 Synthesis of Pt/SBA-15 28

4.2.2 Synthesis of TiO_2/Pt/SBA-15 28

4.2.3 Synthesis of Pt/TiO_2/SBA-15 28

4.2.4 Synthesis of Pt/TiO_2-P25 and Pt/TiO_2 (sol-gel) 28

4.2.5 Hydrogenation of cinnamaldehyde 29

4.2.6 CO oxidation 29

4.3 Results and discussion 32

4.3.1 Characterization of Pt/SBA-15 and removal of PVP 32

4.3.2 Characterization of (1-4)-TiO_2/Pt/SBA-15 and Pt/(1-4)-TiO_2/SBA-15 36

4.3.3 Hydrogenation of cinnamaldehyde 48

4.3.4 CO oxidation 57

4.4 Conclusions 58

Chapter 5 Synthesis, characterization and catalytic performance studies of supported Au nanocatalysts 61

5.1 Introduction 61

5.2 Experimental 61

5.2.1 Synthesis of bis(ethylenediamine) gold (III) chloride - $Au(en)_2Cl_3$ 61

5.2.2 Synthesis of Au/SBA-15 and Au/(1-4)-TiO_2/SBA-15 62

5.2.3 Synthesis of (1-4)-TiO_2/Au/SBA-15 62

5.2.4 Synthesis of Au/TiO_2 (sol-gel) 62

5.2.5 Functionalization of SBA-15 with APTES 62

5.2.6 Synthesis of Au/SBA-15 with APTES functionalized SBA-15 63

5.2.7 Synthesis of Au/SBA-15 with $NaBH_4$ as reducing agent 63

5.2.8 Hydrogenation of CAL 63

5.2.9 Oxidation of benzyl alcohol 63

5.3 Results and discussion 64

5.3.1 Characterization of (0-4)-TiO_2/Au/SBA-15 and Au/(1-4)-TiO_2/SBA-15 64

5.3.2 Hydrogenation of cinnamaldehyde 74

5.3.3 Oxidation of benzyl alcohol 78

5.3.4 Size control of Au nanoparticle 83

5.4 Conclusions 85

Chapter 6 Conclusions and future works 87

6.1 Conclusions 87

6.2 Future works 90

References 91

List of Figures

Figure 3.1 (a) N_2 adsorption-desorption isotherms. (b) Pore size distributions, (c) pore diameter <d>, and pore volume V, estimated from adsorption branch. (d) Pore size distributions, (e) <d>, V, and surface area A, estimated from desorption branch. Data are reported as a function of the number of ALD cycles used. 16

Figure 3.2 CO IR absorption spectra of (a) 1-TiO_2/SBA-15, (b) 2-TiO_2/SBA-15, (c) 3-TiO_2/SBA-15, (d) 4-TiO_2/SBA-15. (e) Peak intensities versus temperature. 17

Figure 3.3 (a, c) Pyridine IR absorption spectra of (0-10)-TiO_2/SBA-15. (b, d) Peak intensities versus temperature before and after annealing at 150 ^oC. 19

Figure 3.4 XPS spectra of (a) Ti 2p and (b) O 1s of (0-10)-TiO_2/SBA-15..... 20

Figure 3.5 ^{29}Si NMR spectra of (a) SBA-15, (b) 2-TiO_2/SBA-15, (c) 4-TiO_2/SBA-15 and (d) 10-TiO_2/SBA1-5. (e) Peak intensities versus ALD cycles. (f) Peak assignments and structures of various silica species. 22

Figure 3.6 (a) XRD patterns of TiO_2-P25, 10-TiO_2/SBA-15 calcined at 800 ^oC, 10-TiO_2/SBA-15 and TiO_2 (sol-gel). (b) TEM image of 10-TiO_2/SBA-15 calcined at 800 ^oC. 23

Figure 3.7 EPR spectra of 4-TiO_2/SBA-15 (left), TiO_2-P25 (center), and TiO_2 (sol-gel) (right). From bottom to top are fresh, calcined under H_2, and calcined under H_2 followed by O_2 samples, respectively. 25

Figure 4.1 Synthetic approaches. 27

Figure 4.2 CO_2 calibration curve. 31

Figure 4.3 (a) C 1s and (b) N 1s XPS spectra of Pt/SBA-15 after calcination. 32

Figure 4.4 (a) N_2 adsorption-desorption isotherms. (b) Pore size distributions from desorption branch of SBA-15 and Pt/SBA-15 before and after calcination. 33

Figure 4.5 (a) TEM image. (b) Pt nanoparticle size distributions of Pt/SBA-15 after calcination. 34

Figure 4.6 (a) CO IR absorption spectra of Pt/SBA-15, and (b) peak intensities versus temperature after calcination..... 35

Figure 4.7 (a, b) N_2 adsorption-desorption isotherms. (c, d) Pore size distributions, (e, f) <d>, V, and A, estimated from desorption branch, of (1-4)-TiO_2/Pt/SBA-15 and Pt/(1-4)-TiO_2/SBA-15. Pt/SBA-15 and (1-4)-TiO_2/SBA-15 are used as reference samples. Data are reported as a function of the number of ALD cycles used..... 37

Figure 4.8 TEM images and Pt nanoparticle size distributions of (a, b) 1-TiO_2/Pt/SBA-15, (c, d) 2-TiO_2/Pt/SBA-15, (e, f) 3-TiO_2/Pt/SBA-15, and (g, h) 4-TiO_2/Pt/SBA-15..... 38

Figure 4.9 TEM images and Pt nanoparticle size distributions of (a, b) Pt/1-TiO_2/SBA-15, (c, d) Pt/2-TiO_2/SBA-15, (e, f) Pt/3-TiO_2/SBA-15, and (g, h) Pt/4-TiO_2/SBA-15..... 39

Figure 4.10 (a) HAADF image. EDS mapping images of Pt (b), Si (c) and Ti (d) of 1-TiO_2/Pt/SBA-15. 41

Figure 4.11 (a) HAADF image. EDS mapping images of Pt (b), Si (c) and Ti (d) of Pt/1-TiO_2/SBA-15. 42

Figure 4.12 CO IR absorption spectra of (1-4)-TiO_2/Pt/SBA-15 (a to d). Peak intensities versus temperature (e, f). 44

Figure 4.13 CO IR absorption spectra of Pt/(1-4)-TiO_2/SBA-15 (a to d). Peak intensities versus temperature (e, f). 45
Figure 4.14 Reaction pathways of hydrogenation of CAL. 49
Figure 4.15 % Conversion of CAL (a), % selectivity of HCAL (b), HCOL (c), and COL (d) versus reaction time. 49
Figure 4.16 % Selectivity of HCAL, HCOL and COL of various catalysts at t=300 min. 51
Figure 4.17 Selectivity versus conversion of various catalysts. 52
Figure 4.18 TOFs (a, c and e) and TONs (b, d and f) of HCAL, HCOL and COL for various catalysts as a function of reaction time. 53
Figure 4.19 (a) TEM image. (b) Pt nanoparticle size distributions of 1-TiO_2/Pt/SBA-15 after 3 catalytic runs. 55
Figure 4.20 % Conversion of CAL (a), % selectivity of HCAL (b), HCOL (c), and COL (d) versus reaction time of 1-TiO_2/Pt/SBA-15 for 3 catalytic runs. 56
Figure 4.21 TOFs (a, c) and TONs (b, d) of CAL and COL versus reaction time of 1-TiO_2/Pt/SBA-15 for 3 catalytic runs. 57
Figure 4.22 (a) TOFs and (b) TONs for CO oxidation versus reaction time. 58
Figure 5.1 (a, b) N_2 adsorption-desorption isotherms. (c, d) Pore size distributions, (e, f) <d>, V, and A, estimated from desorption branch, of (1-4)-TiO_2/Au/SBA-15 and Au/(1-4)-TiO_2/SBA-15. SBA-15, Au/SBA-15 and (1-4)-TiO_2/SBA-15 are used as reference samples. Data are reported as a function of the number of ALD cycles used. 65
Figure 5.2 (a) TEM image. (b) Au nanoparticle size distributions of Au/SBA-15. 66

Figure 5.3 TEM images and Au nanoparticle size distributions of (a, b) 1-TiO_2/Au/SBA-15, (c, d) 2-TiO_2/Au/SBA-15, (e, f) 3-TiO_2/Au/SBA-15 and (g, h) 4-TiO_2/Au/SBA-15. 67

Figure 5.4 TEM images and Au nanoparticle size distributions of (a, b) Au/1-TiO_2/SBA-15, (c, d) Au/2-TiO_2/SBA-15, (e, f) Au/3-TiO_2/SBA-15 and (g, h) Au/4-TiO_2/SBA-15. 68

Figure 5.5 (a) CO IR absorption spectrum of Au/SBA-15. (b) Peak intensities versus temperature. 69

Figure 5.6 CO IR absorption spectra of (1-4)-TiO_2/Au/SBA-15 (a to d). Peak intensities versus temperature (e, f). 70

Figure 5.7 CO IR absorption spectra of Au/(1-4)-TiO_2/SBA-15 (a to d). Peak intensities versus temperature (e, f). 71

Figure 5.8 % Conversion of CAL (a), % selectivity of HCAL (b), HCOL (c), and COL (d) versus reaction time. 74

Figure 5.9 % Selectivity of HCAL, HCOL and COL of various catalysts at t=300 min. 75

Figure 5.10 Selectivity versus conversion of various catalysts. 76

Figure 5.11 TOFs (a, c and e) and TONs (b, d and f) of HCAL, HCOL and COL for various catalysts as a function of reaction time. 77

Figure 5.12 (a) % Conversion of benzyl alcohol versus reaction time. (b) % Selectivity of benzaldehyde at t=360 min. 79

Figure 5.13 (a) TOFs and (b) TONs of benzaldehyde. 80

Figure 5.14 (a) % Conversion of benzyl alcohol. TOFs and TONs of benzyl alcohol (b, c) and benzaldehyde (d, e) versus reaction time of Au/4-TiO_2/SBA-15 for 3 catalytic runs. 81

Figure 5.15 (a) TEM image. (b) Au nanoparticle size distributions of Au/4-TiO_2/SBA-15 after 3 catalytic runs. 82

Figure 5.16 TEM images of (a) Au/SBA-15 and (b) 2-TiO_2/Au/SBA-15 after 3 catalytic runs. 82

Figure 5.17 TEM images and Au nanoparticle size distributions of Au/SBA-15 functionalized with APTES (a, b) and reduced by $NaBH_4$ (c, d) 84

List of Tables

Table 3.1 TiO_2 loadings of (1-4)-TiO_2/SBA-15 26

Table 4.1 Summary of surface areas, pore volumes and pore diameters of SBA-15, Pt/SBA-15 before and after calcination 33

Table 4.2 Pt and TiO_2 loadings of Pt/SBA-15, (1-4)-TiO_2/Pt/SBA-15 and Pt/(1-4)-TiO_2/SBA-15 47

Table 4.3 EDS elemental analysis of 1-TiO_2/Pt/SBA-15 48

Table 4.4 EDS elemental analysis of Pt/1-TiO_2/SBA-15 48

Table 5.1 Au and TiO_2 loadings of Au/SBA-15, (1-4)-TiO_2/Au/SBA-15 and Au/(1-4)-TiO_2/SBA-15 73

Chapter 1 Introduction

1.1 Noble metal nanocatalyst

Heterogeneous catalysis plays an important role in the manufacture of essential products in the fields of chemical industry, agriculture and pharmaceuticals. It is estimated that more than 20% of the gross national product (GNP) of industrial countries relies in one way or another on catalysis[1,2]. One of the major challenges in heterogeneous catalysis is to be able to design and develop highly stable and selective catalysts. As an important type of heterogeneous catalysts, noble metal (e.g., Pt, Au, Pd and Ag) catalysts have been extensively applied in many important reactions such as partial oxidation[3], selective hydrogenation[4], C-C coupling reaction[5], etc. Thanks to the advent of nanoscience and nanotechnology, a lot of efforts have been made towards the rational design of noble metal nanoparticle catalysts, owing to their high surface-to-volume ratio and high density of active sites compared to the bulk materials[6,7].

Despite their promising catalytic activity, noble metal nanoparticles often suffer from coking, leaching and sintering under high temperature and high pressure conditions. To prevent sintering of nanoparticles, an effective approach is to encapsulate the nanoparticles into mesoporous silica, such as MCM-41 or SBA-15, because the interior mesoporous structure can nanoconfine the size of metal nanoparticles and inhibit their aggregation and further growth[8,9].

As a subset of noble metals, finely divided platinum nanoparticles show excellent catalytic activity for various reactions, such as CO/NO_x oxidation[10], hydrogenation of alkene[11], oxidation of alcohol[12], etc. It is also the most effective electrocatalyst for the oxygen reduction reaction (ORR)[13]. Moreover, great effort has been made to prepare shape and size controllable Pt nanoparticles with improved reactivity and selectivity[14,15]. Gold was once considered to be chemically inert and is generally regarded as a poor catalyst. However, when Au nanoparticles are deposited on metal oxides, they become surprisingly active for oxidation and hydrogenation reactions[16–18].

1.2 Metal-oxide interface

Strong metal-support interaction (SMSI) effect was introduced by Tauster et al. in 1970s to describe the drastic changes in the chemisorption properties of group 8 metals supported on titanium dioxide after high temperature reduction[19]. The SMSI effect suppresses the activity for alkane hydrogenolysis; however, this effect also shows enhanced activity for the reaction of CO with H_2 to form methane or higher hydrocarbons[20]. It has been proven by electron microscopic and in situ spectroscopic techniques that the reduced titania (TiO_x) species migrate onto the surface of metals, and there are strong bondings formed and charge transfer between the metal and oxide[21,22]. Furthermore, the surface and interfaces of catalysts are of great importance for heterogeneous catalysis as they are often considered to be active sites for catalytic reactions. One versatile way to create new active sites is by exploiting the interface of metal-oxide. The unique geometric and electronic properties between metal and oxide may provide new acidic sites and display enhanced reactivity and

selectivity toward specific reactions. Therefore, in the past decades, even though the mechanism of interfacial structure-catalytic performance correlation is not fully understood, the noble metal nanoparticles supported on reducible oxide (e.g., TiO_2, CeO_2 and Fe_3O_4) catalyst has been widely used in many reactions, such as CO oxidation[23,24], water-gas shift (WGS) reaction[25,26] and CO_2 hydrogenation reaction[27]. Rodriguez and co-workers have demonstrated that Au surfaces partially covered by ceria or titania nanoparticles have activities comparable to those of good WGS catalysts such as Cu (111) or Cu (100), even though clean Au (111) is not catalytically active for the WGS[28]. Accordingly, employing reducible oxide is of great importance, because their oxygen storage capacity and oxygen vacancies created at the metal-oxide interface can promote the reactivity.

Moreover, previous research has primarily targeted three major causes for deactivation: sintering, leaching and coking[29,30]. Metal nanoparticles have high surface energy, and thus tend to sinter and form large particles under high temperature reaction conditions. Also, leaching always occurs in liquid phase reactions, and coke blocks the catalytic active sites due to carbon deposition. To improve the stability of catalysts, depositing a protective oxide layer has been proven to be an effective approach, because the oxide layer can immobilize the metal nanoparticles and strengthen the interaction between the metal and support[31,32]. Stair and co-workers showed that 45 layers of Al_2O_3 overcoated Pd/Al_2O_3 catalyst can effectively reduce deactivation by coking and sintering in oxidative dehydrogenation of ethane to ethylene. No visible morphology change can be observed for the $45Al_2O_3/Pd/Al_2O_3$ catalyst after reaction at 675 ^oC for 28 hours[33]. Dumesic and co-

workers employed similar method to stabilize Cu/Al_2O_3 catalyst for liquid-phase reactions. The particle size and loading of Cu did not change before and after three cycles of reaction[34].

1.3 Atomic layer deposition (ALD)

ALD is a vapor phase technique capable of producing thin films of a variety of materials. In ALD, the deposition process is split into two sequential, self-limiting half reactions in order to provide a better handle on the thickness, conformality and uniformity of the grown films. ALD is considered the deposition method with the greatest potential for the production of thin films, offering many advantages over other chemical vapor deposition (CVD) or physical vapor deposition (PVD) techniques: (1) precise thickness control at the Ångstrom or monolayer level by tailoring the number of ALD cycles; (2) conformality of high aspect ratio and three dimensionally-structured materials[35–37].

As discussed already, introducing an oxide layer on supported metal catalysts is critical. Some solution chemistries have been developed for the deposition of oxide films on the surface of porous supports; however, these offer only limited control on the characteristics of the resulting deposited films in terms of either thickness or atomic distribution[38–40]. In contrast, ALD can achieve atomically-precise thickness control of the oxide layer. Moreover, since the ALD processes are always conducted at relatively low temperatures, it can be anticipated that the oxide films will be amorphous and reducible[41]. Therefore, some new active sites may be prepared this way, and charge transfer might also occur across the interface, and then lead to enhanced reactivity and selectivity.

1.4 Catalytic reactions

Selective hydrogenation of α, β-unsaturated aldehydes to α, β-unsaturated alcohols is an important class of reactions, because the desired products (unsaturated alcohols) are widely employed in the manufacture of pharmaceuticals, perfumes and fragrances. However, from both thermodynamic (the bond energy is 715 kJ/mol for C=O and 615 kJ/mol for C=C) and kinetic point of view, the hydrogenation of C=C bond is favored over the C=O bond[42]. Thus, the selective hydrogenation of the C=O bond remains a great challenge. Metal nanoparticles supported on reducible oxides may be a promising catalyst for selective hydrogenation of α, β-unsaturated aldehyde, because the geometric and electronic structures are modified through SMSI effect. The migration of reduced oxides onto metal nanoparticles could suppress the adsorption of the C=C group, and the reduced cation could serve as Lewis acid sites and increase the selectivity[43,44].

Selective oxidation of alcohols to aldehydes/ketones have been extensively studied, because the desired products are valuable intermediates of plastics, detergents, paints, cosmetics and food additives[45,46]. Many oxidations of this type were carried out using stoichiometric oxidants, such as chromate or permanganate, but they are expensive and often produce large amounts of toxic waste[47,48]. Therefore, development of heterogeneous catalysts, and the use of molecular O_2 as the oxidant are of great interest.

Catalytic CO oxidation has been extensively studied in recent years, due to its wide industrial applications, such as pollution reduction in the automotive industry, sensors, gas masks, CO_2 lasers, fuel cells, etc.[49,50]. Furthermore, CO oxidation serves as a prototypical reaction for heterogeneous catalysis. Noble metal nanoparticles supported on reducible

oxides catalysts have been shown substantially enhanced catalytic performance for CO oxidation, as a large amount of oxygen vacancies is created at the perimeter interface[51,52], which can greatly promote the reaction.

Chapter 2 Instrumentation and catalyst characterization

2.1 Chemical reagents

The following chemicals were used as purchased without further purification: (3-Aminopropyl)triethoxysilane (APTES, Sigma-Aldrich, 99%), benzaldehyde (Sigma-Aldrich, ≥99.9%), benzyl alcohol (Alfa Aesar, 99+%), benzoic acid (Sigma-Aldrich, ≥99.5%), chloroplatinic acid hexahydrate ($H_2PtCl_6 \cdot 6H_2O$, Strem chemicals, 99.9%), dodecane (Sigma-Aldrich, ≥99%), ethanol (Koptec 200 proof pure ethanol), ethylenediamine (Sigma-Aldrich, ≥99%), gold(III) chloride trihydrate ($HAuCl_4 \cdot 3H_2O$, Sigma-Aldrich, ≥99.9%), hydrochloric acid (Fisher chemical, 36.5-38.0%), 2-propanol (Fisher chemical, ≥99.5%), nitric acid (Fisher chemical, 70%), polyvinylpyrrolidone (PVP, Sigma-Aldrich, average molecular weight 10000), SBA-15 (ACS material), sodium borohydride (Sigma-Aldrich, 99%), sodium hydroxide (Fisher chemical, ≥97%), sulfuric acid (Fisher chemical, 95-98%), tetrabutyl orthotitanate (Sigma-Aldrich, ≥97.0%), tetrakis(dimethylamido)titanium(IV) (TDMAT, Strem chemicals, 99%), titanium(IV) oxide (Aeroxide P25, Acros organics, ≥99.5%), toluene (Fisher chemical, ≥99.5%), *trans*-cinnamaldehyde (Sigma-Aldrich, 99%), urea (Sigma-Aldrich, 99.0-100.5%).

Carbon dioxide (99.8%) and carbon monoxide (99.9%) were purchased from Matheson. Oxygen, hydrogen, nitrogen, air and liquid nitrogen were purchased from Airgas.

2.2 ALD reactor

The ALD experiments were carried out in a homemade ALD reactor made out of a six-way stainless steel cross sealed with 2.75 inches Conflat flanges. The main reaction chamber can be heated to temperatures of up to 400 K by using a set of heating tapes wrapped around its outside. The powder sample is placed in a holder consisting of a 3 × 2 cm^2 shallow tray, ~5 mm deep, made out of a Ni sheet. This holder can be heated resistively by passing current through appropriate feedthroughs connected to a pair of supporting Ni wires. The powder is spread on the tray to form a layer approximately 1 mm in depth, and covered with a tightly fitted lid made out of a stainless steel wire mesh to hold it in place and prevent it from being blown away during pumping and purging. The temperature of the sample holder is monitored with a K-type thermocouple wire pair spotwelded to the backside of the tray, and set independently from that of the chamber by using a separate controller. Powder samples can be heated with this arrangement to temperatures of up to 625 K during the depositions.

Two independent precursors and purging gas delivery lines are attached to two of the flanges bolted to the reaction chamber. Two precursors with high vapor pressures and purging gases are all fed to the system directly. The reactor can be evacuated using a mechanical pump connected to the six-way cross via a 1.5 inches right-angle valve, and typically reaches ultimate pressures of around or below 5 mTorr, as measured by a thermocouple gauge. In a typical ALD cycle, the chemicals are fed into the chamber in sequence, with purging cycles performed in between, while maintaining continuous pumping.

2.3 Catalyst characterization

2.3.1 Transmission electron microscope (TEM)

Around 1 mg of TEM sample was added in around 1 mL of ethanol in a centrifuge tube. The suspension was sonicated for a while until the particles were uniformly dispersed, and then the suspension was added onto a TEM copper grid (Formvar/Carbon on 400 Mesh Copper) dropwise on the dark side with a filter paper underneath. The sample was ready for analysis once the ethanol was completely evaporated under ambient conditions. TEM characterization was performed using a FEI Titan Themis 300 scanning transmission electron microscope (STEM). The energy-dispersive spectroscopy (EDS) data were obtained using a Bruker Quantax detector. The nanopaticle size distribution was estimated by calculating the average diameter of 100 nanopaticles on the images.

2.3.2 Fourier transform infrared spectroscopy (FTIR)

The CO and pyridine adsorption experiments were carried out in transmission mode using a Bruker Tensor 27 FTIR spectrometer and a homemade quartz cell with NaCl windows capable of working at any temperature between -150 ^{o}C and 350 ^{o}C and at any pressure between 0.01 and 760 Torr.

For the CO adsorption experiment, approximately 10 mg of the catalysts were pressed into a self-supporting 13 mm diameter disc and placed inside the central holder of the reactor. They were dried at 150 ^{o}C for 2 h in situ under vacuum inside the transmittance IR cell, and pre-treated by following two alternating oxidizing and reducing cycles at 350 ^{o}C, under 200 Torr of O_2 and 200 Torr of H_2, respectively, for 1 h each. Each catalyst disk was studied individually by cooling it down to below -150 ^{o}C and exposing it to 20 Torr of CO for 10

min, after which the cell was evacuated. Transmission IR spectra were taken at 10 ^{o}C intervals while warming the sample until reaching a temperature of 350 ^{o}C. The IR spectra of the adsorbed CO were recorded at a resolution of 4 cm^{-1} using a mercury-cadmium-telluride (MCT) detector, and referenced to background traces recorded under similar conditions before CO adsorption.

The pyridine adsorption experiment followed the same sample preparation procedure. Whereas the disk was pre-treated at 350 ^{o}C under 200 Torr of H_2 for 1 h in situ in the IR cell under vacuum. The cell was evacuated, and background spectrum was recorded before introducing pyridine. After the catalyst was exposed to 20 Torr of pyridine vapor, the IR spectra were taken at 25 ^{o}C before and after annealing at 150 ^{o}C for 1 h.

2.3.3 Inductively coupled plasma optical emission spectrometry (ICP-OES)

The metal (Pt, Au and Ti) loadings were quantified by a Perkin-Elmer Optima 7300DV ICP-OES system.

The Pt or Au ICP sample was prepared as follows. 3 mg of sample was weighed out, and dissolved in 20 mL of aqua regia solution. The suspension was heated at 80 ^{o}C for 30 min, and 120 ^{o}C for 1.5 h. After cooled down to room temperature, the suspension was filtered and rinsed at least three times. The clear solution was transferred to a 100 mL volumetric flask, and diluted to the mark with deionized (DI) water.

The Ti ICP sample was prepared by suspending 2 mg of sample in 10 mL of concentrated H_2SO_4 solution and heating at 205 ^{o}C for 2 h, since hot concentrated H_2SO_4 is capable of dissolving TiO_2. After filtration, the solution was quantitatively diluted to a 500 mL volumetric flask.

2.3.4 Adsorption-desorption isotherm analysis

N_2 adsorption-desorption isothermal measurements were performed using a Quantachrome NOVA@2000e gas sorption system. Pore diameter and pore volume were estimated using the BJH (Barrett-Joyner-Halenda) equations, whereas surface areas were calculated using the BET (Brunauer-Emmett-Teller) isotherm.

2.3.5 X-ray photoelectron spectroscopy (XPS)

XPS analysis for Pt/SBA-15 was conducted using a Kratos Analytical AXIS Ultra Delay-Line Detector (DLD) Imaging XPS system, equipped with an Al K_α monochromated X-ray source and a 165-mm mean radius electron energy hemispherical analyzer. The powder sample was pressed into disc, and mounted on carbon tapes for analysis.

XPS spectra for TiO_2/SBA-15 were obtained using a Specs Gmbh spectrometer under ultra-high vacuum (UHV) conditions (10^{-9} to 10^{-10} Torr), equipped with a Phoibos 1509MCD energy analyzer and Mg K_α radiation, at the Chemistry Division of Brookhaven National Laboratory.

2.3.6 Electron paramagnetic resonance (EPR)

The EPR analysis was carried out using a Bruker EMX EPR spectrometer equipped with a Bruker ER 4102ST cavity. Around 1 mg of sample was placed in a capillary glass tube. Then the capillary was sealed with parafilm and placed in the cavity for analysis. The center field was set as 3330 G, and the sweep width was set as 100 G. The measurement was performed at 100 K.

2.3.7 X-ray diffraction (XRD)

XRD analysis was performed using a PANalytical Empyrean Series 2 diffractometer with Cu K_α radiation (λ=1.5418 Å) with 45 kV and 40 mA.

2.3.8 Nuclear magnetic resonance (NMR)

The solid state ^{29}Si NMR spectra were obtained using a Bruker NEO 600MHz NMR spectrometer with Bruker 4 mm CP-MAS 1H/BB probe.

2.4 Catalytic test

The liquid phase hydrogenation of unsaturated aldehydes and oxidation of alcohols were carried out in a 4560 Parr bench top reactor. The aliquots were analyzed using an Agilent 6890N gas chromatograph (GC) with an HP-50 column (15 m × 320 μm × 0.25 μm) to determine their composition.

Chapter 3 Atomic layer deposition of TiO_2

3.1 Introduction

In this chapter, TiO_2 films were deposited onto mesoporous SBA-15 via ALD. N_2 adsorption-desorption isotherms were primarily used to characterize the mesoporous structure of the deposited TiO_2/SBA-15. The TiO_2 loadings were estimated by ICP-OES. EPR and XRD were used to demonstrate the redox properties and amorphous structure of the TiO_2 films. XPS and NMR spectra were utilized to investigate the surface properties of the TiO_2 films, including the Ti valence and O bondings, and the surface OH groups. IR absorption spectroscopy using CO and pyridine as probes was employed to identify the active sites on the surface.

3.2 Experimental

3.2.1 Deposition of TiO_2 film on SBA-15

The TiO_2 ALD experiment was carried out in the ALD reactor. TDMAT and DI water were dosed alternatively with N_2 purging in between. ALD cycle times were TDMAT: N_2: H_2O: N_2 = 20 min: 50 min: 2 min: 50 min. The temperatures of the sample holder, reactor and TDMAT were 100 ^oC, 100 ^oC and 40 ^oC, respectively.

3.2.2 Synthesis of porous TiO_2 by sol-gel method

10 mL of tetrabutyl orthotitanate was added to 100 mL DI water dropwise, and the mixture was stirred for 4 h at room temperature. Then the water was removed by rotary evaporator at 50 ^oC, and the powder was calcined at 150 ^oC for 6 h[53].

The 10-TiO_2/SBA-15 was calcined under air for 24 h for XRD and TEM measurements.

3.3 Results and discussion

The quality of the TiO_2 films grown by ALD was primarily investigated by the analysis of N_2 adsorption-desorption isotherms. All the isotherms (Figure 3.1a) are typical type IV isotherms, according to International Union of Pure and Applied Chemistry (IUPAC) nomenclature. The shape of the hysteresis loop is not affected by the TiO_2 deposition even after 10 ALD cycles, indicating that the TiO_2/SBA-15 retains the mesoporous structure. Furthermore, the total amount of nitrogen consumed, which is determined by the value at P/P_0=1, decreases with the number of ALD cycles used. This reflects that the deposited films reduce the empty volume inside the pores. Finally, the shift of the hysteresis loop toward lower pressures with increasing number of ALD cycles manifests that the condensation occurs at lower pressures because the pores are smaller.

Figure 3.1b and d show the pore size distributions extracted from BJH equations from the adsorption and desorption branches, respectively. Although the qualitative trends are similar in both cases, the values of the pore diameter in each case are different. For mesoporous SBA-15, it is suggested that the data from the desorption branch may better represent the actual pore diameter and pore volume[54]. In Figure 3.1b and d, the average pore diameters decrease monotonically with increasing number of ALD cycles. More importantly, the pore size distributions are narrow and well defined in general.

Figure 3.1c and e exhibit the geometrical parameters, including pore diameters, pore volumes, and surface areas, as a function of the numbers of ALD cycles used. The pore

diameters decrease linearly with increasing number of ALD cycles, suggesting the layer-by-layer growth of the films. It is estimated that the TiO_2 films thickness is approximately 1 Å per cycle.

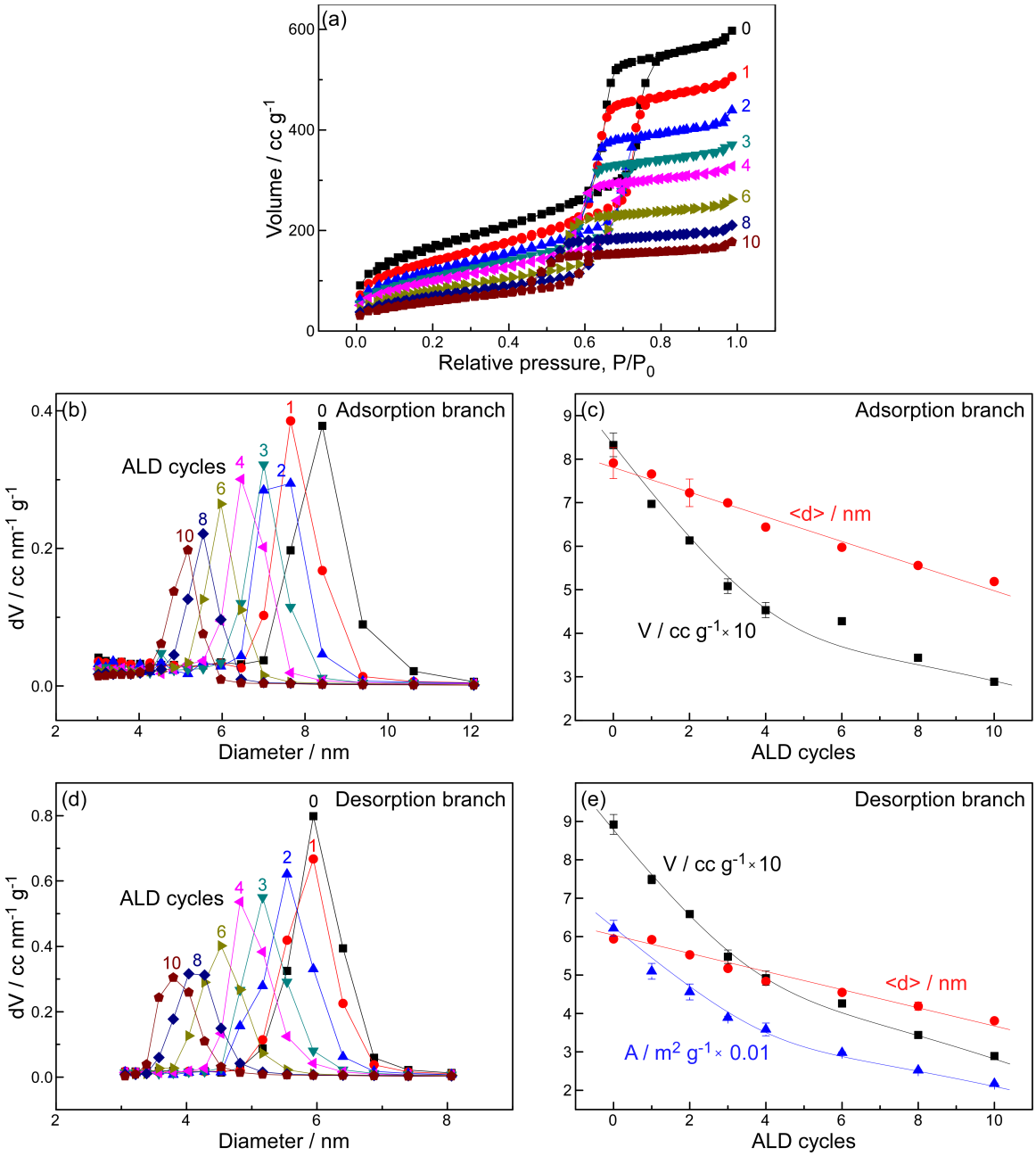

Figure 3.1 (a) N_2 adsorption-desorption isotherms. (b) Pore size distributions, (c) pore diameter <d>, and pore volume V, estimated from adsorption branch. (d) Pore size distributions, (e) <d>, V, and surface area A, estimated from desorption branch. Data are reported as a function of the number of ALD cycles used.

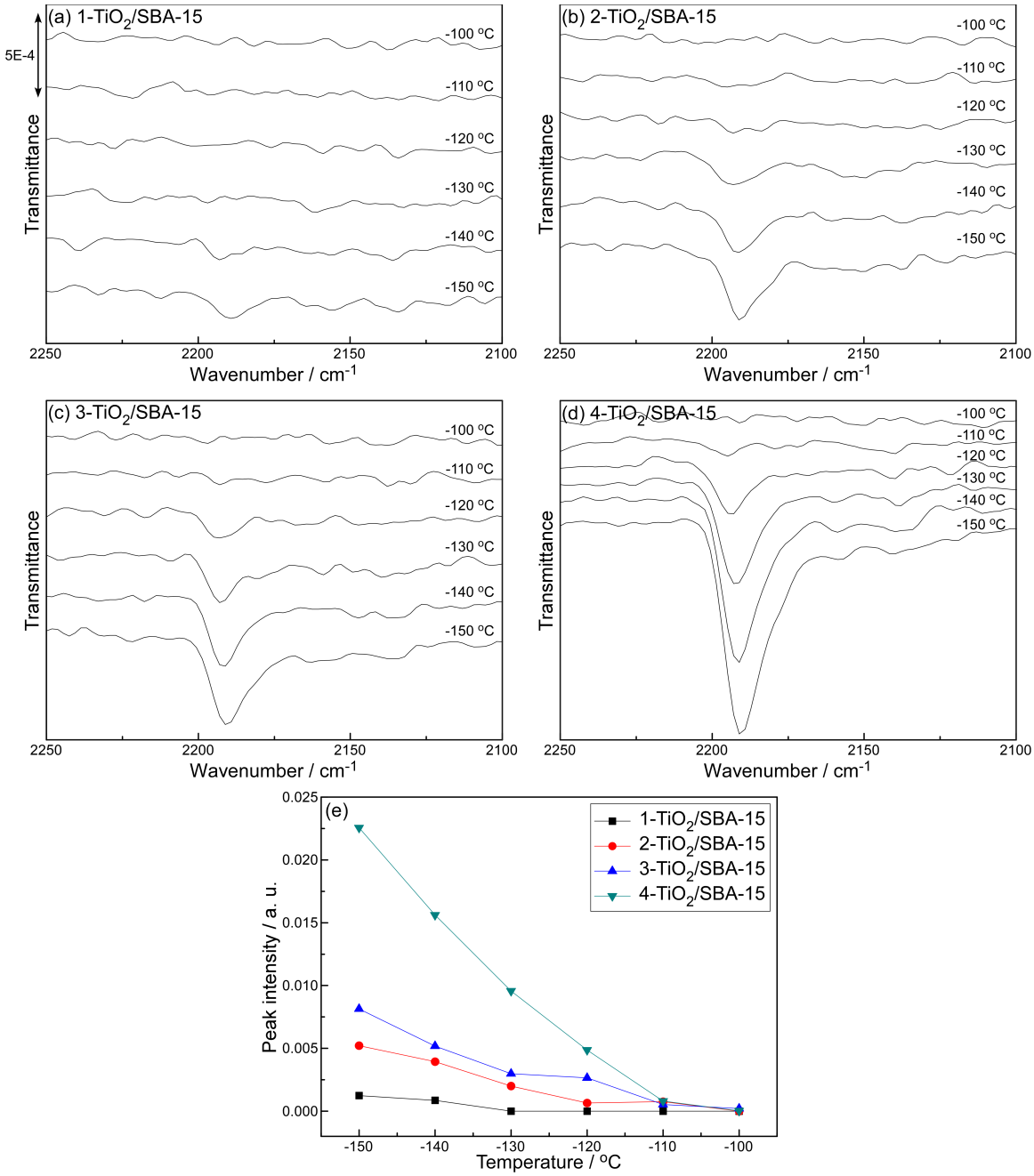

Figure 3.2 CO IR absorption spectra of (a) 1-TiO_2/SBA-15, (b) 2-TiO_2/SBA-15, (c) 3-TiO_2/SBA-15, (d) 4-TiO_2/SBA-15. (e) Peak intensities versus temperature.

IR absorption spectroscopy using CO as a probe molecule has proven versatile and sensitive to characterize nanostructured catalysts. The peak positions of the C-O stretching mode in IR spectra can differentiate between adsorption on metals and oxide supports, provide information on the oxidation state of the metal, and distinguish the surface planes available for adsorption[55]. Figure 3.2 displays typical sequences of IR spectra obtained after CO adsorption as a function of temperatures. Only one peak at approximately 2190 cm^{-1} is observed, corresponding to CO adsorption on Ti^{4+} (Ti^{4+}-CO carbonyls)[56,57]. The shift of the peak position as temperature increasing is probably due to the changes in CO surface coverage upon CO desorption. As temperature increasing, CO molecules desorbed quickly from the TiO_2 surface (below -100 ^oC), as they are weakly bonded to the active sites, compared to CO adsorption on metals. As the number of ALD cycles increasing, the peak intensities grow monotonically, because more TiO_2 was deposited (Figure 3.2e).

Pyridine is a powerful probe to identify the surface acidic sites on SiO_2 and TiO_2, since pyridine adsorbs more strongly on oxides than CO, and it is sensitive to Lewis acidic sites and Brønsted acidic sites[58]. As shown in Figure 3.3a, there are two main peaks at 1445 and 1595 cm^{-1}, especially for pure SBA-15, corresponding to the hydrogen-bonded pyridine, indicating the existence of OH groups on the surface. The peak at 1547 cm^{-1} is associated with pyridinum ions, and is indicative of adsorption on Brønsted acidic sites. It is worth focusing on the peaks at 1489, 1576, and 1608 cm^{-1}, which are assigned to coordinately bonded pyridine on Lewis acidic sites[32,59,60]. These three peaks reach a maximum in intensity after 4 ALD cycles (Figure 3.3b), suggesting that more Lewis acidic sites were created after the deposition of TiO_2 on SBA-15.

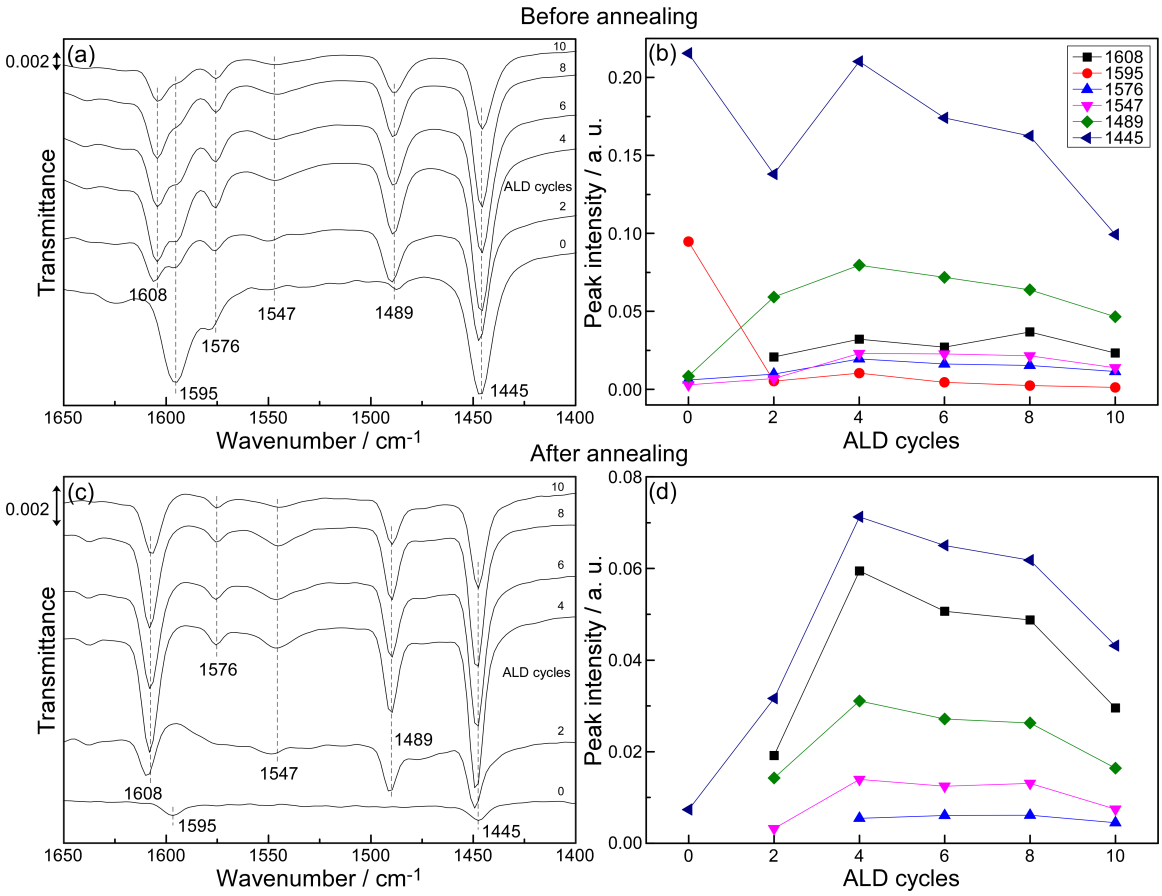

Figure 3.3 (a, c) Pyridine IR absorption spectra of (0-10)-TiO_2/SBA-15. (b, d) Peak intensities versus temperature before and after annealing at 150 ºC.

The weakly adsorbed species desorbed after annealing at 150 ºC. Figure 3.3c shows that the Lewis acidic sites-bonded pyridine is more stable than the hydrogen-bonded pyridine to outgassing. It is more obvious to see that 4-TiO_2/SBA-15 shows the largest number of Lewis acidic sites. Therefore, the ALD-TiO_2 films significantly change the surface of SBA-15, and create new acidic sites.

Figure 3.4a shows the Ti 2p XPS spectra of (2-10)-TiO_2/SBA-15. The Ti $2p_{1/2}$ and Ti $2p_{3/2}$ spin-orbital splitting photoelectrons for all the samples are located at 464.7 and 458.9 eV, respectively. The Ti signal intensities increase monotonically as the thickness of TiO_2 films growing. Only fully oxidized Ti^{4+} peaks are seen in all cases. The O 1s spectra (Figure 3.4b) exhibit two peaks at 530.4 and 532.7 eV, indicating the presence of two different environments of oxygen atoms[61,62]. The former one is associated with O bonded to Ti atoms. The latter one is attributed to O bonded to Si atoms.

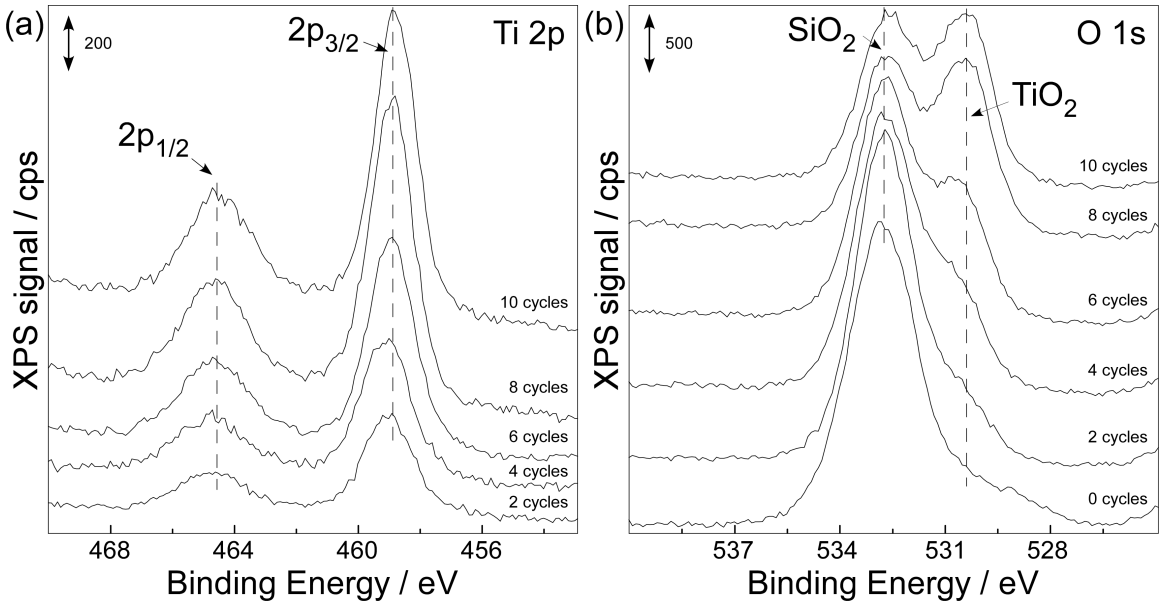

Figure 3.4 XPS spectra of (a) Ti 2p and (b) O 1s of (0-10)-TiO_2/SBA-15.

^{29}Si solid state NMR spectroscopy is a powerful tool to characterize and quantify the silanol groups of silica. As seen in Figure 3.5, an intense peak at -101.3 ppm, corresponding to Q_3, and two shoulder peaks at -92.0 and -110.6 ppm, associated with Q_2 and Q_4 structural units, are observed. Q_n terms refer to $[Si(OSi)_n(OH)_{4-n}]$ with n = 0, 1, 2, 3, 4[63]. The three chemical shifts at -92.0, -101.3 and -110.6 ppm can be assigned to geminal silanol groups $[(SiO)_2Si-(OH)_2]$, isolated silanol groups $[(SiO)_3Si-OH]$, and siloxane groups $[(SiO)_4Si]$, respectively[64,65]. An increase of peak intensity of Q_4, along with a significant decrease of peak intensity of Q_3 after 10 ALD cycles (Figure 3.5e), indicates the silanol groups on SBA-15 have been covered by TiO_2 films. After the TiO_2 deposition, Q_2 and Q_3 species were reduced, while more Q_4 species formed. Additionally, the NMR results suggest that the ALD process occurs preferentially at isolated silanol groups, the predominant type of Si-OH groups present on the surface.

The Q_4 species represent the interlinked SiO_4 tetrahedrons, which are located inside the SBA-15 walls, while Q_2 and Q_3 species related to OH groups are mainly located on the surface of SBA-15. It is worth noting that the peak intensity of Q_4 does not change greatly, but the peak intensity of Q_3 decreases remarkably, because the deposition of TiO_2 films just modifies the surface of SBA-15 without greatly affecting the structure inside SBA-15.

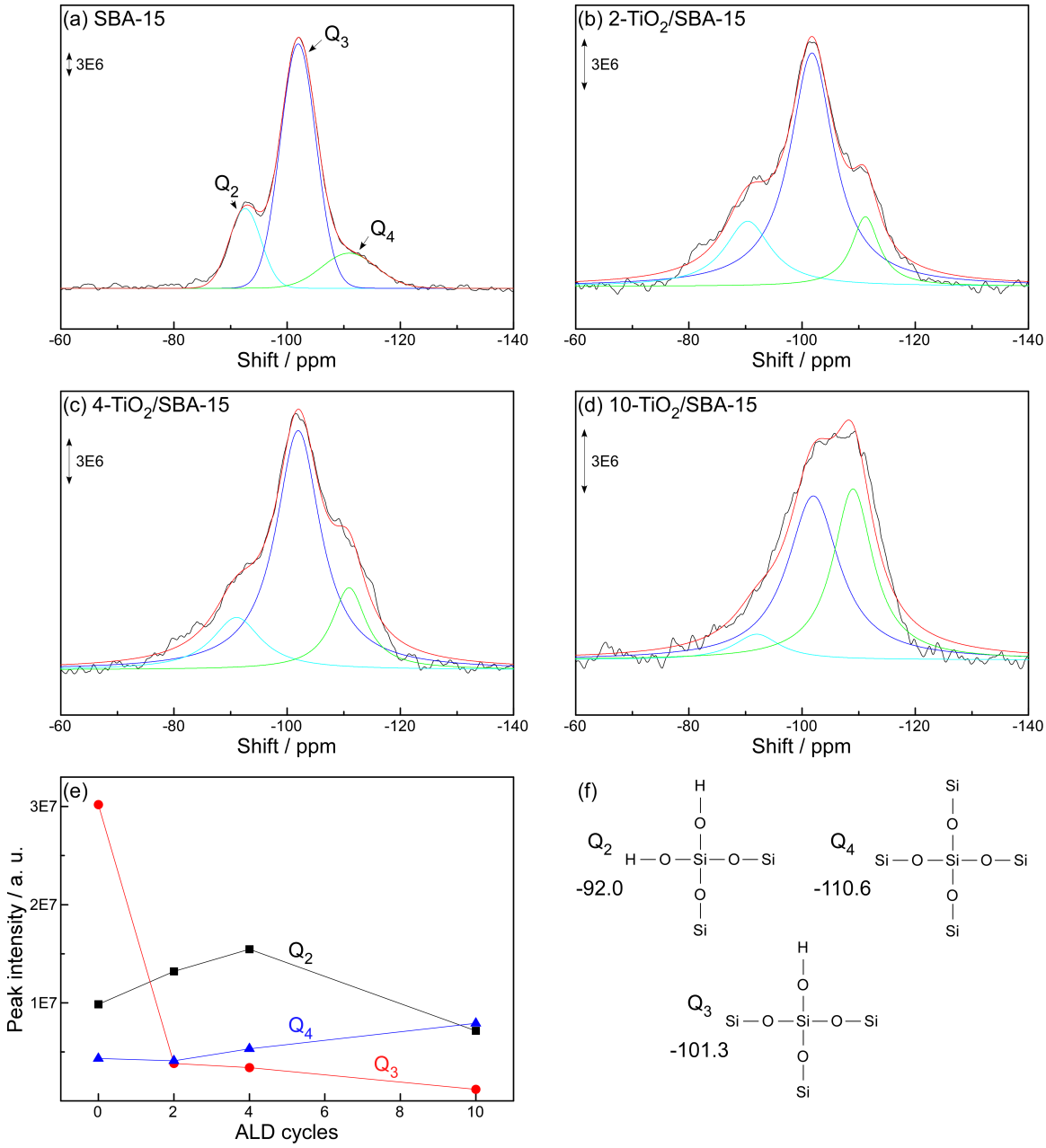

Figure 3.5 ^{29}Si NMR spectra of (a) SBA-15, (b) 2-TiO_2/SBA-15, (c) 4-TiO_2/SBA-15 and (d) 10-TiO_2/SBA1-5. (e) Peak intensities versus ALD cycles. (f) Peak assignments and structures of various silica species.

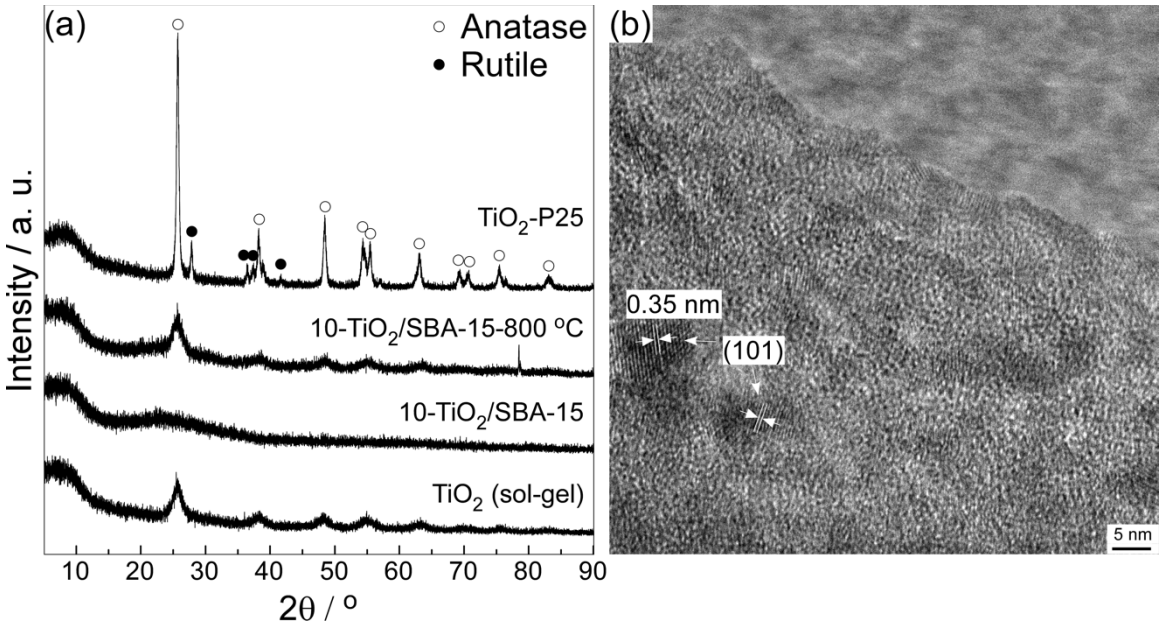

Figure 3.6 (a) XRD patterns of TiO_2-P25, 10-TiO_2/SBA-15 calcined at 800 ºC, 10-TiO_2/SBA-15 and TiO_2 (sol-gel). (b) TEM image of 10-TiO_2/SBA-15 calcined at 800 ºC.

Commercial TiO_2-P25, containing 80 wt% of anatase and 20 wt% of rutile, and TiO_2 (sol-gel) were used as reference samples. The fresh and calcined 10-TiO_2/SBA-15, as well as TiO_2-P25 and TiO_2 (sol-gel), were investigated by XRD and TEM to study their crystallinity. As shown in the XRD patterns, the TiO_2-P25 is well-crystallized, whereas the fresh 10-TiO_2/SBA-15 is amorphous. The TiO_2 (sol-gel) is poorly crystallized (almost amorphous), though we intended to synthesize completely amorphous TiO_2. Anyway, this TiO_2 prepared by sol-gel method is close to our amorphous TiO_2/SBA-15 samples. After calcination at 800 ºC, the amorphous TiO_2 films crystallized (Figure 3.6a). This can be confirmed by the TEM image (Figure 3.6b), where crystallites and anatase (101) planes can be detected.

EPR measurements were utilized to identify Ti^{3+} species and the reducibility of various TiO_2 materials. The signal at 3330 G is attributed to Ti^{3+} species[66,67] (Figure 3.7). All the

fresh samples do not show this signal. However, 4-TiO_2/SBA-15 and TiO_2 (sol-gel) display remarkable enhancement of this signal after H_2 reduction at 350 ^oC, indicating that only amorphous or poorly crystallized TiO_2 were reduced. Crystallized TiO_2-P25 is much less reducible than amorphous TiO_2. Furthermore, subsequent oxidation significantly decreases the signal intensity, suggesting that Ti^{3+} was reoxidized to Ti^{4+}. Therefore, the EPR spectra verify that the ALD-TiO_2/SBA-15 samples exhibit excellent reducibility.

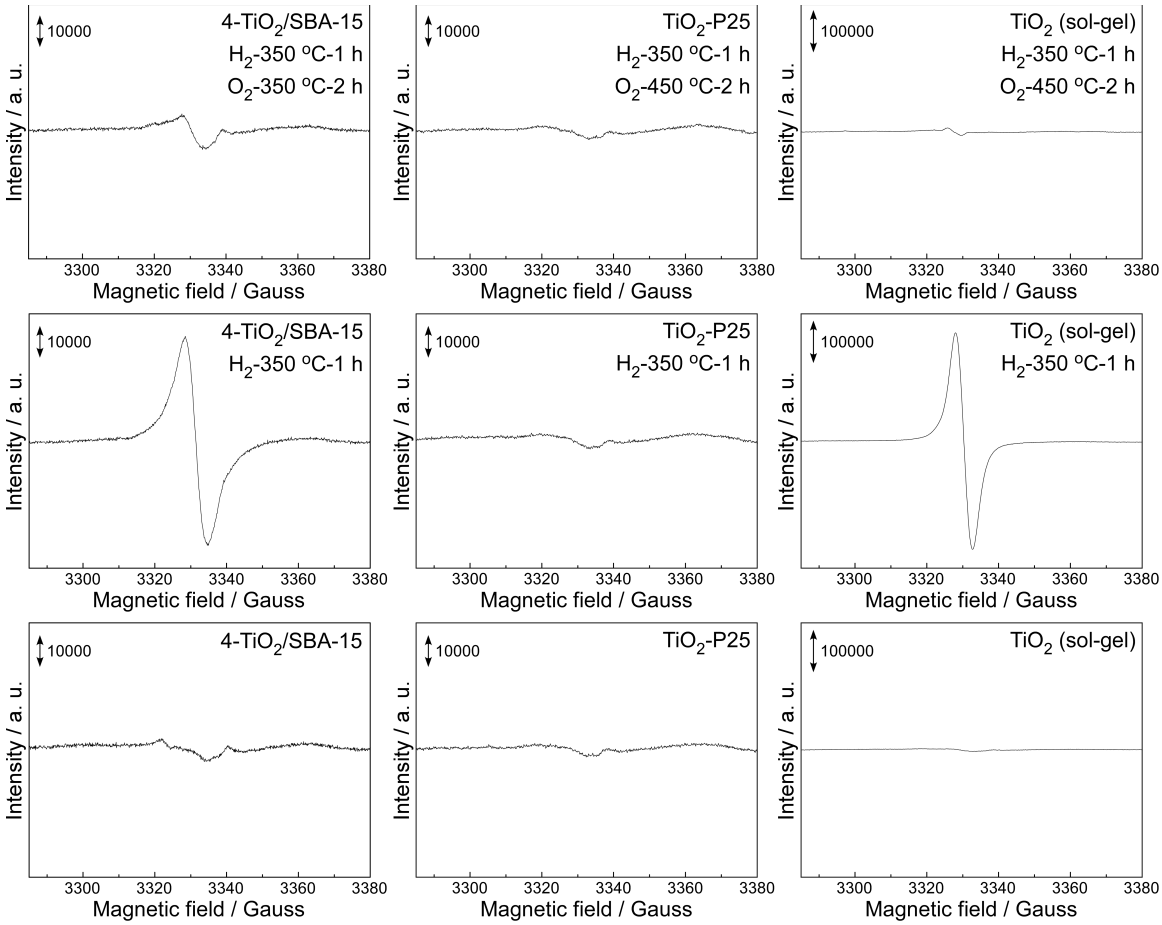

Figure 3.7 EPR spectra of 4-TiO_2/SBA-15 (left), TiO_2-P25 (center), and TiO_2 (sol-gel) (right). From bottom to top are fresh, calcined under H_2, and calcined under H_2 followed by O_2 samples, respectively.

The weight percent of TiO_2 was estimated by ICP measurements, as listed in Table 3.1. The TiO_2 loadings increase linearly as a function of the number of ALD cycles used. Approximate 6 wt% of TiO_2 was deposited per ALD cycle.

Table 3.1 TiO_2 loadings of (1-4)-TiO_2/SBA-15

Sample	Average TiO_2 load (%)	Standard deviation
1-TiO_2/SBA-15	8.10	0.00
2-TiO_2/SBA-15	13.98	0.02
3-TiO_2/SBA-15	18.79	0.02
4-TiO_2/SBA-15	25.74	0.00

3.4 Conclusions

The TiO_2 films were successfully deposited on mesoporous silica-SBA-15 via ALD. The growth rate is approximately 1 Å per cycle. The mesoporous structure of SBA-15 was retained even after 10 ALD cycles. New surface sites were created after the TiO_2 deposition, and only fully oxidized Ti^{4+} were detected. The ALD process mainly occurs on isolated silanol groups on the SBA-15 surface. The as-prepared TiO_2 films are amorphous and reducible, differing from the crystallized TiO_2, such as anatase and rutile. The uniform growth of TiO_2 in a controlled fashion and the redox properties of TiO_2 are fundamental for the further study of supported Pt or Au nanocatalysts.

Chapter 4 Synthesis, characterization and catalytic performance studies of supported Pt nanocatalysts

4.1 Introduction

In this chapter, TiO_2 films and Pt nanoparticles were deposited in two possible sequences, as shown in Figure 4.1.The Pt nanoparticles were dispersed on top of TiO_2 films or the TiO_2 films were deposited after Pt. The microstructure was investigated by TEM and EDS, and Pt nanoparticle size distributions were estimated from the TEM images with 100 particles. The Pt and TiO_2 loadings were estimated by ICP-OES. The mesoporous structures were characterized by N_2 adsorption-desorption isotherms. The two types of catalysts, as well as the Pt/SBA-15, Pt/TiO_2-P25 and Pt/TiO_2 (sol-gel) as reference catalysts, were tested for hydrogenation of cinnamaldehyde (CAL) and CO oxidation reactions.

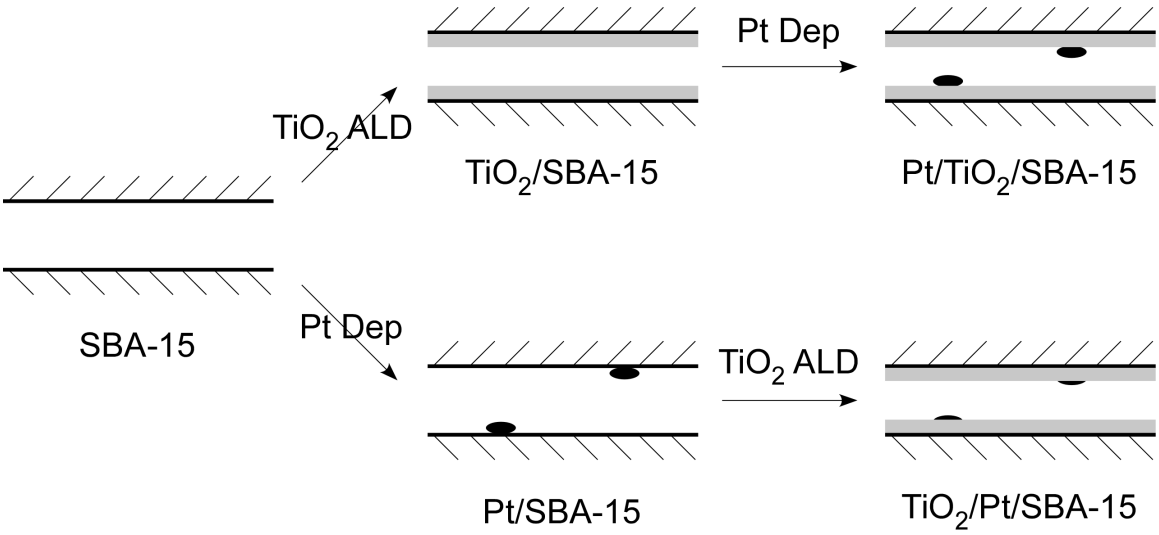

Figure 4.1 Synthetic approaches.

4.2 Experimental

4.2.1 Synthesis of Pt/SBA-15

Pt/SBA-15 catalysts were prepared by colloidal method. 2.59 mL of 0.006 mol/L $H_2PtCl_6 \cdot 6H_2O$ aqueous solution, 2.4 mL of DI water, 45 mL of ethanol, 0.060 g of PVP and 0.3 g of SBA-15 were mixed together, followed by sonication for 30 min and magnetic stir for 1 h. The suspension was transferred to a 2-neck flask equipped with a thermocouple and condenser, and refluxed at 79 ^oC for 3 h with magnetic stirring. After centrifugation and completely dry, the powder was calcined under O_2 at 500 ^oC for 24 h, and then reduced under H_2 at 200 ^oC for 2 h to remove PVP.

4.2.2 Synthesis of TiO_2/Pt/SBA-15

The as-prepared Pt/SBA-15 was used as support. The deposition of TiO_2 followed the same procedure in Chapter 3.

4.2.3 Synthesis of Pt/TiO_2/SBA-15

The Pt/(1-4)-TiO_2/SBA-15 were prepared by deposition precipitation (DP) method, using the as-prepared (1-4)-TiO_2/SBA-15 as supports. 0.86 mL of 0.006 mol/L $H_2PtCl_6 \cdot 6H_2O$ aqueous solution, 20 mL of DI water, 100 mg TiO_2/SBA-15 were mixed together and sonicated for 30 min. The solvent was removed via rotary evaporation at around 58 ^oC for 3 h. After completely dry, the powder was reduced at 350 ^oC under H_2 for 3 h.

4.2.4 Synthesis of Pt/TiO_2-P25 and Pt/TiO_2 (sol-gel)

The synthesis of Pt/TiO_2-P25 and Pt/TiO_2 (sol-gel) employed the same DP method, but using 8.63 mL of $H_2PtCl_6 \cdot 6H_2O$ solution, 30 mL of DI water and 1 g of TiO_2-P25 or TiO_2 (sol-gel).

The Pt loading of all the catalysts was approximately 1 wt.%.

4.2.5 Hydrogenation of cinnamaldehyde

20 mg of catalysts without any pretreatment were mixed with approximately 0.8 g of cinnamaldehyde, 2 mL of benzyl alcohol (internal standard) and 75 mL of 2-propanol (solvent) in the reactor vessel. The vessel was purged for 5 times and then pressurized to H_2 pressure of 30 bar. The reaction was running at 100 ^oC with stirring (1000 rpm). Aliquots were taken at preset times and analyzed by GC.

4.2.6 CO oxidation

The CO oxidation experiment was carried out in the same FTIR in transmission mode. The same procedure for preparing the catalyst disks and scanning parameters were employed. The disk was pre-treated at 350 ^oC under 200 Torr of H_2 for 2 h in situ in the IR cell under vacuum. Then the cell was evacuated and refilled with 200 Torr of CO and O_2 mixture (ratio of CO and O_2 is 1:1). The reaction was running at 150 ^oC and IR spectra were taken at preset times, and referenced to background traces recorded before CO was introduced into the cell.

The CO_2 pressures versus signal intensities were calibrated by introducing different amounts of CO_2 gas into the cell. As seen in Figure 4.2, a nice linear trend can be obtained from 0 to 15 Torr, and the CO_2 pressures can be calculated using the equation: y = 18.37996x+0.92548. Then the moles of CO_2 was calculated by the ideal gas law:

$$n = \frac{PV}{RT} \tag{4.1}$$

where P, T and R are the CO_2 pressure, reaction temperature and ideal gas law constant; V is the volume of the cell, which was estimated to be 0.00014 m^3; n is the moles of CO_2.

The turnover numbers (TONs) and turnover frequencies (TOFs) for all the catalytic reactions were calculated by the equations below:

$$n_{surface} = \frac{m \times L}{M_{Pt}} \times dispersion \tag{4.2}$$

$$Dispersion = \sqrt[1.23]{\frac{3.32}{\frac{d_{Pt\ nanoparticle}}{d_{Pt\ atom}}}} \tag{4.3}$$

$$TONs = \frac{n_{product}}{n_{surface}} \tag{4.4}$$

$$TOFs = \frac{TON}{\Delta t} \tag{4.5}$$

Where $n_{surface}$ is the number of surface atoms on Pt nanoparticle; m is the mass of catalyst used; L is the Pt loading; $d_{Pt\ nanoparticle}$ and $d_{Pt\ atom}$ are the diameters of Pt nanoparticle and single Pt atom; M_{Pt} is the molar mass of Pt; dispersion is the fraction of atoms of a material exposed to the surface[68]; $n_{product}$ is the moles of product (or reactant).

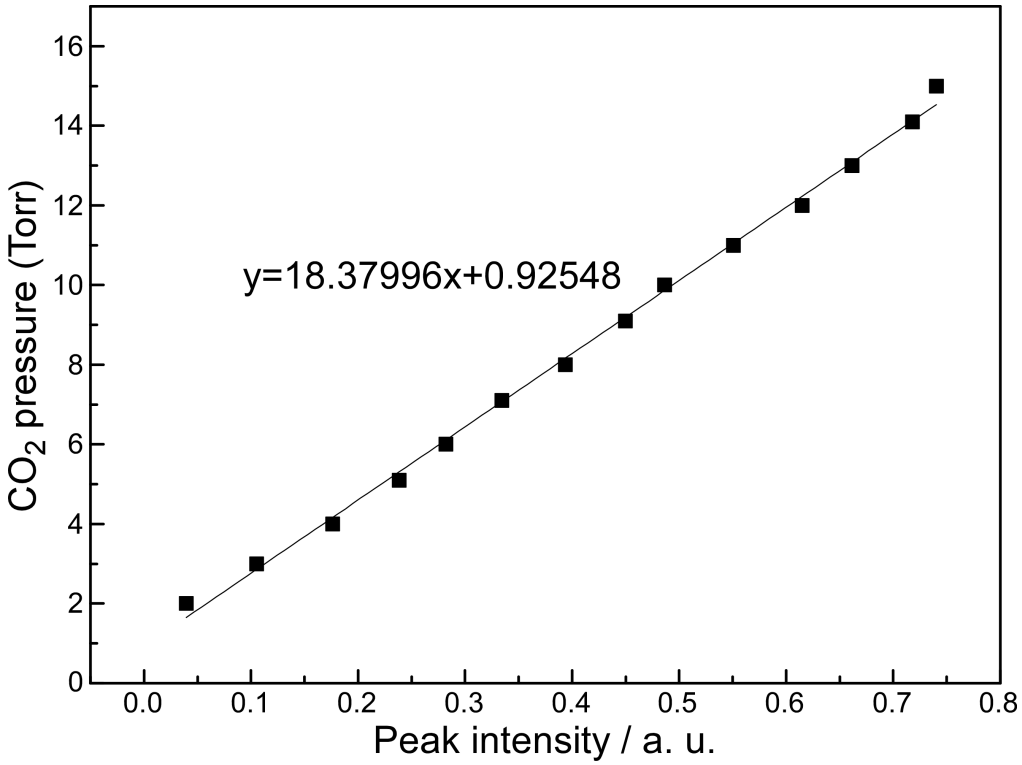

Figure 4.2 CO_2 calibration curve.

4.3 Results and discussion

4.3.1 Characterization of Pt/SBA-15 and removal of PVP

One of the most challenging tasks of this work is the incorporation of metal nanoparticles into the pores of SBA-15. PVP, as a capping agent, was employed in the synthetic process to stabilize and control the growth of nanoparticles, and prevent nanoparticles aggregation. The Pt nanoparticles were protected and encapsulated by the capping agent, so the Pt nanoparticles were finely dispersed in the mesoporous structure of SBA-15. However, the capping ligand is detrimental for catalytic performance, because the active sites are covered by the polymer. Therefore, the removal of PVP is critical as well.

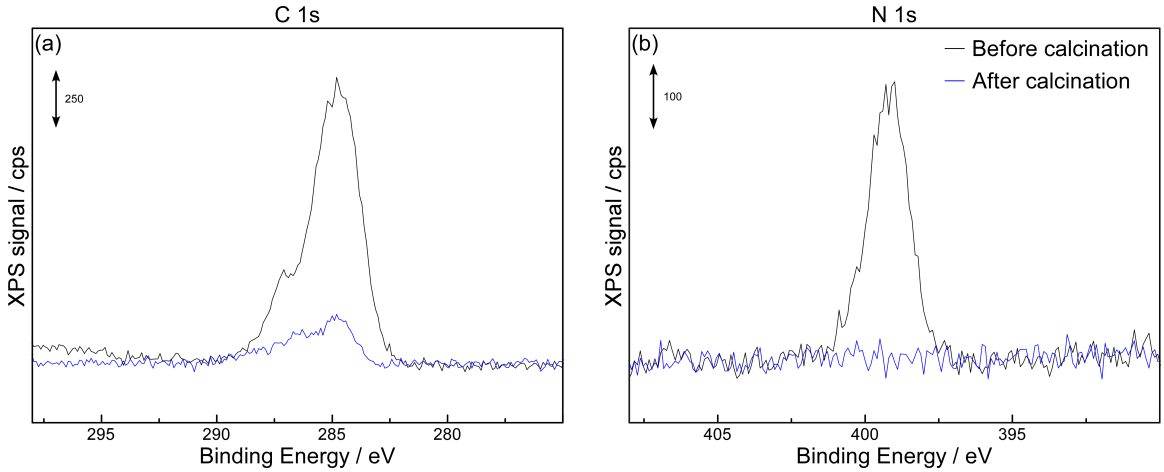

Figure 4.3 (a) C 1s and (b) N 1s XPS spectra of Pt/SBA-15 after calcination.

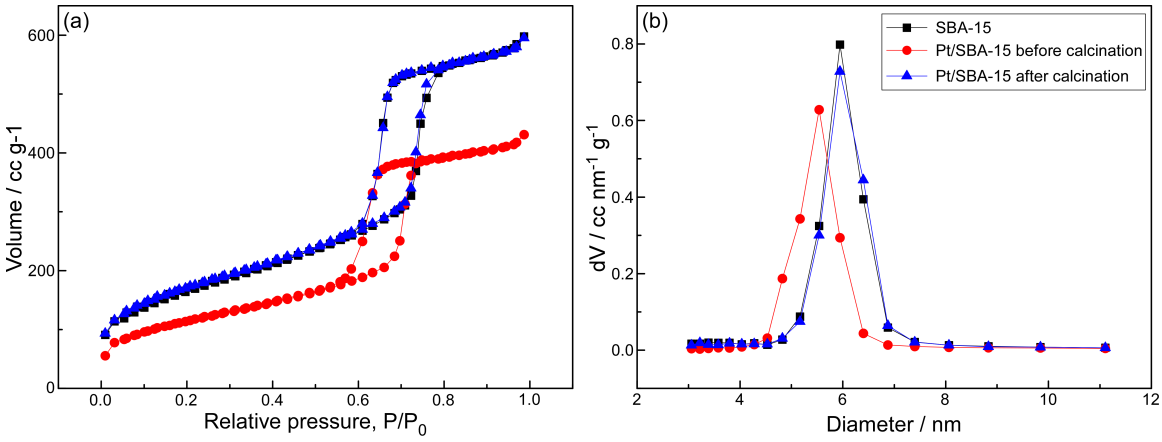

Figure 4.4 (a) N_2 adsorption-desorption isotherms. (b) Pore size distributions from desorption branch of SBA-15 and Pt/SBA-15 before and after calcination.

Table 4.1 Summary of surface areas, pore volumes and pore diameters of SBA-15, Pt/SBA-15 before and after calcination

Sample	Surface area (m^2/g)	Adsorption		Desorption	
		Pore volume (cc/g)	Pore diameter (nm)	Pore volume (cc/g)	Pore diameter (nm)
SBA-15	621.988	0.833	7.911	0.892	5.938
Pt/SBA-15 before calcination	419.469	0.668	5.527	0.619	7.015
Pt/SBA-15 after calcination	629.049	0.826	7.907	0.886	5.939

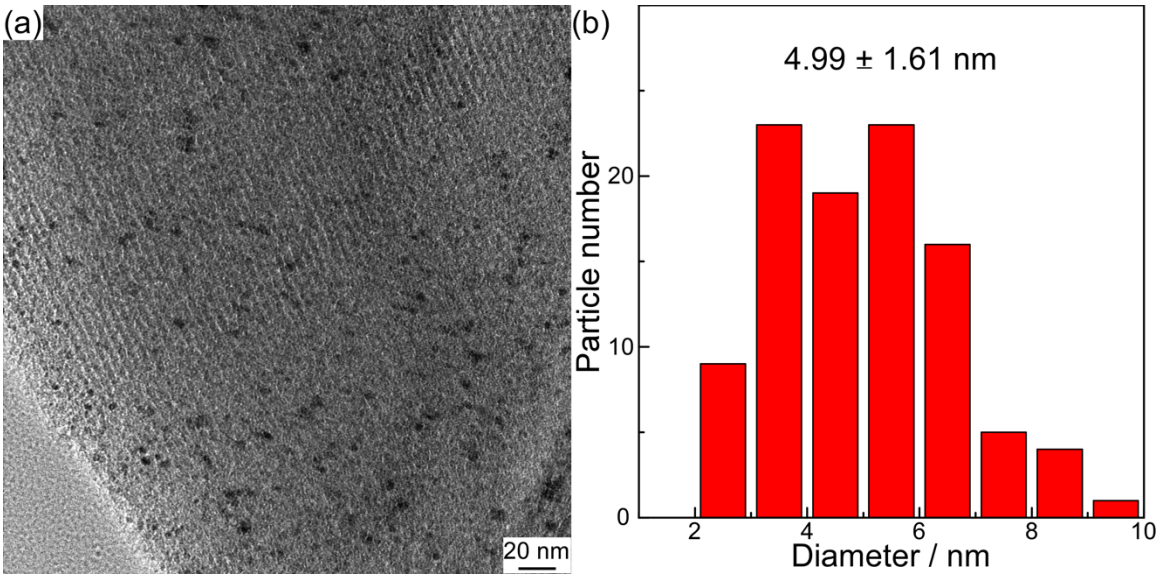

Figure 4.5 (a) TEM image. (b) Pt nanoparticle size distributions of Pt/SBA-15 after calcination.

Since PVP is not thermally stable, Pt/SBA-15 was treated under O_2 and H_2 at high temperature to decompose PVP. As PVP [$(C_6H_9NO)_n$] contains C and N elements, the removal of PVP can be verified by XPS. Although the XPS signals come from the surface of sample, we think the calcination of Pt/SBA-15 in the furnace is uniform. As shown in Figure 4.3, the N 1s signal disappeared, and C 1s signal intensity decreased significantly after calcination, indicating the PVP has been removed after treatment. The weak C 1s peak is attributed to the carbon contamination from atmosphere.

The surface area, pore volume and pore diameter changes before and after calcination compared with pure SBA-15 (Figure 4.4 and Table 4.1) exhibit that PVP occupied certain porous structures of SBA-15. Nevertheless, PVP was eliminated after calcination, since all the geometrical parameters increased back to almost the same values as pure SBA-15.

The N_2 adsorption-desorption isotherms (Figure 4.4a) suggest that the mesoporous structure of SBA-15 did not collapse, which can also be proven by the TEM image (Figure

4.5a). As seen in Figure 4.5, the Pt nanoparticles were well-dispersed in the pores of SBA-15, and the diameter of the nanoparticles is approximately 4.99 nm. Therefore, the Pt nanoparticles were uniformly deposited into the pores of SBA-15, and the PVP was removed without destroying SBA-15 structure.

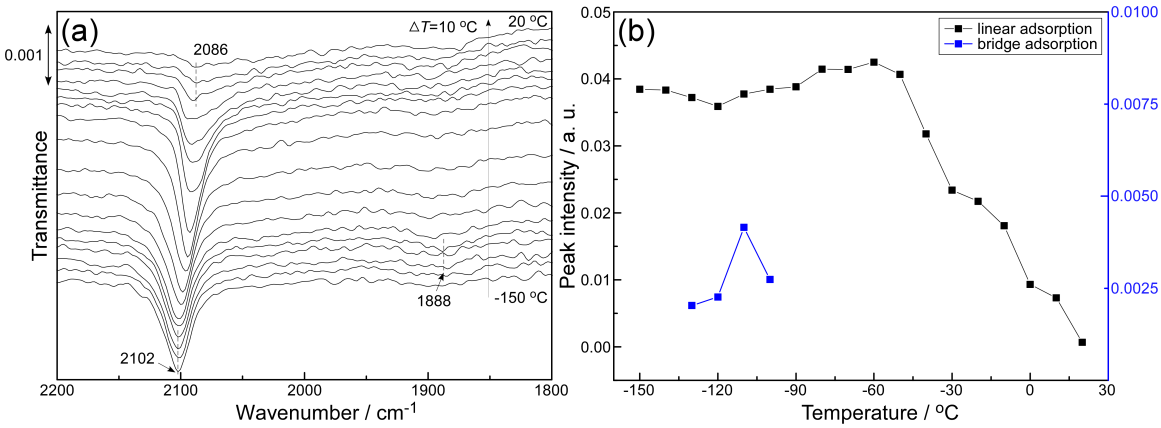

Figure 4.6 (a) CO IR absorption spectra of Pt/SBA-15, and (b) peak intensities versus temperature after calcination.

Figure 4.6 displays a typical sequence of IR spectra obtained after CO adsorption on Pt/SBA-15 and evolution of peak intensities extracted from the spectra as a function of temperature. Two features located at 1888 cm^{-1}, which is associated with CO adsorption bridged on two Pt atoms, and 2086-2102 cm^{-1}, corresponding to CO linearly adsorbed on Pt atop sites of lower Miller index terraces, can be identified[69–71]. The intensity of the bridging band is very weak, because CO molecules preferentially adsorb on atop Pt sites. This peak becomes the most prominent at -110 °C, though it is hard to be observed. The feature at 2086-2102 cm^{-1} is of the most interest, since it probes the accessibility of the Pt surface to the reactants. The CO molecules desorbed from the Pt atop sites gradually as the catalyst was warmed up, and the desorption rate reaches a maximum at -40 °C. The redshift

of this peak is due to the decrease of CO surface coverage upon desorption. Overall, the Pt surface is clean and accessible to CO molecules after the PVP is removed.

4.3.2 Characterization of (1-4)-TiO_2/Pt/SBA-15 and Pt/(1-4)-TiO_2/SBA-15

The mesoporous structure and geometrical parameters of the support were investigated by N_2 adsorption-desorption isotherms as reported in Figure 4.7. The mesoporous structure of all the catalysts was retained after Pt and TiO_2 deposition, indicating that neither the deposition of Pt nor TiO_2 destroyed the ordered structure of SBA-15. The pore diameter decreased linearly, while the pore volume and surface area decreased monotonically as a function of the number of ALD cycles, which is consistent with the TiO_2/SBA-15 samples. Nevertheless, since at least two batches of TiO_2/SBA-15 samples are needed for the preparation of Pt/TiO_2/SBA-15, the pore size distributions of Pt/TiO_2/SBA-15 are broader than others (Figure 4.7d), and larger errors are observed in Figure 4.7f.

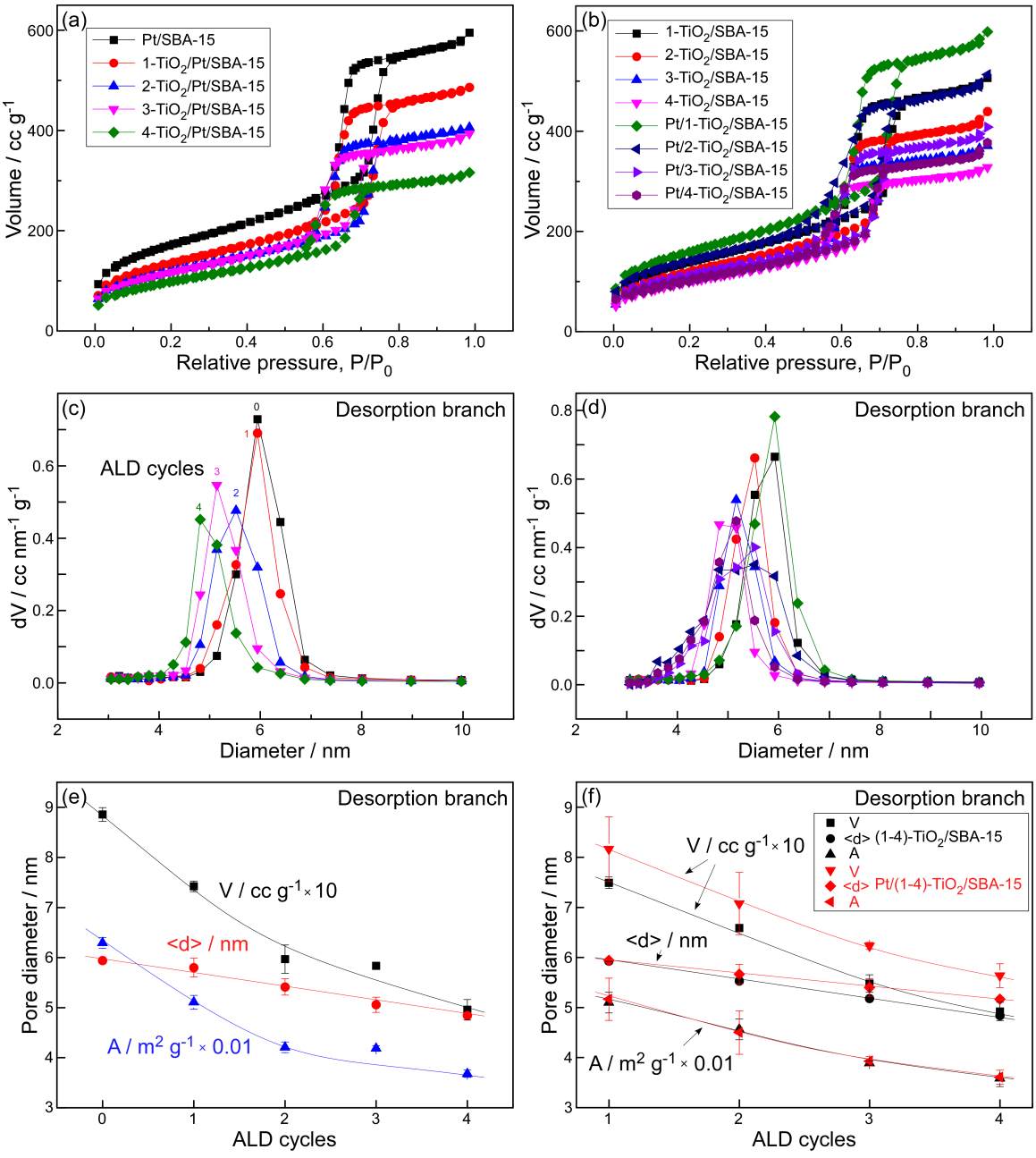

Figure 4.7 (a, b) N_2 adsorption-desorption isotherms. (c, d) Pore size distributions, (e, f) <d>, V, and A, estimated from desorption branch, of (1-4)-TiO_2/Pt/SBA-15 and Pt/(1-4)-TiO_2/SBA-15. Pt/SBA-15 and (1-4)-TiO_2/SBA-15 are used as reference samples. Data are reported as a function of the number of ALD cycles used.

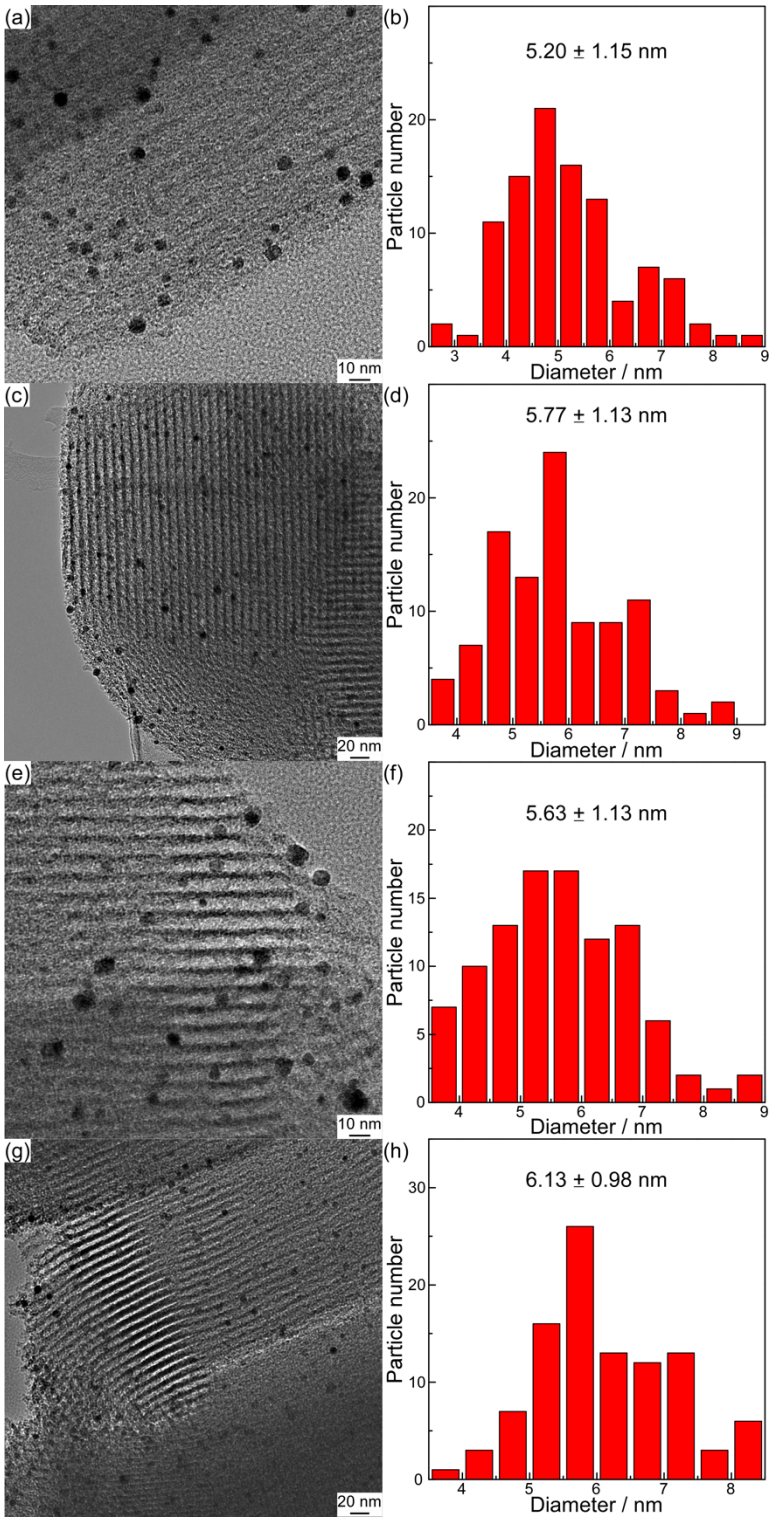

Figure 4.8 TEM images and Pt nanoparticle size distributions of (a, b) 1-TiO_2/Pt/SBA-15, (c, d) 2-TiO_2/Pt/SBA-15, (e, f) 3-TiO_2/Pt/SBA-15, and (g, h) 4-TiO_2/Pt/SBA-15.

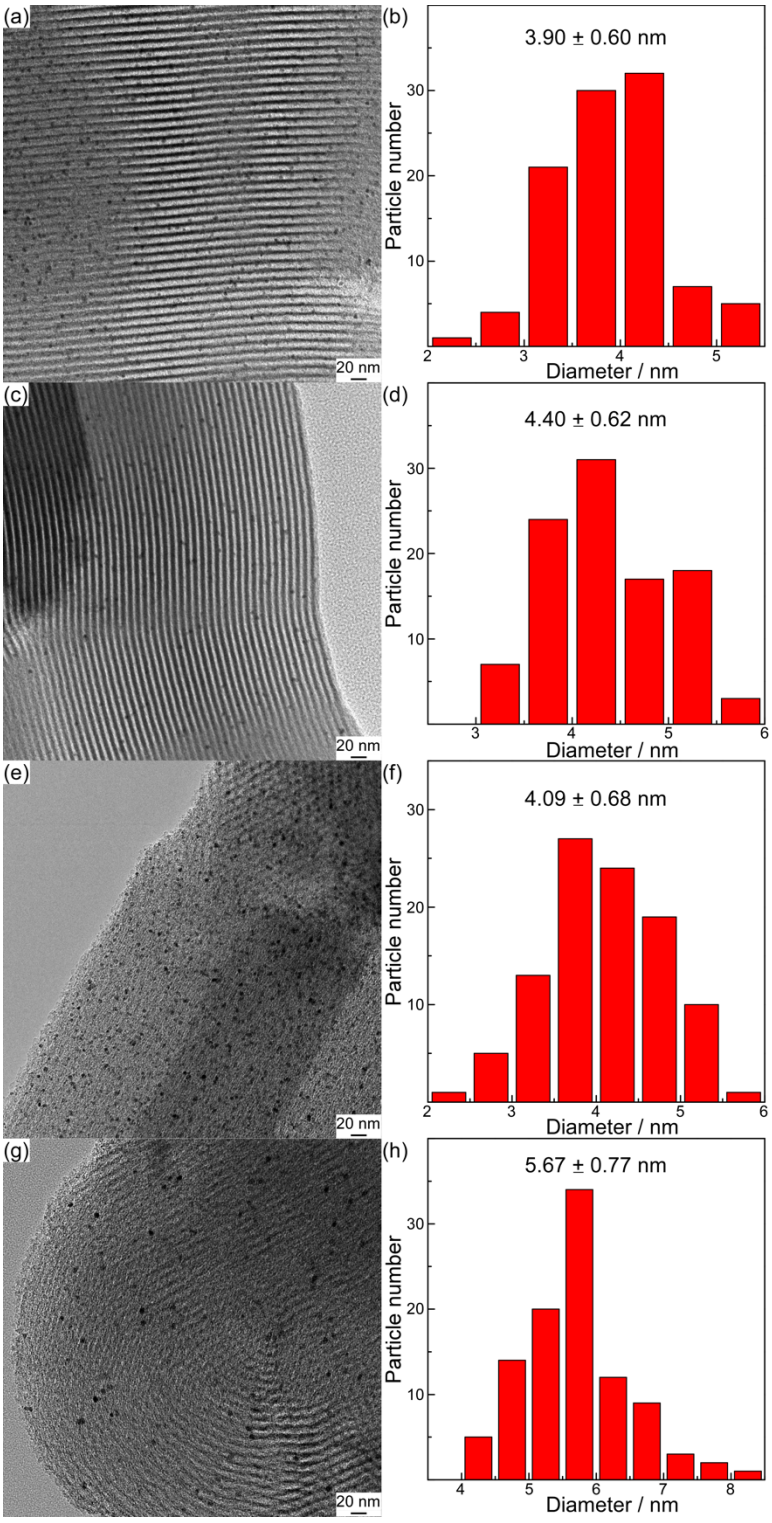

Figure 4.9 TEM images and Pt nanoparticle size distributions of (a, b) Pt/1-TiO_2/SBA-15, (c, d) Pt/2-TiO_2/SBA-15, (e, f) Pt/3-TiO_2/SBA-15, and (g, h) Pt/4-TiO_2/SBA-15.

The TEM images and Pt nanoparticle distributions of (1-4)-TiO_2/Pt/SBA-15 are reported in Figure 4.8. The average diameters of the Pt nanoparticles for (1-4)-TiO_2/Pt/SBA-15 are approximately 5.20, 5.77, 5.63, and 6.13 nm, respectively. The Pt nanoparticles are still homogeneously distributed in the channels of SBA-15 after TiO_2 deposition. Figure 4.9 shows the similar data of Pt/(1-4)-TiO_2/SBA-15. The average diameters of the Pt nanoparticles for Pt/(1-4)-TiO_2/SBA-15 are approximately 3.90, 4.40, 4.09, and 5.67 nm, respectively. The TEM images (Figure 4.9a, c, e and g) clearly show that the Pt nanoparticles were incorporated into the mesoporous structure, and well-dispersed in the pores of SBA-15. It appears that the Pt nanoparticles of all the samples are primarily located inside the pores, though the possibility of Pt nanoparticles located outside cannot be ruled out. The DP method for synthesizing Pt/(1-4)-TiO_2/SBA-15 works well, as the noble metal atoms can be immobilized on the TiO_2 modified SBA-15 support. This method is commonly used for the preparation of noble metal supported on TiO_2 catalysts. Finally, the TiO_2 films of all the samples are too thin to be clearly visible by TEM.

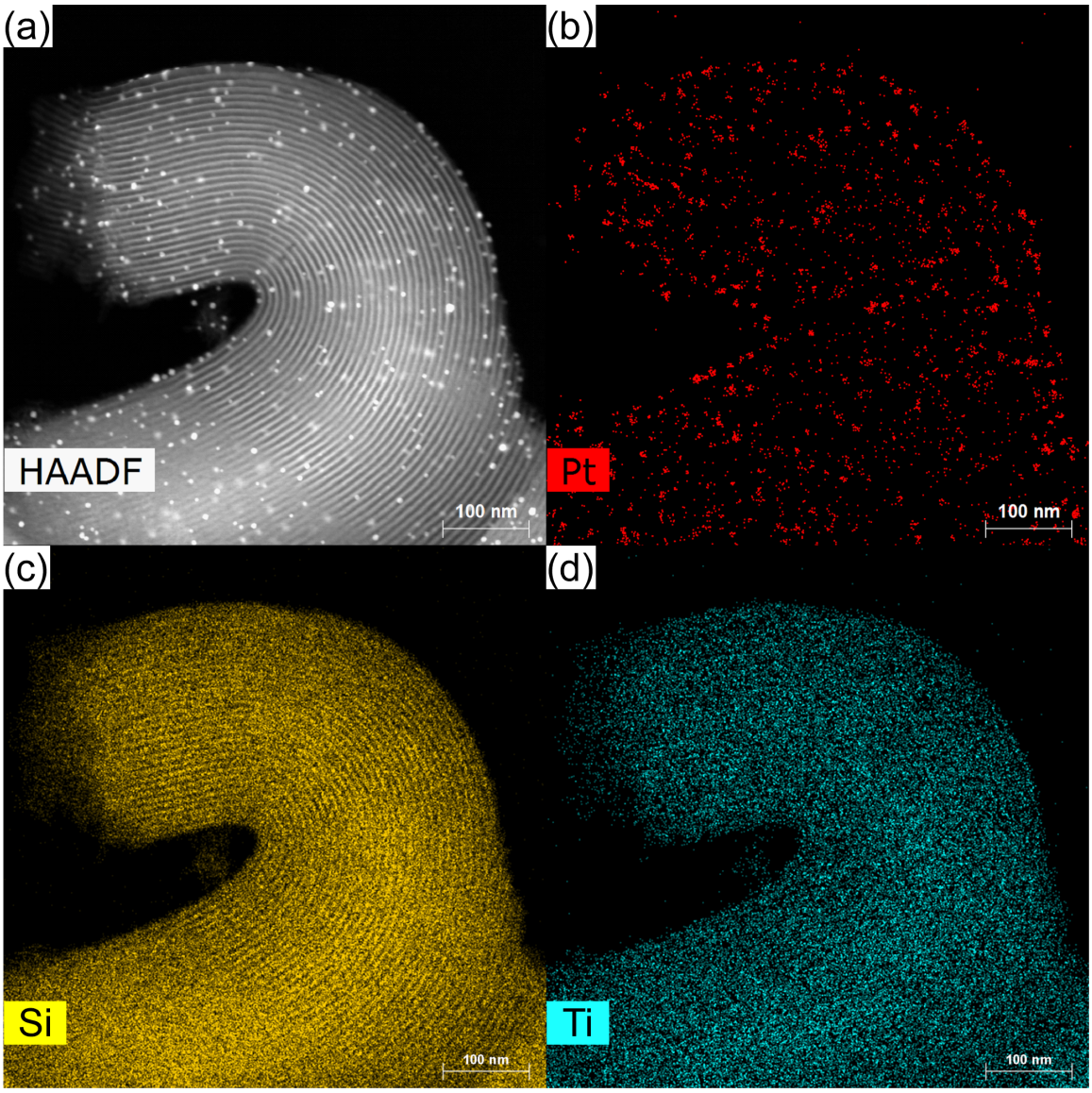

Figure 4.10 (a) HAADF image. EDS mapping images of Pt (b), Si (c) and Ti (d) of 1-TiO_2/Pt/SBA-15.

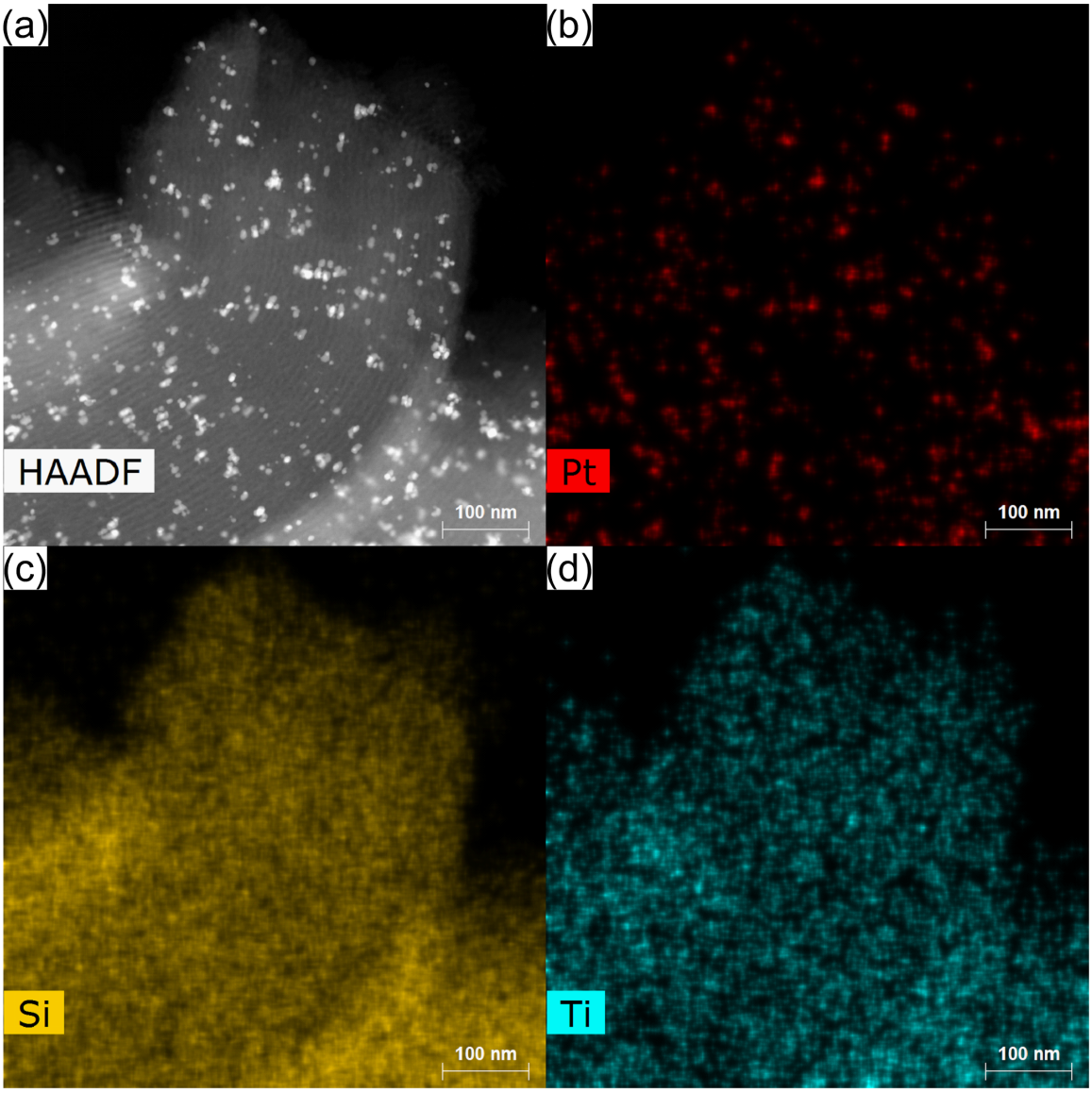

Figure 4.11 (a) HAADF image. EDS mapping images of Pt (b), Si (c) and Ti (d) of Pt/1-TiO_2/SBA-15.

1-TiO_2/Pt/SBA-15 and Pt/1-TiO_2/SBA-15 are selected for HAADF and EDS elemental analysis. The HAADF images (Figure 4.10a and 4.11a) demonstrated that the Pt nanoparticles are well-dispersed in the pores of SBA-15 and TiO_2/SBA-15. No serious nanoparticle aggregation can be seen. The EDS mapping images of Pt (Figure 4.10b and 4.11b) confirm that the Pt atoms are in nanoparticle forms. Figure 4.10d and 4.11d reveal that titanium was uniformly deposited on the entire SBA-15.

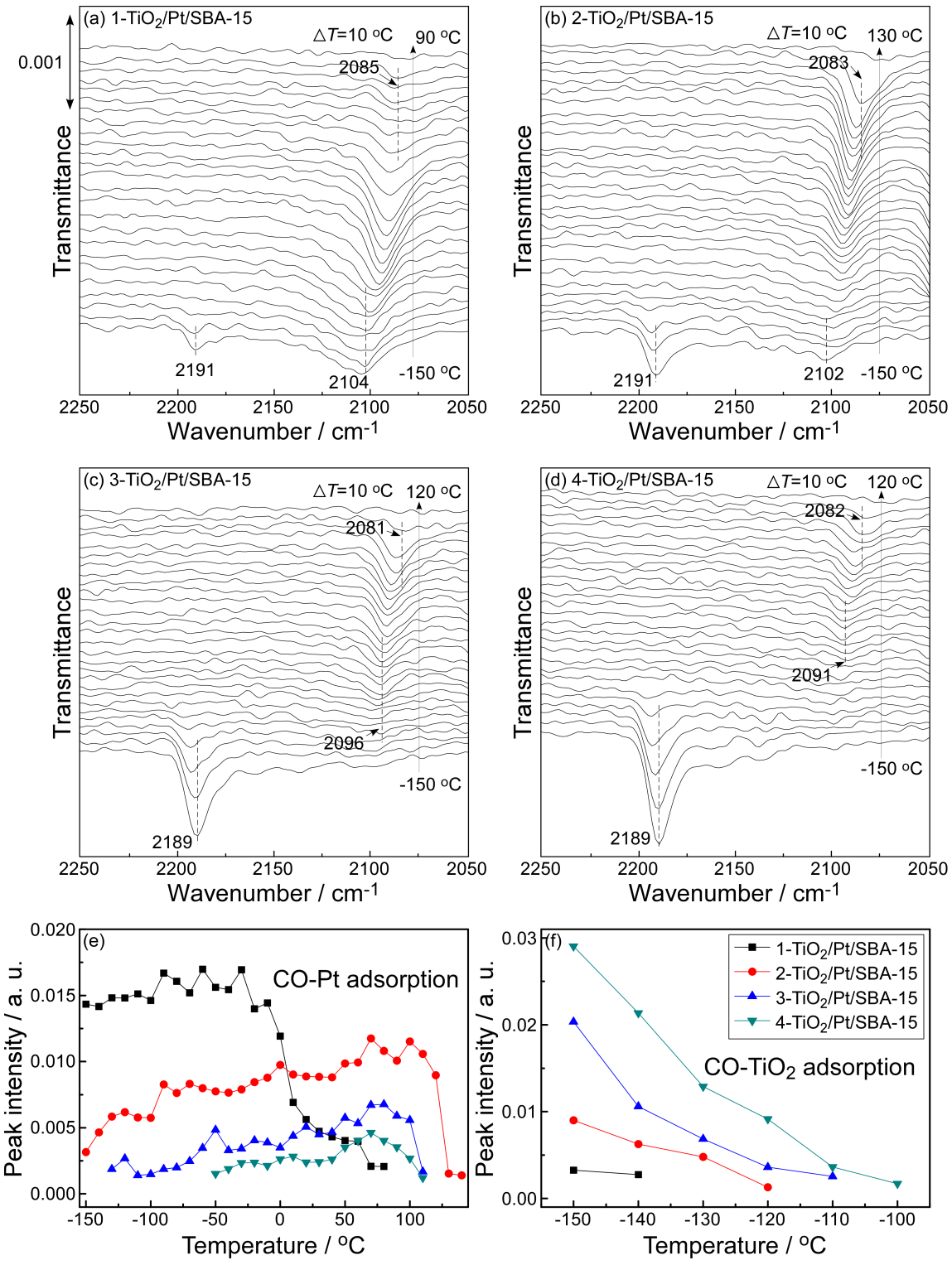

Figure 4.12 CO IR absorption spectra of (1-4)-TiO_2/Pt/SBA-15 (a to d). Peak intensities versus temperature (e, f).

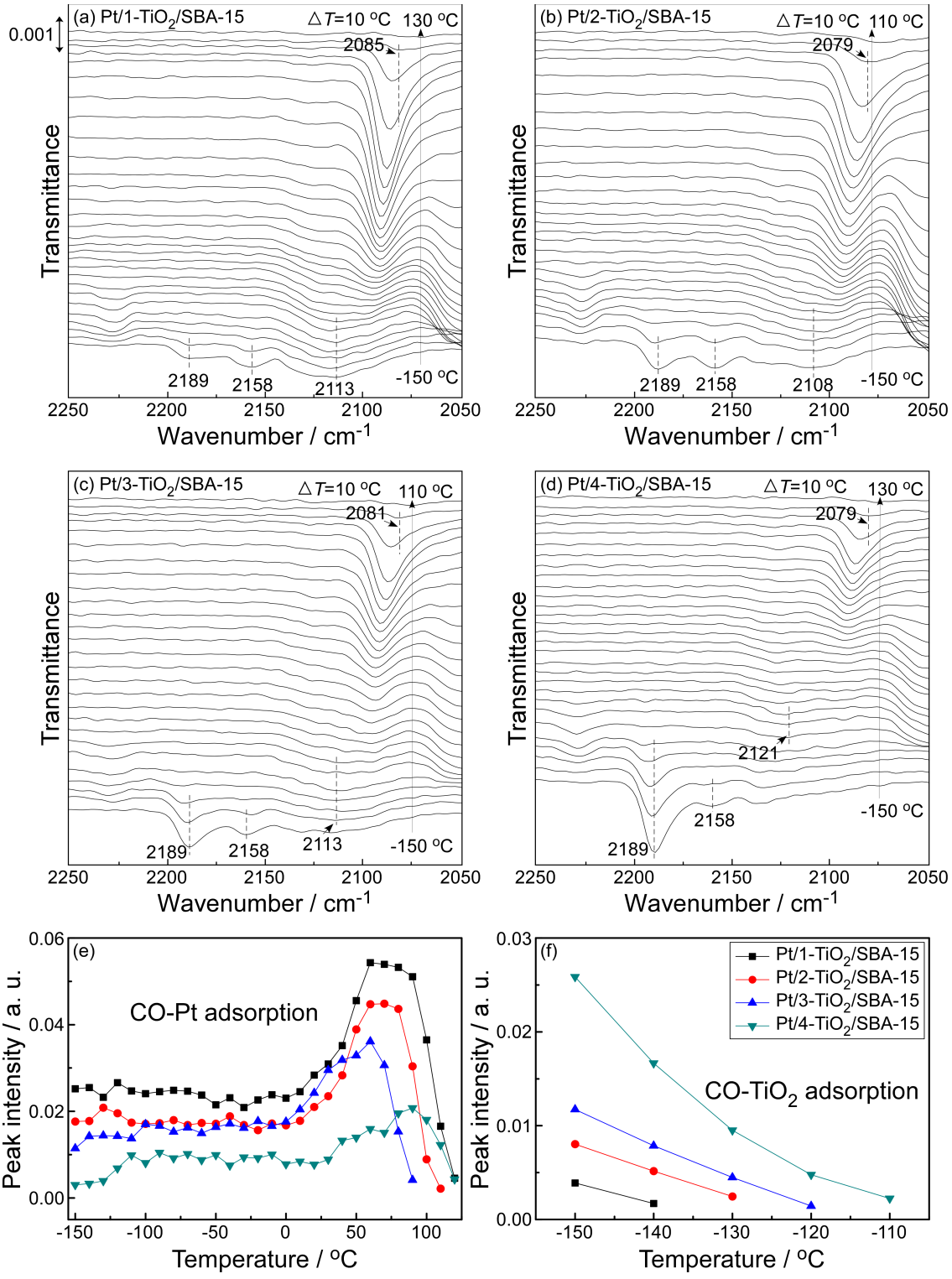

Figure 4.13 CO IR absorption spectra of Pt/(1-4)-TiO_2/SBA-15 (a to d). Peak intensities versus temperature (e, f).

Figure 4.12 displays the IR spectra in the C-O stretching regions as a function of temperature of (1-4)-TiO_2/Pt/SBA-15. The spectra are qualitatively similar to those obtained from Pt/SBA-15 and TiO_2/SBA-15. The peak at 2189-2194 cm^{-1} is assigned to the CO adsorption on TiO_2. This peak intensity increases as the thickness of TiO_2 growing (Figure 4.12f). The feature at 2079-2131 cm^{-1} is associated with CO adsorption on Pt atop sites. The maximum desorption rates of (1-4)-TiO_2/Pt/SBA-15 are seen at approximately 0, 120, 100 and 100 ^oC, respectively (Figure 4.12e). It is worth noting that the peak intensity of CO adsorption on Pt atop sites decreases, while the peak intensity of CO adsorption on TiO_2 increases, as a function of the number of ALD cycles used, owing to the Pt atop sites are covered by TiO_2 films. The shift of the two peaks with temperature increasing is due to the changes in CO surface coverage upon desorption.

Figure 4.13 exhibits the CO IR spectra of Pt/(1-4)-TiO_2/SBA-15. A weak peak at 2158 cm^{-1} is attributed to CO adsorption on silanol groups[72], which is not observed on other catalysts. This peak disappears quickly upon pumping. Other features and trends are similar to (1-4)-TiO_2/Pt/SBA-15. However, since the Pt nanoparticles were deposited after TiO_2 films for Pt/(1-4)-TiO_2/SBA-15, the Pt nanoparticles have more atop sites exposed to CO, leading to more intense peaks of CO adsorption on Pt atop sites (2079-2121 cm^{-1}), compared with (1-4)-TiO_2/Pt/SBA-15. Furthermore, CO adsorption on bridge sites are not seen for either (1-4)-TiO_2/Pt/SBA-15 or Pt/(1-4)-TiO_2/SBA-15.

The Pt and TiO_2 loadings were quantified by ICP-OES as shown in Table 4.2. The measured Pt loading is 1.03 wt.% for Pt/SBA-15, which is very close to the nominal value: 1 wt.%. The Pt loadings of (1-4)-TiO_2/Pt/SBA-15 are lower than Pt/SBA-15, because the

growth of TiO_2 films decreases the weight percent of Pt. It is possible that some Pt particles were not loaded on TiO_2/SBA-15 during the synthetic process of Pt/(1-4)-TiO_2/SBA-15, as the Pt loadings are lower than 1 wt.%. The TiO_2 loadings of (1-4)-TiO_2/Pt/SBA-15 and Pt/(1-4)-TiO_2/SBA-15 are in good agreement with the values of (1-4)-TiO_2/SBA-15, reflecting the good reproducibility of ALD process.

Table 4.2 Pt and TiO_2 loadings of Pt/SBA-15, (1-4)-TiO_2/Pt/SBA-15 and Pt/(1-4)-TiO_2/SBA-15

Sample	Average Pt load (%)	Standard deviation	Average TiO_2 load (%)	Standard deviation
Pt/SBA-15	1.03	0.00	N/A	N/A
1-TiO_2/Pt/SBA-15	0.87	0.00	8.28	0.00
2-TiO_2/Pt/SBA-15	0.70	0.00	14.25	0.00
3-TiO_2/Pt/SBA-15	0.71	0.00	18.98	0.01
4-TiO_2/Pt/SBA-15	0.64	0.00	22.84	0.01
Pt/1-TiO_2/SBA-15	0.79	0.00	8.45	0.00
Pt/2-TiO_2/SBA-15	0.66	0.00	14.14	0.00
Pt/3-TiO_2/SBA-15	0.86	0.00	19.32	0.01
Pt/4-TiO_2/SBA-15	0.69	0.00	23.22	0.00

Furthermore, the Pt and TiO_2 loadings were also confirmed by EDS analysis, as shown in Table 4.3 and 4.4. Although the EDS elemental analysis is less accurate than ICP-OES, since the electron microscope just focuses on a small area of the sample, the data are reasonable and can be used as supplementary evidence. The Pt and TiO_2 loadings are 3.94

and 7.63 wt.% for 1-TiO_2/Pt/SBA-15, and 4.7 and 6.2 wt.% for Pt/1-TiO_2/SBA-15, respectively. The TiO_2 loadings are close to the results obtained by ICP-OES.

Table 4.3 EDS elemental analysis of 1-TiO_2/Pt/SBA-15

Element	Mass (%)	Atom (%)	Relative error (%)
Pt	3.94	0.45	10.70
Ti	7.63	3.52	3.36
O	44.50	61.47	3.06
Si	43.92	34.56	0.21

Table 4.4 EDS elemental analysis of Pt/1-TiO_2/SBA-15

Element	Mass (%)	Atom (%)	Relative error (%)
Pt	4.7	0.5	0.5
Ti	6.2	2.9	0.2
O	43.0	60.0	1.1
Si	46.1	36.6	0.3

4.3.3 Hydrogenation of cinnamaldehyde

The catalytic performance of our samples toward hydrogenation of cinnamaldehyde (CAL) was evaluated. The reaction pathways are shown in Figure 4.14. The unsaturated alcohol (cinnamyl alcohol, COL) is the desired product, namely selective hydrogenation of C=O bond.

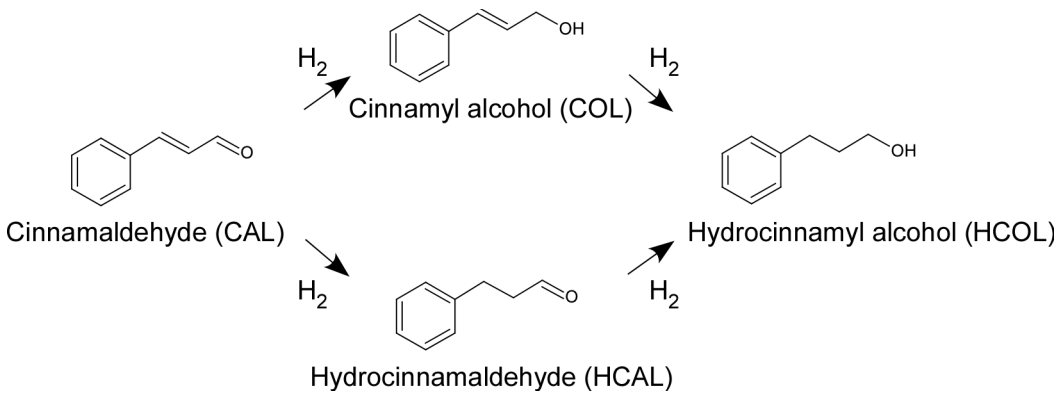

Figure 4.14 Reaction pathways of hydrogenation of CAL.

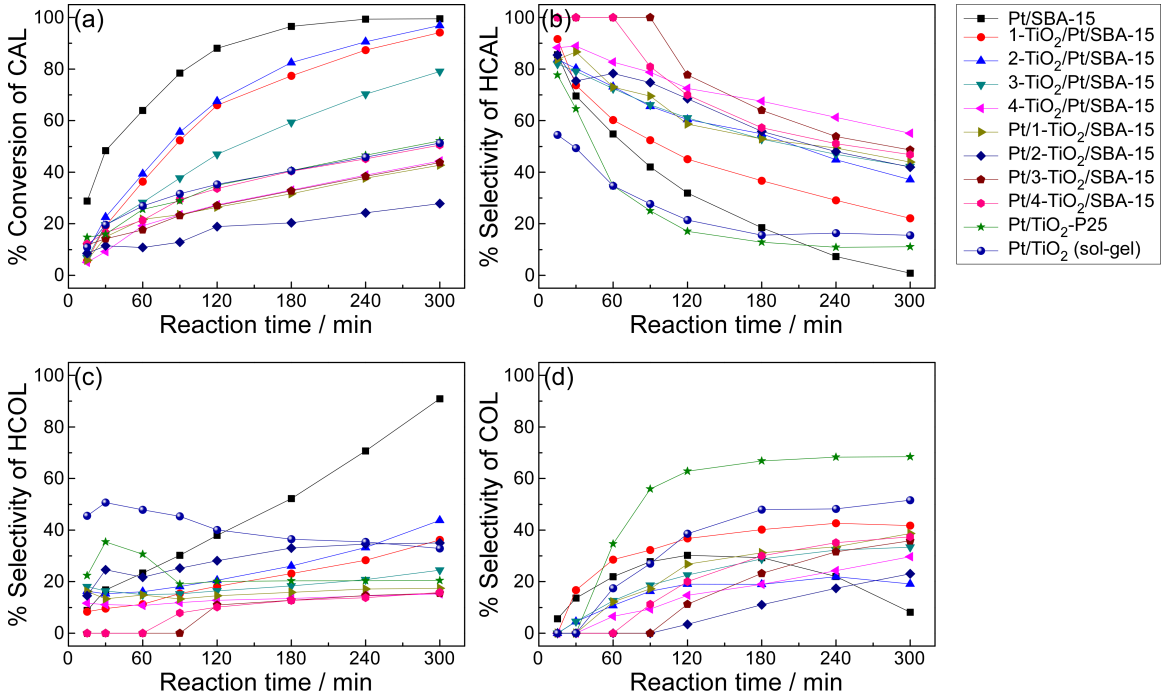

Figure 4.15 % Conversion of CAL (a), % selectivity of HCAL (b), HCOL (c), and COL (d) versus reaction time.

Figure 4.15a shows the conversion of CAL versus reaction time. The Pt/SBA-15 exhibits the best reactivity (over 99% conversion after 240 min). However, this sample shows poor selectivity toward COL (~8% at t=300 min). As seen in Figure 4.15c, CAL was over hydrogenated to hydrocinnamyl alcohol (HCOL). Nevertheless, the Pt/SBA-15 with 1 ALD cycle (1-TiO_2/Pt/SBA-15) shows relatively best conversion of CAL and selectivity of COL (Figure 4.15a and d). The addition of TiO_2 films enhances the selectivity of COL, while decreases the total reactivity. Moreover, all the (1-4)-TiO_2/Pt/SBA-15 and Pt/(1-4)-TiO_2/SBA-15 samples show better selectivity of COL and worse conversion of CAL. It is commonly observed that an increment of selectivity is often accompanied by a certain loss of reactivity. The Pt/TiO_2-P25 and Pt/TiO_2 (sol-gel) were used as reference samples. As seen in Figure 4.16, these two samples exhibit 68% and 51% selectivity toward COL production at t=300 min, which are better than other samples. However, the conversion of CAL are only 52% and 51%, respectively. It confirms that the addition of TiO_2 films can improve the selectivity of COL.

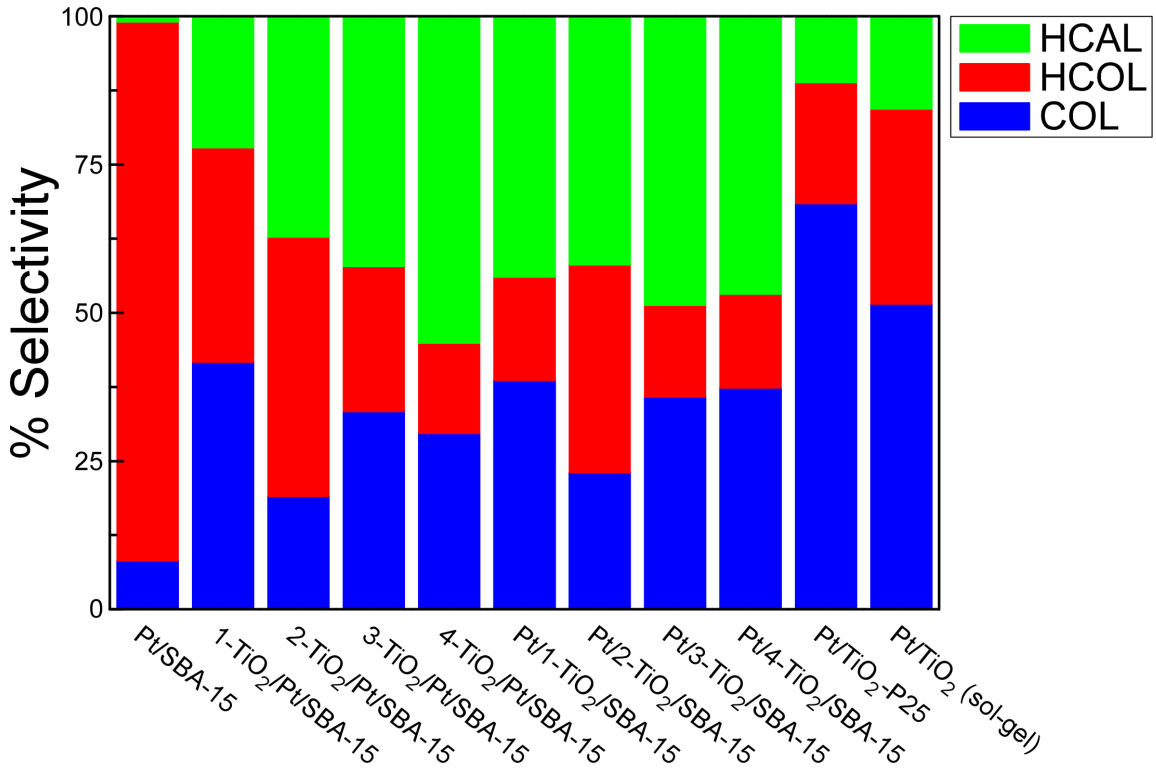

Figure 4.16 % Selectivity of HCAL, HCOL and COL of various catalysts at t=300 min.

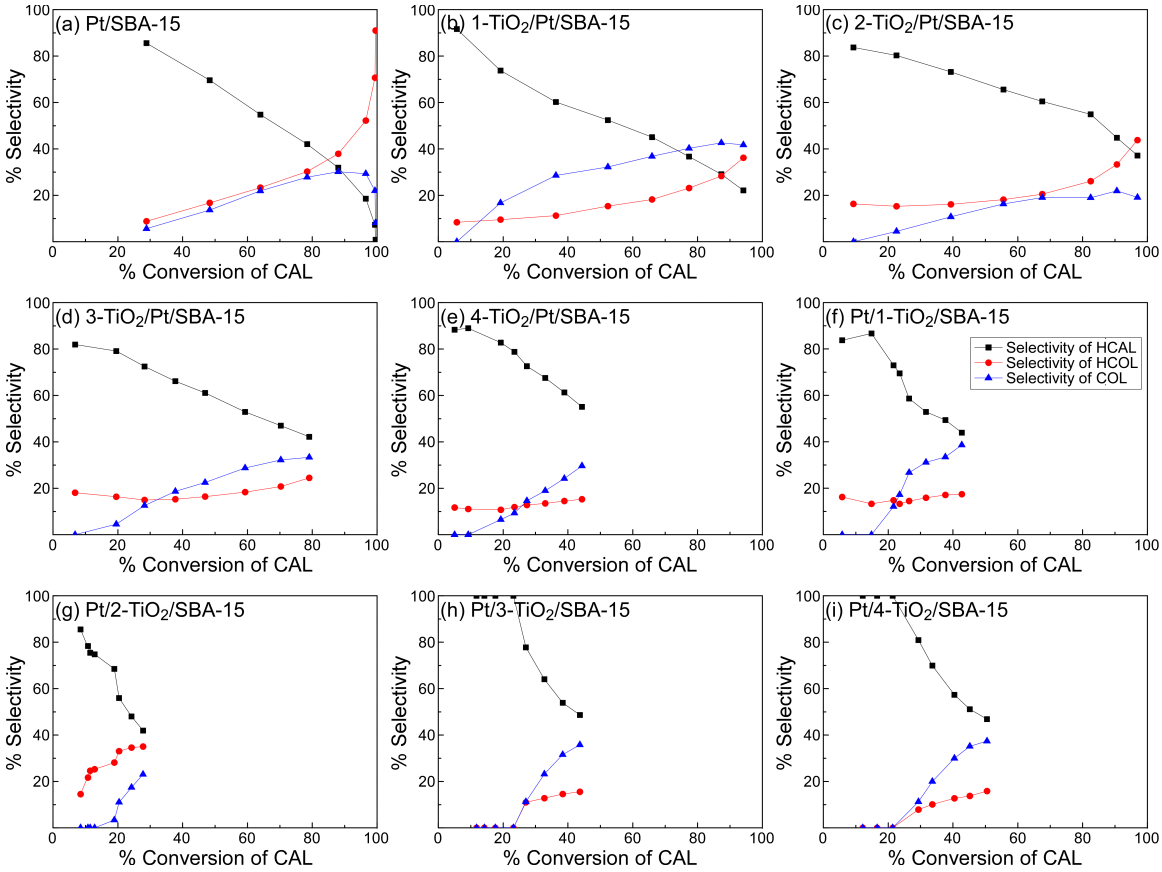

Figure 4.17 Selectivity versus conversion of various catalysts.

The selectivity toward three products and conversion of CAL is plotted in Figure 4.17. The saturated alcohol (HCOL) and unsaturated aldehyde (hydrocinnamaldehyde, HCAL) were produced at the beginning of the reaction. The selectivity of HCAL decreased and the selectivity of COL increased as the reaction was going on. For Pt/SBA-15, a great amount of COL was converted to HCOL after 180 min. However, the production toward HCOL is suppressed after the addition of TiO_2 films.

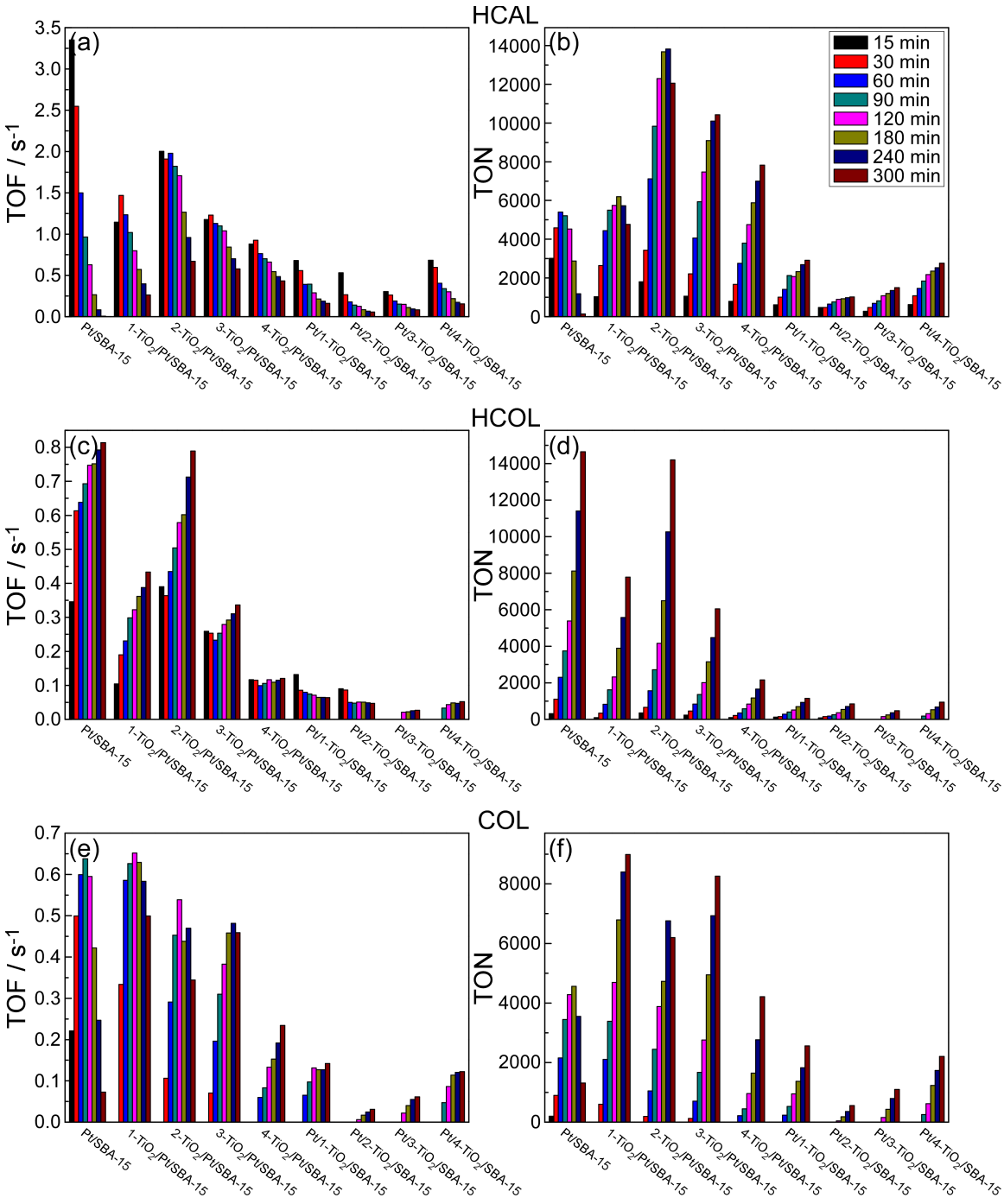

Figure 4.18 TOFs (a, c and e) and TONs (b, d and f) of HCAL, HCOL and COL for various catalysts as a function of reaction time.

Turnover frequencies (TOFs) and turnover numbers (TONs) of various samples as a function of reaction time are shown in Figure 4.18. Figure 4.18 shows the similar trends as Figure 4.15. It is more clearly to see that the 1-TiO_2/Pt/SBA-15 exhibits the best selectivity toward COL production, and the saturated alcohol (HCOL) was catalyzed by Pt/SBA-15 the most. Furthermore, the overall reactivity and selectivity of COL decrease with increasing TiO_2 film thickness. This indicates that the Pt surface atoms may be covered by the TiO_2 films, and the dissociation of H_2 is inhibited. Finally, the Pt/(1-4)-TiO_2/SBA-15 do not show either excellent conversion of CAL or selectivity of COL, suggesting that these samples are not promising for hydrogenation of CAL.

The enhancement of selectivity toward COL production can be attributed to the creation of acidic sites which were probed by pyridine. In the C=O bond, the C end is positively charged, while the O end is electron-rich[42]. Therefore, positively charged centers in the catalysts, such as Brønsted and Lewis acidic sites, can promote the polarization and activation of C=O bond[32,72]. Additionally, the electron-transfer mechanism between the reducible TiO_2 and Pt nanoparticles is also responsible for the enhanced hydrogenation of C=O bond[4].

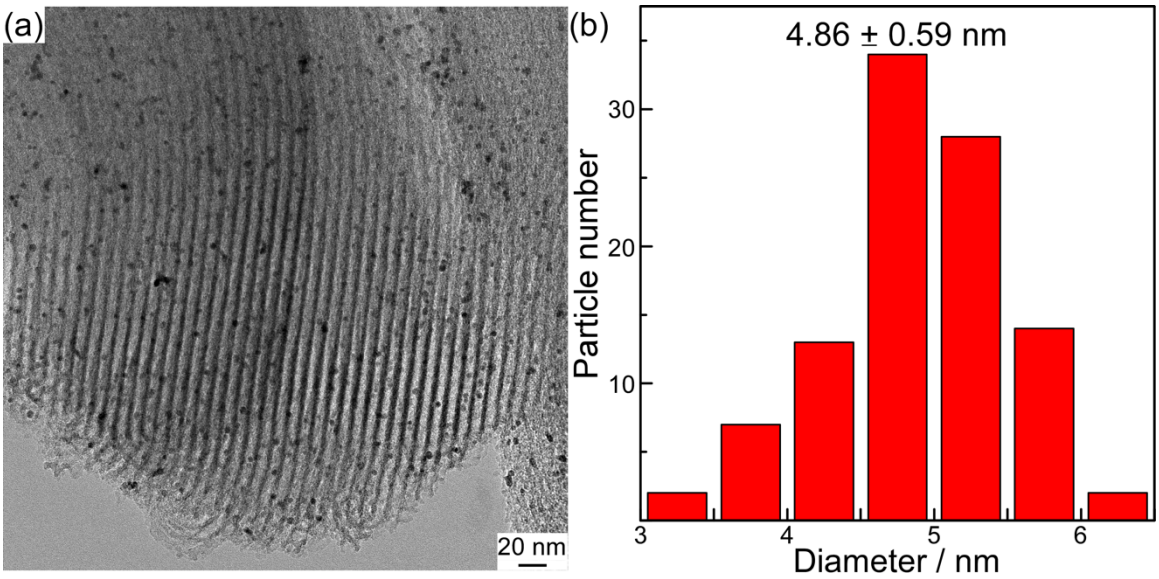

Figure 4.19 (a) TEM image. (b) Pt nanoparticle size distributions of 1-TiO_2/Pt/SBA-15 after 3 catalytic runs.

The 1-TiO_2/Pt/SBA-15 was selected to run the catalytic reaction for three continuous times to investigate the reusability of the sample. The TEM images were obtained after 3 catalytic runs, and Pt nanoparticle size distributions were estimated from the images. As seen in Figure 4.20, the Pt nanoparticles were still well-dispersed in the pores of SBA-15, and no nanoparticle aggregation or sintering were observed after 3 catalytic runs. The average diameter of Pt nanoparticles is approximately 4.86 nm. The nanoparticle size fluctuation is because of experiment error. The TEM images were taken from different batches of samples. The TEM results reflect the excellent reusability of our catalysts.

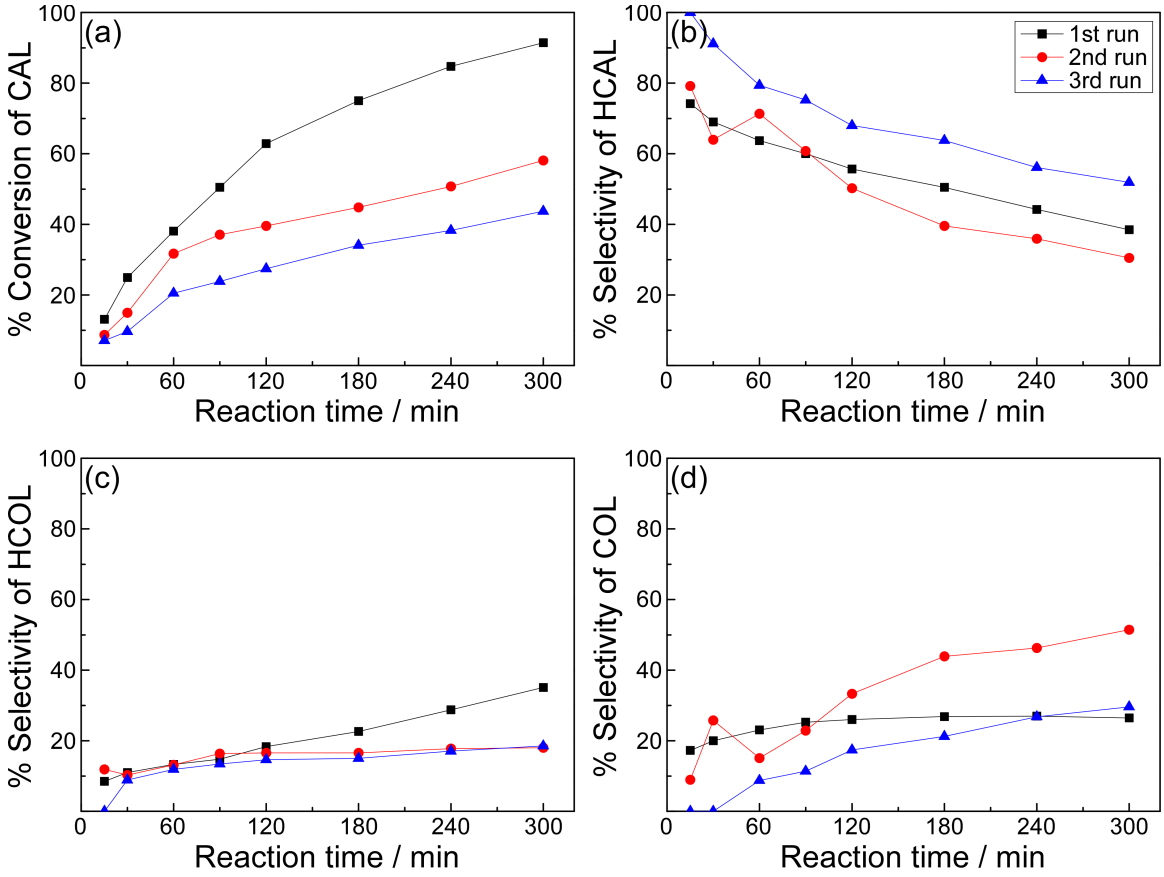

Figure 4.20 % Conversion of CAL (a), % selectivity of HCAL (b), HCOL (c), and COL (d) versus reaction time of 1-TiO_2/Pt/SBA-15 for 3 catalytic runs.

The kinetic data were shown in Figure 4.21 and Figure 4.22. The conversion (Figure 4.21a) and TOFs (Figure 4.22a) reduction is due to the loss of sample (~3 mg each run) and poisoning. However, the selectivity of COL increases in the second catalytic run, and even maintains the same level in the third catalytic run after 240 min. The TOFs and TONs toward COL production are also better in the second run at t=300 min.

It is worth noting that the 1-TiO_2/Pt/SBA-15 shows prominent reusability in hydrogenation of CAL. Two main reasons may be responsible for the enhanced reusability: (1) encapsulation of Pt nanoparticles inside the pores of SBA-15; (2) immobilization of Pt

nanoparticles by TiO_2 films. Mesoporous SBA-15 and TiO_2 films stabilize the Pt nanoparticles and prevent nanoparticle sintering. In addition, SMSI effect may also contribute to the enhanced stability. Owing to SMSI effect, TiO_2 species migrate to the perimeter of Pt nanoparticles, and further improve the stability of Pt nanoparticles.

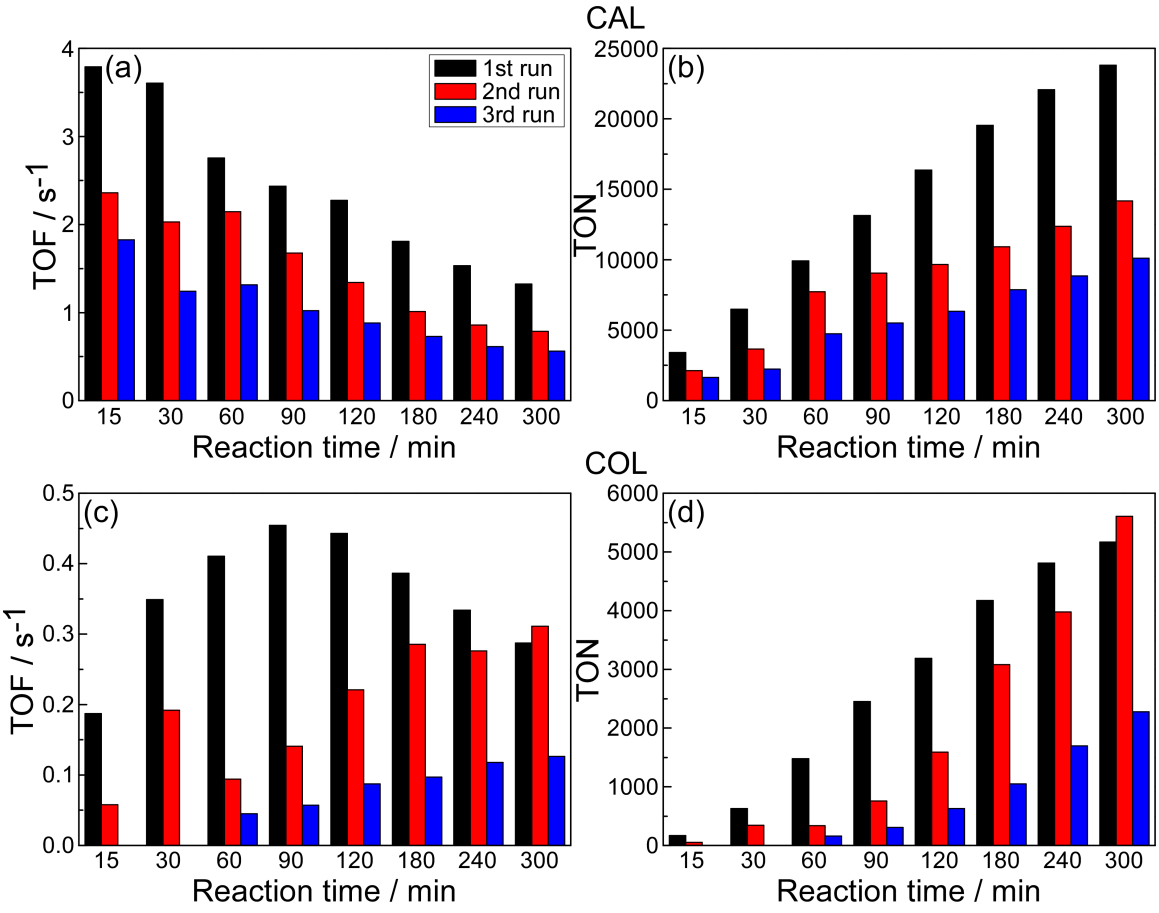

Figure 4.21 TOFs (a, c) and TONs (b, d) of CAL and COL versus reaction time of 1-TiO_2/Pt/SBA-15 for 3 catalytic runs.

4.3.4 CO oxidation

The kinetic studies of CO oxidation are displayed in Figure 4.23. The Pt/SBA-15 shows the worst reactivity, while Pt/4-TiO_2/SBA-15 exhibits twice higher reaction rate than

Pt/SBA-15. All the (1-4)-TiO_2/Pt/SBA-15 and Pt/(1-4)-TiO_2/SBA-15 samples show better catalytic performance than Pt/SBA-15, indicating that TiO_2 films greatly improve the reactivity. The main reason is attributed to the Pt-TiO_2 interface. By introducing TiO_2 films, a large amount of oxygen vacancies at the perimeter interface between reducible TiO_2 and Pt nanoparticles were created[51]. The oxygen vacancies act as active sites and promote the reaction[73,74]. Furthermore, the lattice oxygen of reducible TiO_2 located at the interface is involved in the reaction and is responsible for the enhanced reactivity. Finally, the reaction rates decrease as a function of reaction time. The highest reaction rate was obtained in the initial stage of the reaction (before t=20 min). All the samples exhibit similar trends for TOFs and TONs versus reaction time.

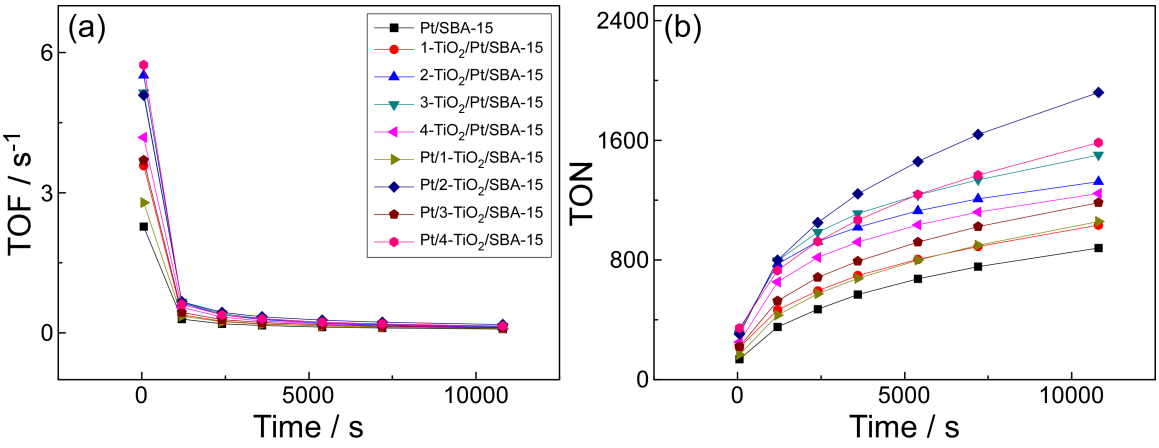

Figure 4.22 (a) TOFs and (b) TONs for CO oxidation versus reaction time.

4.4 Conclusions

The Pt nanoparticles were successfully deposited into the pores of SBA-15 using colloidal method. PVP plays an important role in stabilizing and preventing aggregation of Pt nanoparticles, and it can be removed by calcination. TiO_2 films were deposited afterward

onto Pt/SBA-15 followed the same procedure in Chapter 3. Moreover, Pt/(1-4)-TiO_2/SBA-15 catalysts were successfully synthesized by a DP method. Neither Pt nanoparticles nor TiO_2 films change the mesoporous structure of SBA-15. TEM and EDS results confirm that the Pt nanoparticles are well-dispersed in all the samples.

As probed by CO IR absorption spectra, active sites for both Pt and TiO_2 are present. CO adsorption on both Pt atop sites and bridge sites are observed for Pt/SBA-15. For (1-4)-TiO_2/Pt/SBA-15, the signal intensities of Pt atop sites decrease as increasing number of ALD cycles. The CO adsorption on Pt of Pt/(1-4)-TiO_2/SBA-15 is stronger than (1-4)-TiO_2/Pt/SBA-15, since the former ones are not covered by TiO_2 films.

The Pt and TiO_2 loadings were estimated by ICP-OES and EDS. The nominal Pt loading (1 wt.%) is very close to the values measured by ICP-OES. The TiO_2 loadings are in good agreement with TiO_2/SBA-15 samples.

The catalytic performance was evaluated by hydrogenation of CAL and CO oxidation. 1-TiO_2/Pt/SBA-15 exhibits relatively the best conversion of CAL and selectivity of COL. Addition of TiO_2 films can improve the selectivity toward COL production. The enhanced catalytic performance is attributed to the creation of acidic sites and the changes of reactant adsorption modes. All the (1-4)-TiO_2/Pt/SBA-15 and Pt/(1-4)-TiO_2/SBA-15 samples show higher TOFs of CO_2 than Pt/SBA-15, suggesting the addition of TiO_2 can promote CO oxidation. Oxygen vacancies created in the interface between the reducible TiO_2 films and Pt nanoparticles is responsible for the raised reaction rate.

1-TiO_2/Pt/SBA-15 also shows excellent stability after 3 cycles of reaction. No visible morphology change can be seen in the TEM images. Encapsulation of Pt nanoparticles

inside the pores of SBA-15, ALD-TiO_2 overcoating of Pt nanoparticles and SMSI effect all contribute to the enhanced stability.

Chapter 5 Synthesis, characterization and catalytic performance studies of supported Au nanocatalysts

5.1 Introduction

In this chapter, TiO_2 films and Au nanoparticles were deposited in two possible sequences, similar to Pt nanocatalysts. TEM, IR, ICP-OES, N_2 adsorption-desorption isotherms were utilized to characterize the supported Au nanocatalysts. Au/TiO_2 (sol-gel) and commercial Au/TiO_2 (anatase) were used as reference samples. Catalytic performance was evaluated by hydrogenation of CAL and oxidation of benzyl alcohol reactions.

5.2 Experimental

5.2.1 Synthesis of bis(ethylenediamine) gold (III) chloride - $Au(en)_2Cl_3$

The commonly used DP method for synthesizing Au/TiO_2 catalysts does not work for SBA-15 support. Therefore, a more effective method using a gold cationic complex precursor $[Au(en)_2]^{3+}$ (en=enthylenediamine) was employed[75,76]. The gold cationic precursor was immobilized on negatively charged SBA-15 surface that utilizing the deprotonation reaction of ethylenediamine ligands.

Aqueous solution of $HAuCl_4 \cdot 3H_2O$ was prepared by dissolving 1.0 g of $HAuCl_4 \cdot 3H_2O$ in 10 mL of DI water. 0.45 mL of ethylenediamine was slowly added into the as-prepared $HAuCl_4 \cdot 3H_2O$ aqueous solution. The solution was stirred for 30 min. Subsequently, 70 mL of ethanol was added into the solution and precipitation formed immediately. The product

was filtered, washed by ethanol, and dried overnight under vacuum. The as-prepared $Au(en_2)Cl_3$ powder must be stored in a glove box.

5.2.2 Synthesis of Au/SBA-15 and Au/(1-4)-TiO_2/SBA-15

10.86 mg of $Au(en)_2Cl_3$ was dissolved in 60 mL of DI water. The pH value of the solution was adjusted to 10 by 1.0 mol/L NaOH solution. 0.5 g of support (SBA-15 or TiO_2/SBA-15) was added into the solution. Since the pH value dropped, the final pH value of the solution was adjusted to 9.5 by further addition of the NaOH solution. The suspension was stirred for 2 h. The product was filtered, washed with 300 mL of water and dried under vacuum for 24 h. The final product was reduced under H_2 at 250 ^oC for 3 h.

5.2.3 Synthesis of (1-4)-TiO_2/Au/SBA-15

The as-prepared Au/SBA-15 was used as support. The deposition of TiO_2 followed the same procedure in Chapter 3.

5.2.4 Synthesis of Au/TiO_2 (sol-gel)

The synthesis of Au/TiO_2 (sol-gel) employed a DP-urea method[53]. Typically, 1.025 mL of 0.01 mol/L $HAuCl_4$ solution, 0.0631 g of urea and 0.2 g of TiO_2 (sol-gel) were mixed in 20 mL of DI water. The mixture was stirred for 4 h. Then the product was centrifuged, washed by water, dried overnight and calcined under H_2 at 150 ^oC for 2 h.

5.2.5 Functionalization of SBA-15 with APTES

1 g of SBA-15, 3.2 mL of APTES and 30 mL of toluene were mixed in a flask. The slurry was refluxed at 80 ^oC for 3 h with magnetic stirring. The product was centrifuged and dried.

5.2.6 Synthesis of Au/SBA-15 with APTES functionalized SBA-15

0.1 g of APTES functionalized SBA-15 and 0.5128 mL of 0.01 mol/L $HAuCl_4$ solution were mixed in 10 mL of DI water. Then $NaBH_4$ solution (0.04 mmol of $NaBH_4$ in 10 mL of DI water) was added into the slurry dropwise, followed by magnetic stirring for 30 min. The product was centrifuged and dried.

5.2.7 Synthesis of Au/SBA-15 with $NaBH_4$ as reducing agent

10.86 mg of $Au(en)_2Cl_3$ was dissolved in 60 mL of DI water. The pH value of the solution was adjusted to 10 by 1.0 mol/L NaOH solution. 0.5 g of SBA-15 was added into the solution. The final pH value of the solution was adjusted to 9.5 by further addition of the NaOH solution. The slurry was stirred for 2 h. Then $NaBH_4$ solution (0.04 mmol of $NaBH_4$ in 10 mL of DI water) was added into the slurry dropwise, followed by magnetic stirring for 2 h. The product was centrifuged, washed and dried.

5.2.8 Hydrogenation of CAL

The reaction conditions of hydrogenation of CAL are the same as Chapter 4.

5.2.9 Oxidation of benzyl alcohol

20 mg of catalysts without any pretreatment were mixed with 20 mL of toluene (solvent), 300 μL of benzyl alcohol and 300 μL of dodecane (internal standard) in the reactor vessel. The vessel was purged with O_2 for 10 min and sealed. The reaction was running at 120 ^oC at atmospheric pressure with stirring (1000 rpm). Aliquots were taken at preset times and analyzed by GC.

5.3 Results and discussion

5.3.1 Characterization of (0-4)-TiO_2/Au/SBA-15 and Au/(1-4)-TiO_2/SBA-15

The mesoporous structure of the supported Au nanocatalysts was primarily studied by N_2 adsorption-desorption isotherms, the Au nanocatalysts exhibit similar trends as Pt nanocatalysts. As shown in Figure 5.1a and b, the mesoporous structure was retained after the deposition of Au and TiO_2, because the hysteresis loops are not affected. Since the desorption branch can better reflect the reality, pore diameter, pore volume and pore size distributions estimated from desorption branch are plotted. Narrow pore size distributions are seen in Figure 5.1c and d, and the pore diameter decreases linearly with increasing the number of ALD cycles, indicating the uniform growth of the TiO_2 films. The surface area and pore volume decrease monotonically as a function of the number of ALD cycles (Figure 5.1e and f).

Figure 5.2 displays the TEM images and Au nanoparticle distributions of Au/SBA-15. The diameter of the Au nanoparticles is approximately 5.18 nm. The Au nanoparticles are well-dispersed and incorporated in the pores of SBA-15. The Au nanoparticles are primarily located inside the channels, though the possibility of Au nanoparticles located outside cannot be ruled out. The deposition of Au nanoparticles does not destroy the mesoporous structure of SBA-15.

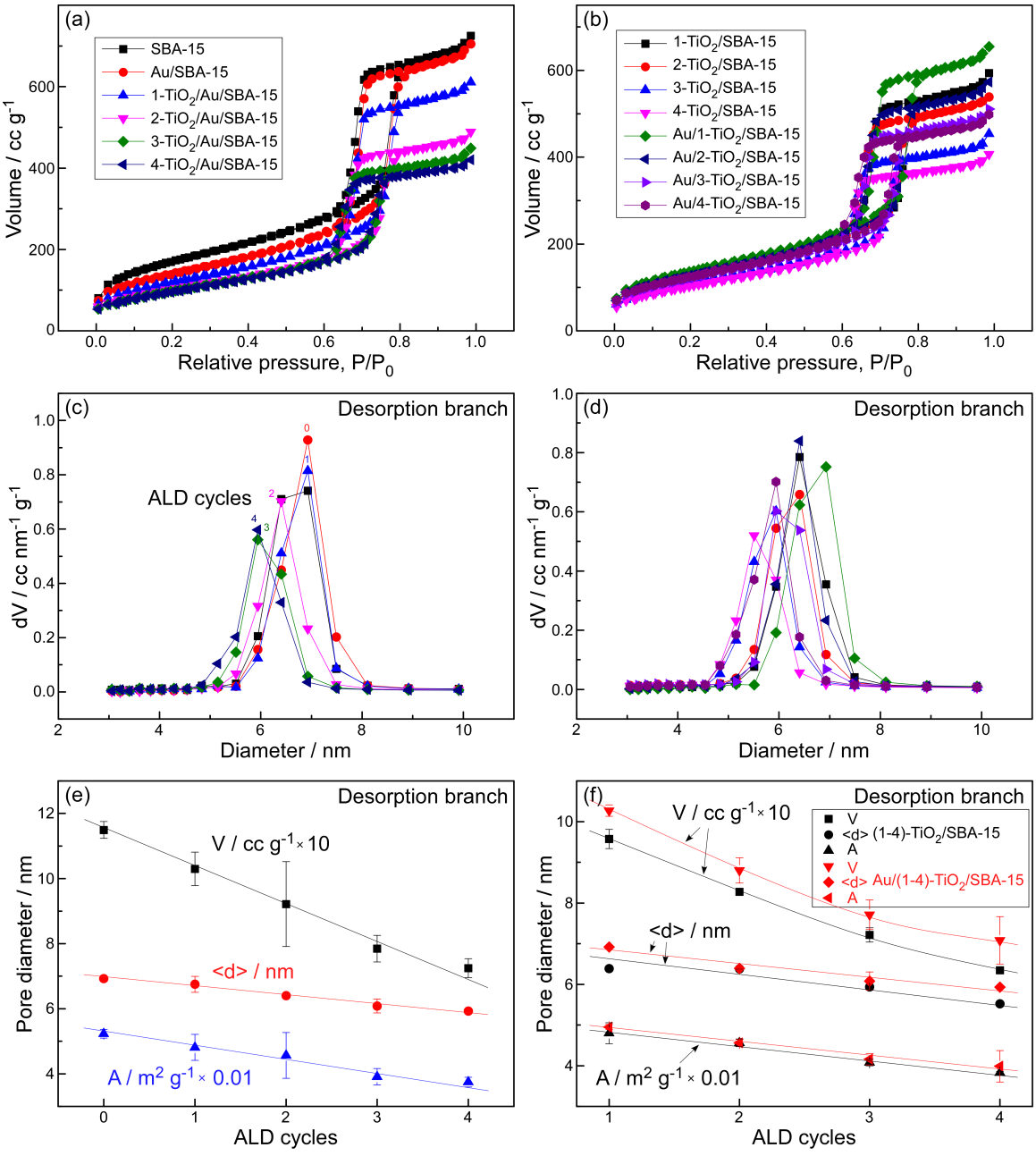

Figure 5.1 (a, b) N_2 adsorption-desorption isotherms. (c, d) Pore size distributions, (e, f) <d>, V, and A, estimated from desorption branch, of (1-4)-TiO_2/Au/SBA-15 and Au/(1-4)-TiO_2/SBA-15. SBA-15, Au/SBA-15 and (1-4)-TiO_2/SBA-15 are used as reference samples. Data are reported as a function of the number of ALD cycles used.

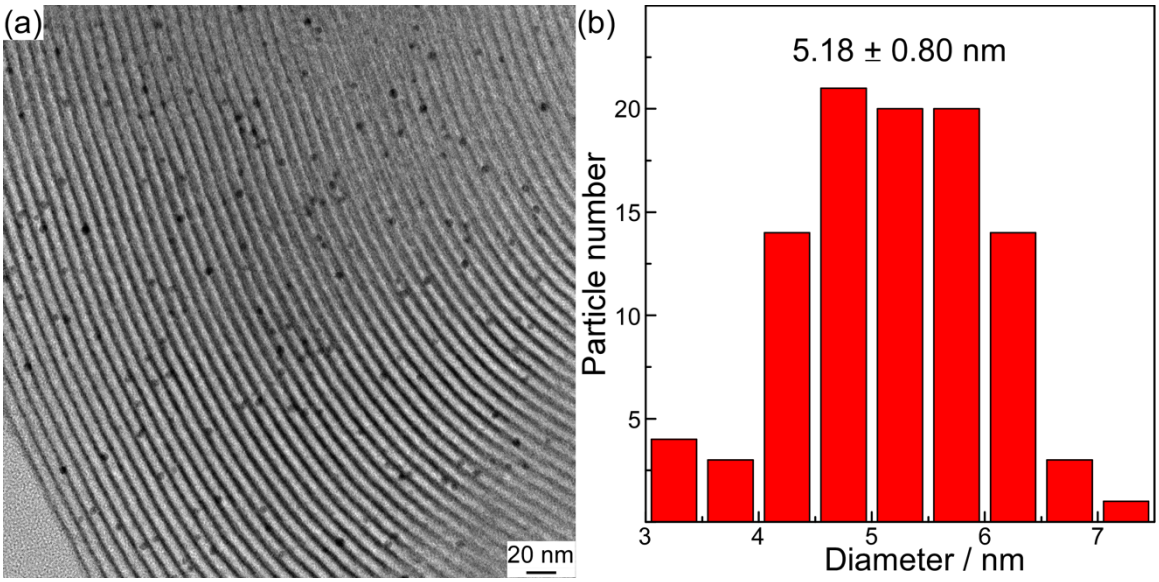

Figure 5.2 (a) TEM image. (b) Au nanoparticle size distributions of Au/SBA-15.

Figure 5.3 displays the TEM images and Au nanoparticle size distributions of (1-4)-TiO_2/Au/SBA-15. The diameters of Au nanoparticles of (1-4)-TiO_2/Au/SBA-15 are 5.60, 5.38, 5.46 and 6.17 nm, respectively. The Au nanoparticle sizes and distributions of (1-4)-TiO_2/Au/SBA-15 are similar to Au/SBA-15 support, suggesting that the deposition of TiO_2 films does not change the morphology too much. The Au nanoparticles are still mainly located inside the channels.

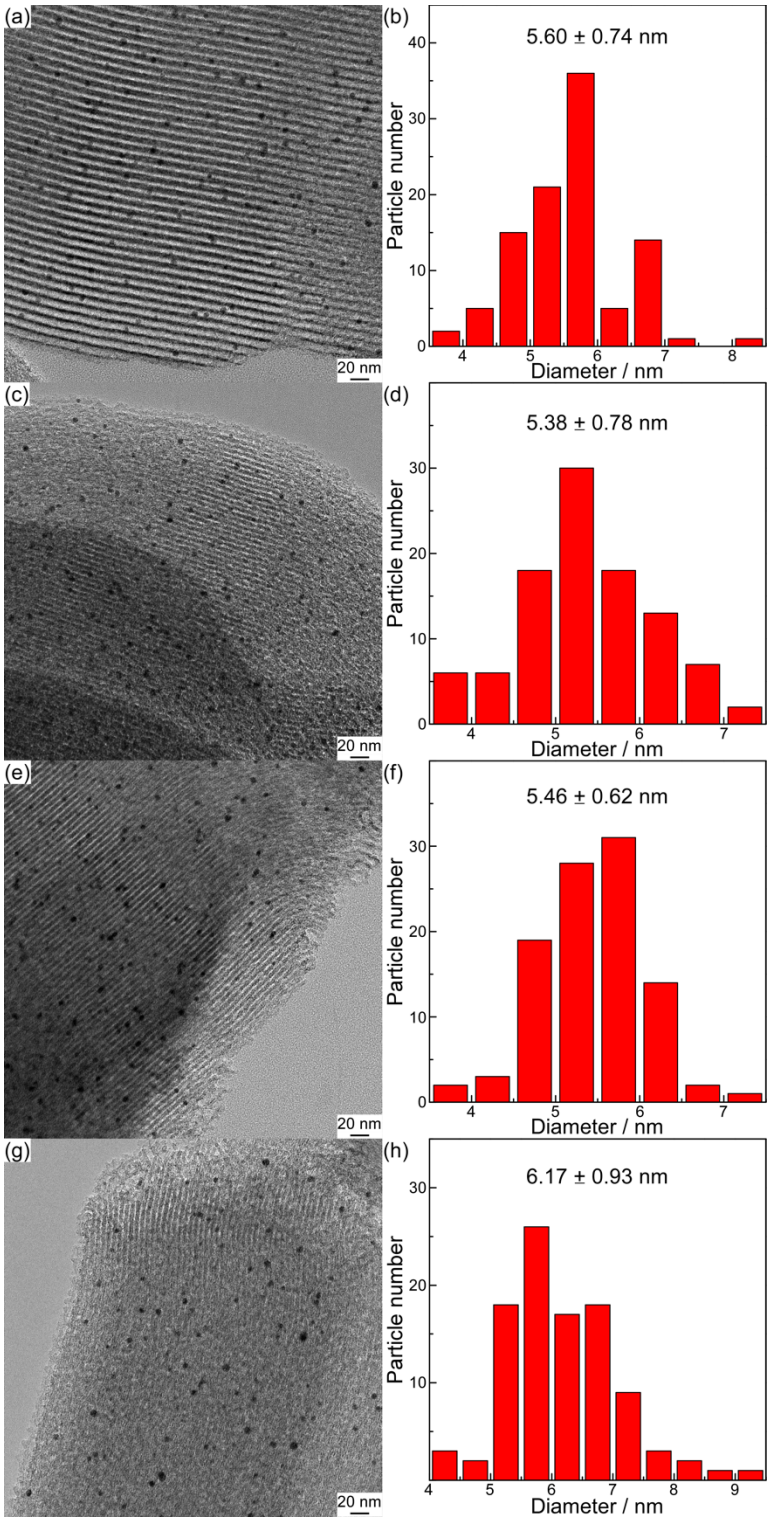

Figure 5.3 TEM images and Au nanoparticle size distributions of (a, b) 1-TiO_2/Au/SBA-15, (c, d) 2-TiO_2/Au/SBA-15, (e, f) 3-TiO_2/Au/SBA-15 and (g, h) 4-TiO_2/Au/SBA-15.

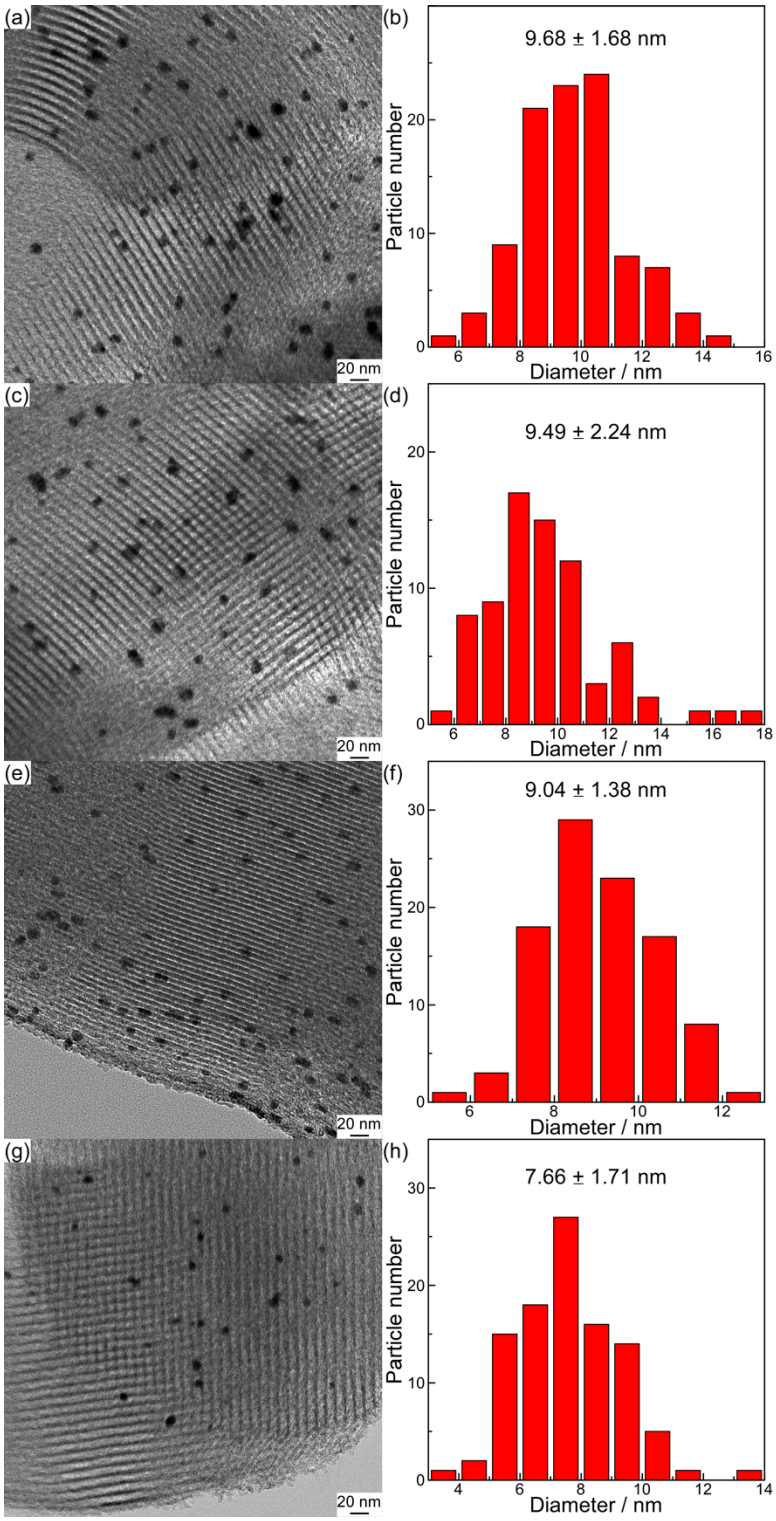

Figure 5.4 TEM images and Au nanoparticle size distributions of (a, b) Au/1-TiO_2/SBA-15, (c, d) Au/2-TiO_2/SBA-15, (e, f) Au/3-TiO_2/SBA-15 and (g, h) Au/4-TiO_2/SBA-15.

Figure 5.4 shows the TEM images and Au nanoparticle size distributions of Au/(1-4)-TiO_2/SBA-15. The diameters of Au nanoparticles of Au/(1-4)-TiO_2/SBA-15 are 9.68, 9.49, 9.04, and 7.66 nm, respectively, which are larger than other catalysts. The Au nanoparticles might occupy the cylindrical pores of SBA-15, and located outside of the channels. The Au nanoparticles are still relatively uniformly dispersed, but the synthesis of Au/(1-4)-TiO_2/SBA-15 using $Au(en)_2Cl_3$ as precursor is less effective for TiO_2 modified SBA-15 support.

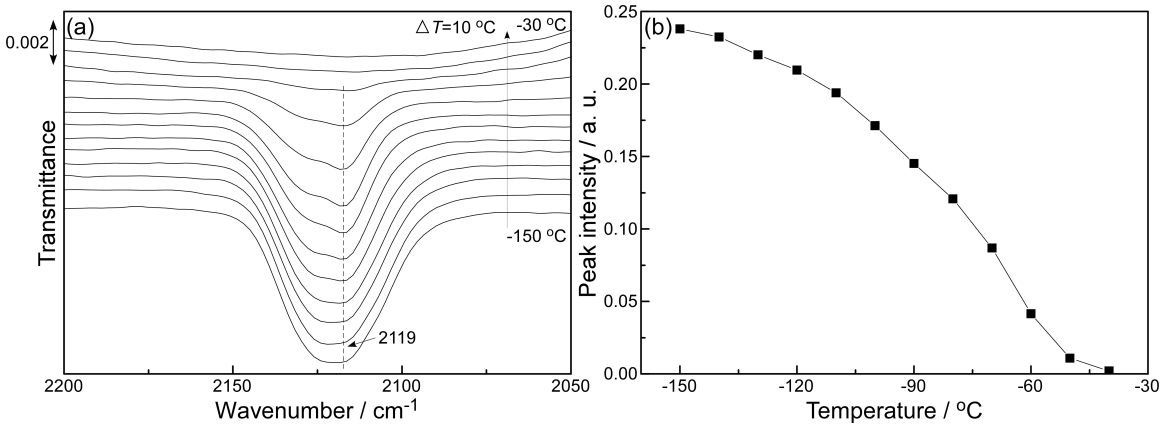

Figure 5.5 (a) CO IR absorption spectrum of Au/SBA-15. (b) Peak intensities versus temperature.

Surface active sites were investigated by CO IR absorption spectroscopy. As seen in Figure 5.5a, the peak at 2119 cm^{-1} was assigned to CO linear adsorption on metallic Au (CO-Au^0)[77]. It is worth noting that a weak shoulder peak at higher frequency (~2123 cm^{-1}), especially from -90 to -60 °C, can be observed. This peak is possibly associated with CO adsorption on $Au^{\delta+}$ species or metallic Au too[78,79]. The peak intensities decrease monotonically as a function of temperature. CO molecules entirely desorb from Au surface at -30 °C, which is much lower than CO adsorption on Pt. It reveals that CO adsorption on Pt is stronger on Pt surface than Au.

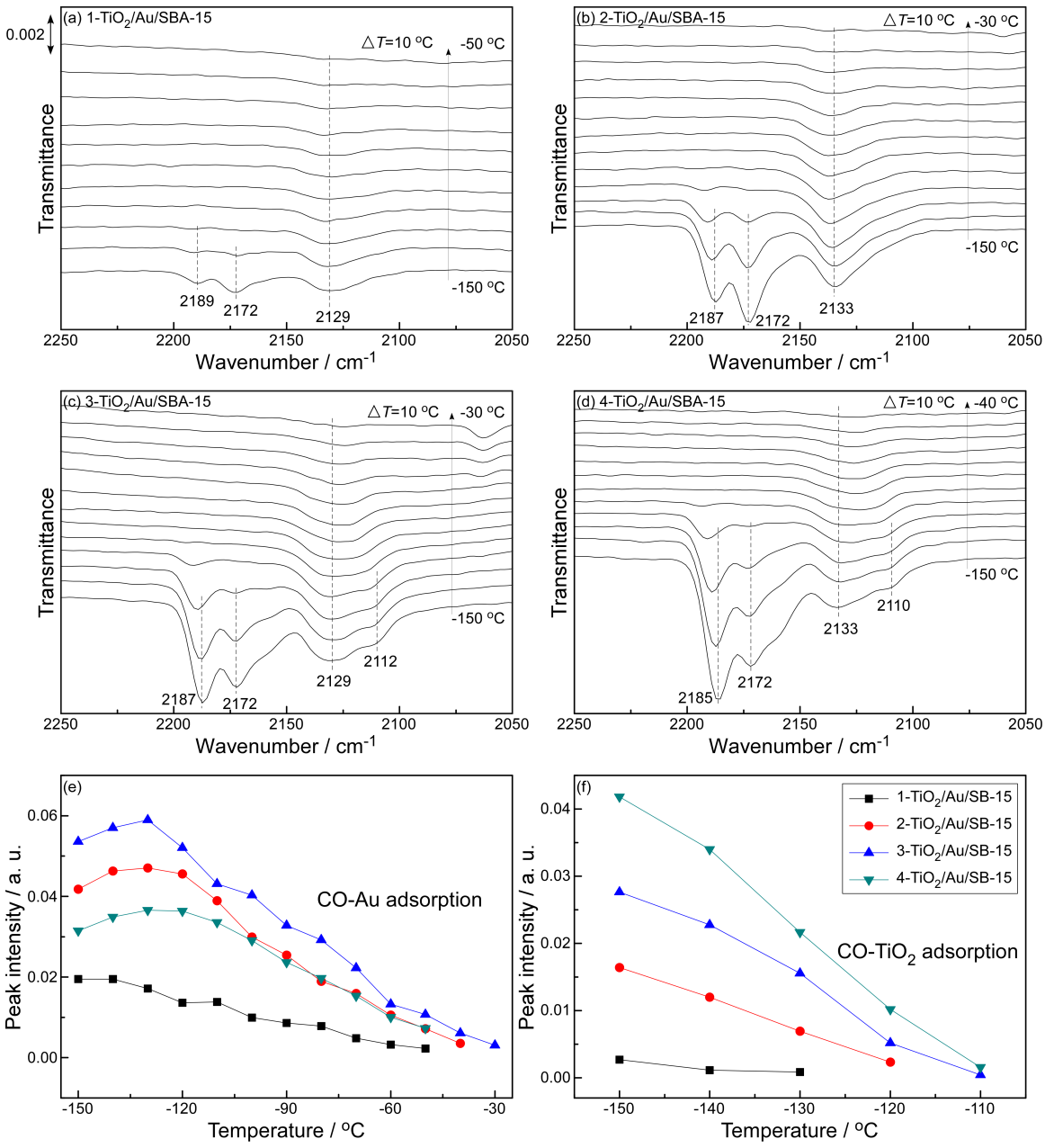

Figure 5.6 CO IR absorption spectra of (1-4)-TiO_2/Au/SBA-15 (a to d). Peak intensities versus temperature (e, f).

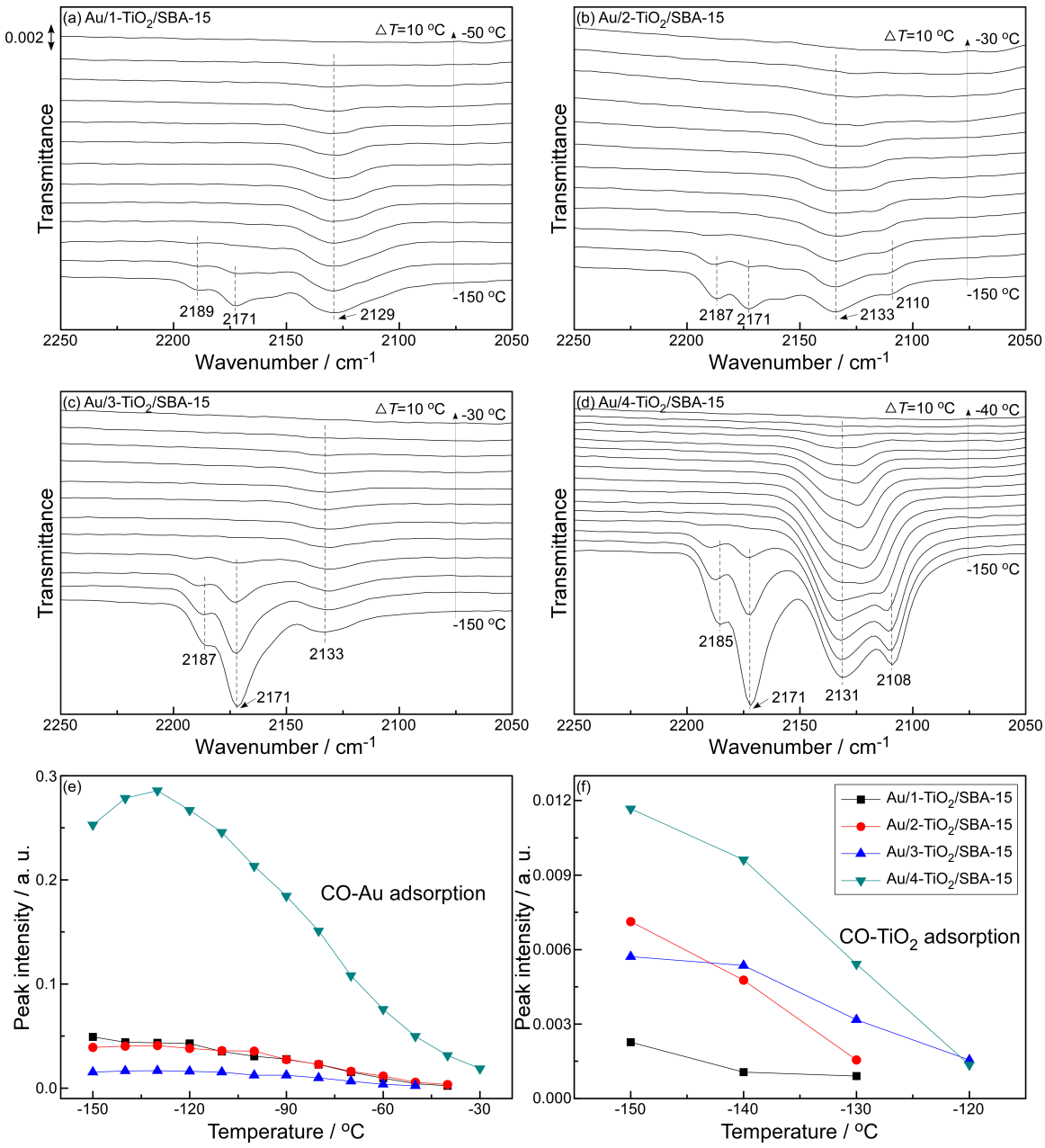

Figure 5.7 CO IR absorption spectra of Au/(1-4)-TiO_2/SBA-15 (a to d). Peak intensities versus temperature (e, f).

Figure 5.6 displays the CO IR absorption spectra of (1-4)-TiO_2/Au/SBA-15. The feature at approximately 2187 cm^{-1} is attributed to CO adsorption on TiO_2, which is consistent with the previous results. The peak at 2172 cm^{-1} is assigned to adsorbed CO interacting with nearby H_2O or OH groups[80,81]. The peak at approximately 2129 cm^{-1} is associated with CO linear adsorption on Au^0. This peak shifts to higher frequency compared with Au/SBA-15, which might due to the modification of TiO_2 films. Again, the weak shoulder peak at 2110-2112 cm^{-1}, especially for 3 and 4 ALD cycles, is corresponding to CO adsorption on $Au^{\delta+}$. Although the peak assignments for the latter two peaks are in dispute, the latter two peaks can be both assigned to CO adsorption on Au nanoparticles. The peak intensities of CO adsorption on Au exhibit a maximum value for 3-TiO_2/Au/SBA-15. It is surprising that the peak intensities do not decrease as a function of the number of ALD cycles (Figure 5.6e). Furthermore, the desorption temperatures are lower than Pt nanocatalysts, indicating weaker CO adsorption on Au than Pt. Nevertheless, the peak intensities of CO adsorption on TiO_2 increase monotonically with increasing number of ALD cycles. The desorption temperatures are similar to TiO_2/SBA-15.

Figure 5.7 shows the CO IR absorption spectra of Au/(1-4)-TiO_2/SBA-15, which is similar to Figure 5.6. The features at approximately 2187, 2171, 2131 and 2108 cm^{-1} are assigned to CO adsorption on TiO_2, OH groups, Au^0 and $Au^{\delta+}$, respectively. Again, the signal between 2070 and 2150 cm^{-1} is not clear yet. Both peaks are attributed to CO adsorption on Au nanoparticles.

Table 5.1 Au and TiO_2 loadings of Au/SBA-15, (1-4)-TiO_2/Au/SBA-15 and Au/(1-4)-TiO_2/SBA-15

Sample	Average Au load (%)	Standard deviation	Average TiO_2 load (%)	Standard deviation
Au/SBA-15	1.01	0.00	N/A	N/A
1-TiO_2/Au/SBA-15	0.86	0.00	8.87	0.01
2-TiO_2/Au/SBA-15	0.78	0.00	14.90	0.02
3-TiO_2/Au/SBA-15	0.72	0.00	17.65	0.02
4-TiO_2/Au/SBA-15	0.64	0.00	22.87	0.00
Au/1-TiO_2/SBA-15	1.01	0.00	9.56	0.00
Au/2-TiO_2/SBA-15	0.96	0.00	15.02	0.01
Au/3-TiO_2/SBA-15	0.98	0.00	19.63	0.01
Au/4-TiO_2/SBA-15	1.05	0.00	24.44	0.01

The Au and TiO_2 loadings were measured by ICP-OES, as shown in Table 5.1. The nominal Au loading of all the samples are 1 wt.%. The measured values of Au/SBA-15 and Au/(1-4)-TiO_2/SBA-15 are very close to 1 wt.%, while the measured Au loadings of (1-4)-TiO_2/Au/SBA-15 are lower than 1 wt.%, because the addition of TiO_2 films increases the total mass. The TiO_2 loadings of (1-4)-TiO_2/Au/SBA-15 and Au/(1-4)-TiO_2/SBA-15 are in good agreement with the results in Chapter 3 and 4, reflecting good reproducibility of the ALD experiment.

5.3.2 Hydrogenation of cinnamaldehyde

The catalytic performance was first evaluated by hydrogenation of CAL. 3-TiO_2/Au/SBA-15 exhibits the best conversion of CAL (78%), and Au/SBA-15 shows 74% conversion of CAL. However, these two catalysts just show 20% and 24% selectivity of COL. 1-TiO_2/Au/SBA-15 shows 42% selectivity toward COL production. Addition of TiO_2 films onto Au/SBA-15 can improve the selectivity toward COL production, particularly 1, 2 and 4 ALD cycles (Figure 5.8 d and Figure 5.9). Generally, the reactivity and selectivity of the supported Au nanocatalysts are worse than Pt nanocatalysts. Au is less active than Pt for hydrogenation of CAL.

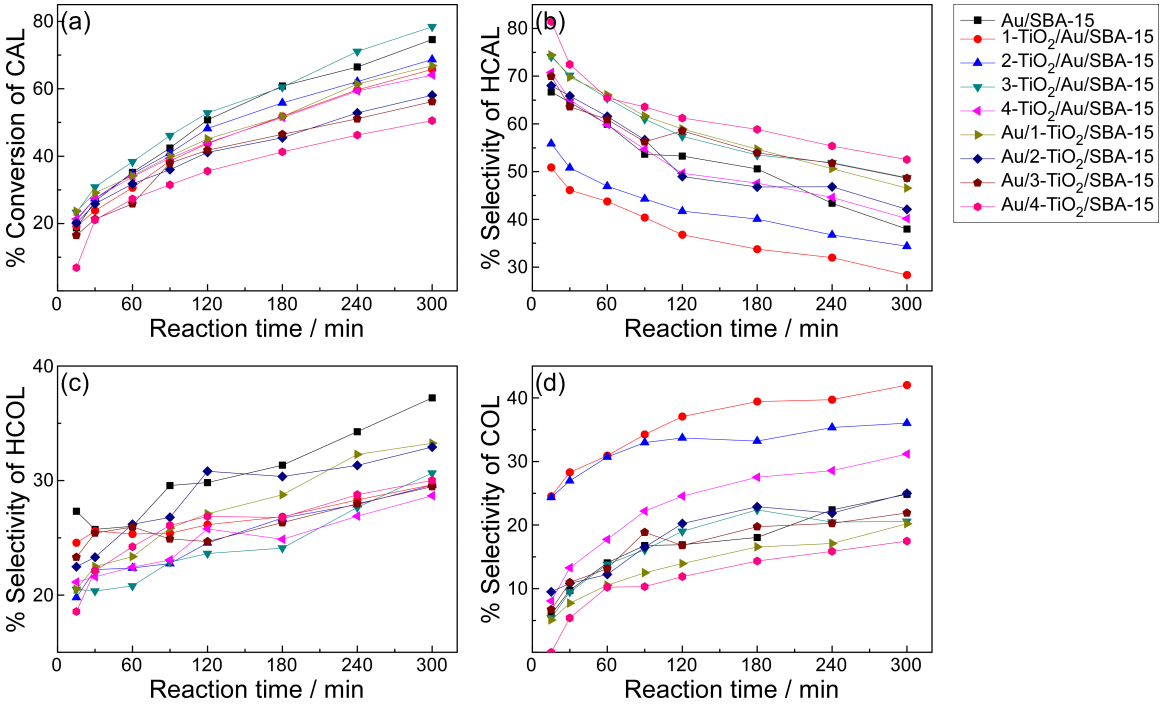

Figure 5.8 % Conversion of CAL (a), % selectivity of HCAL (b), HCOL (c), and COL (d) versus reaction time.

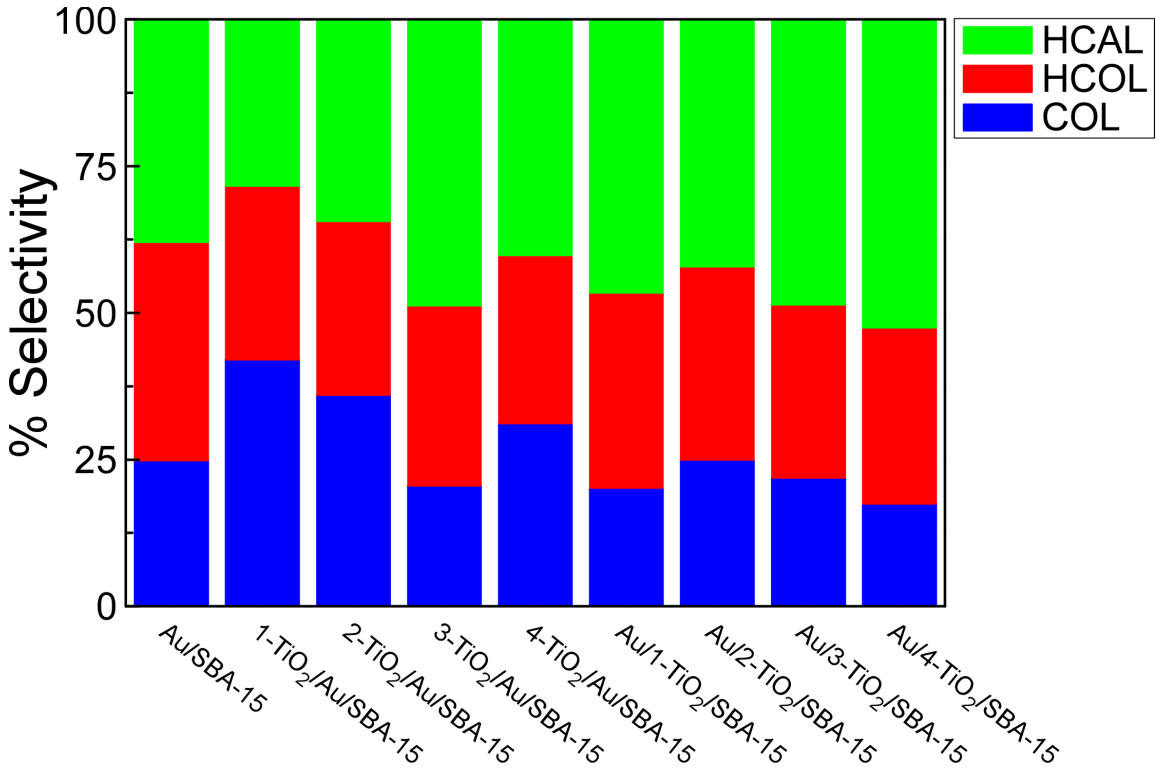

Figure 5.9 % Selectivity of HCAL, HCOL and COL of various catalysts at t=300 min.

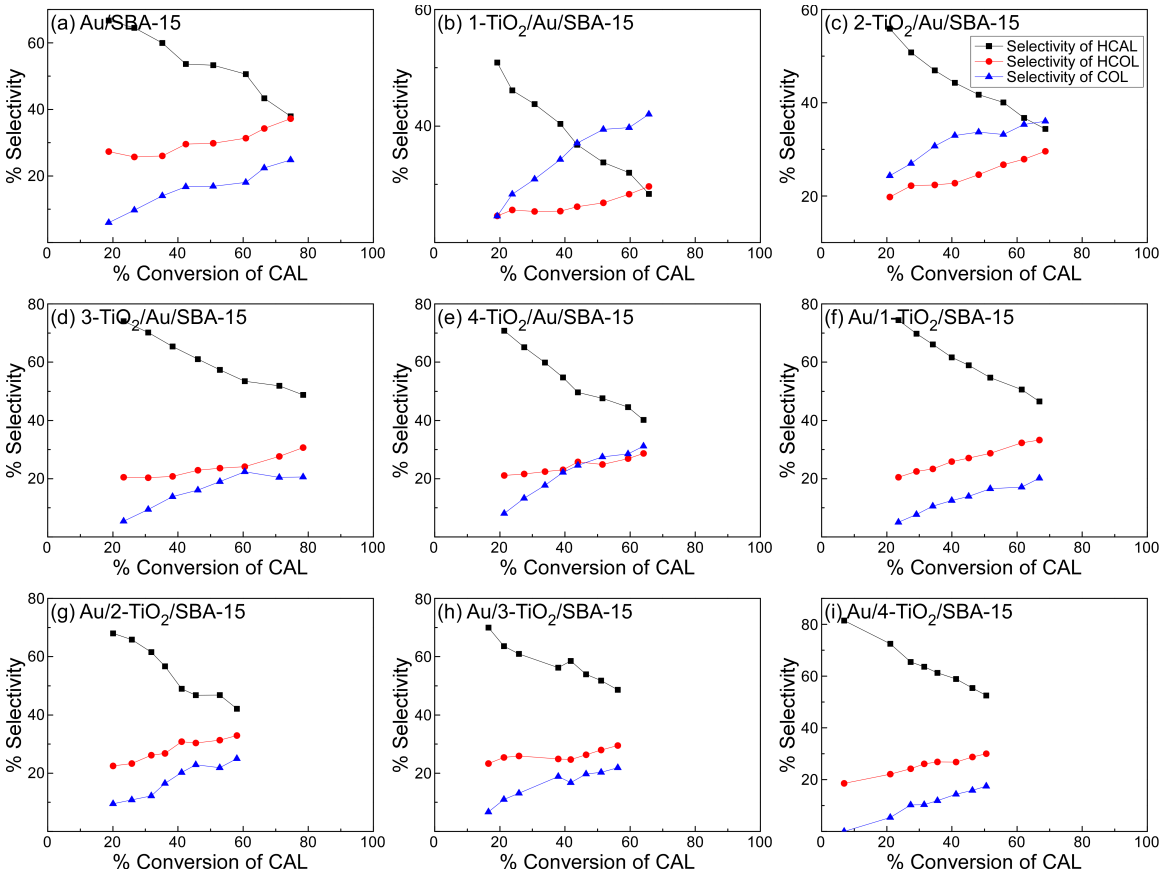

Figure 5.10 Selectivity versus conversion of various catalysts.

The selectivity toward three products versus conversion of CAL was plotted in Figure 5.10. The three products were all produced at the initial stages of the reaction. As the reaction was going on, selectivity toward HCAL was suppressed, and more COL and HCOL were produced. 1-TiO_2/Au/SBA-15 shows the best selectivity toward COL, and the selectivity toward HCAL and HCOL were greatly inhibited (Figure 5.10b).

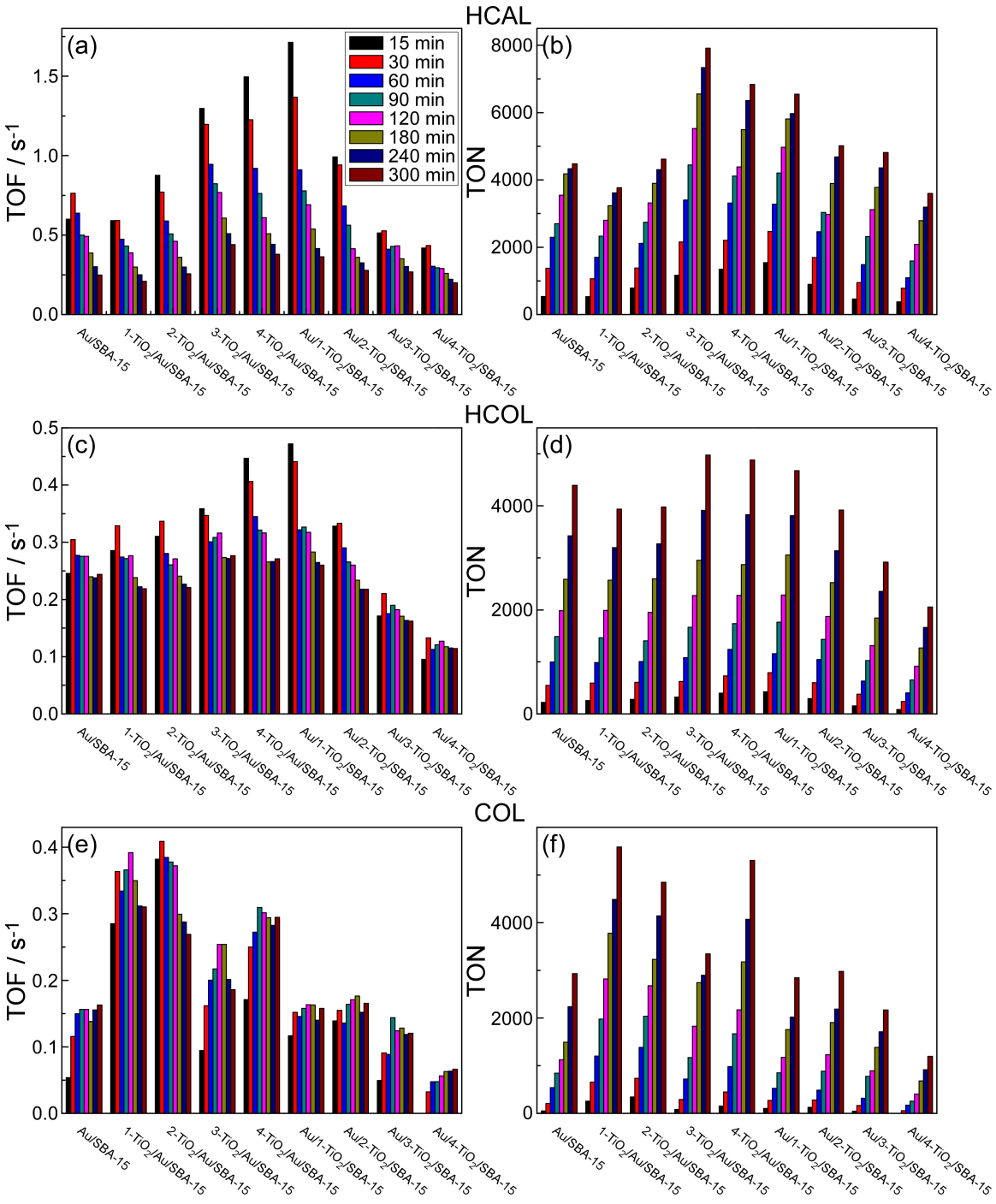

Figure 5.11 TOFs (a, c and e) and TONs (b, d and f) of HCAL, HCOL and COL for various catalysts as a function of reaction time.

It is more clear to see in Figure 5.11 e and f that (1-4)-TiO_2/Au/SBA-15 catalysts have better selectivity toward COL production than Au/SBA-15 and Au/(1-4)-TiO_2/SBA-15. However, 1-TiO_2/Au/SBA-15 just has 0.31 s^{-1} TOFs, which is much less than 1-TiO_2/Pt/SBA-15 (0.5 s^{-1}) at t=300 min.

5.3.3 Oxidation of benzyl alcohol

The catalytic performance was also evaluated by oxidation of benzyl alcohol. The desired product is benzaldehyde, and byproducts include benzoic acid, benzyl benzoate, etc. As shown in Figure 5.12, Au/SBA-15 shows the best conversion rate of benzyl alcohol. 91% of conversion could be achieved at t=360 min. It has to be mentioned that all the catalysts show 100% selectivity toward benzaldehyde production at t≤180 min. Therefore, if the reaction is stopped at 180 min, Au/SBA-15 should be the best catalyst with 56% conversion of benzyl alcohol and 100% selectivity toward benzaldehyde. The highest TOFs of 1.28 s^{-1} of benzaldehyde was achieved by Au/SBA-15 at t=60 min. Au/TiO_2 (sol-gel) and commercial Au/TiO_2 (anatase) show 100% selectivity toward benzaldehyde, but relatively low conversion, because the reactivity of these reference samples is low. At t=360 min, Au/SBA-15, (1-4)-TiO_2/Au/SBA-15 and Au/(1-4)-TiO_2/SBA-15 all produce byproducts, in which benzoic acid is the major one, but they cannot be separated. It appears that the addition of TiO_2 films does not improve the catalytic performance. Particularly, the differences of selectivity of all the catalysts are little.

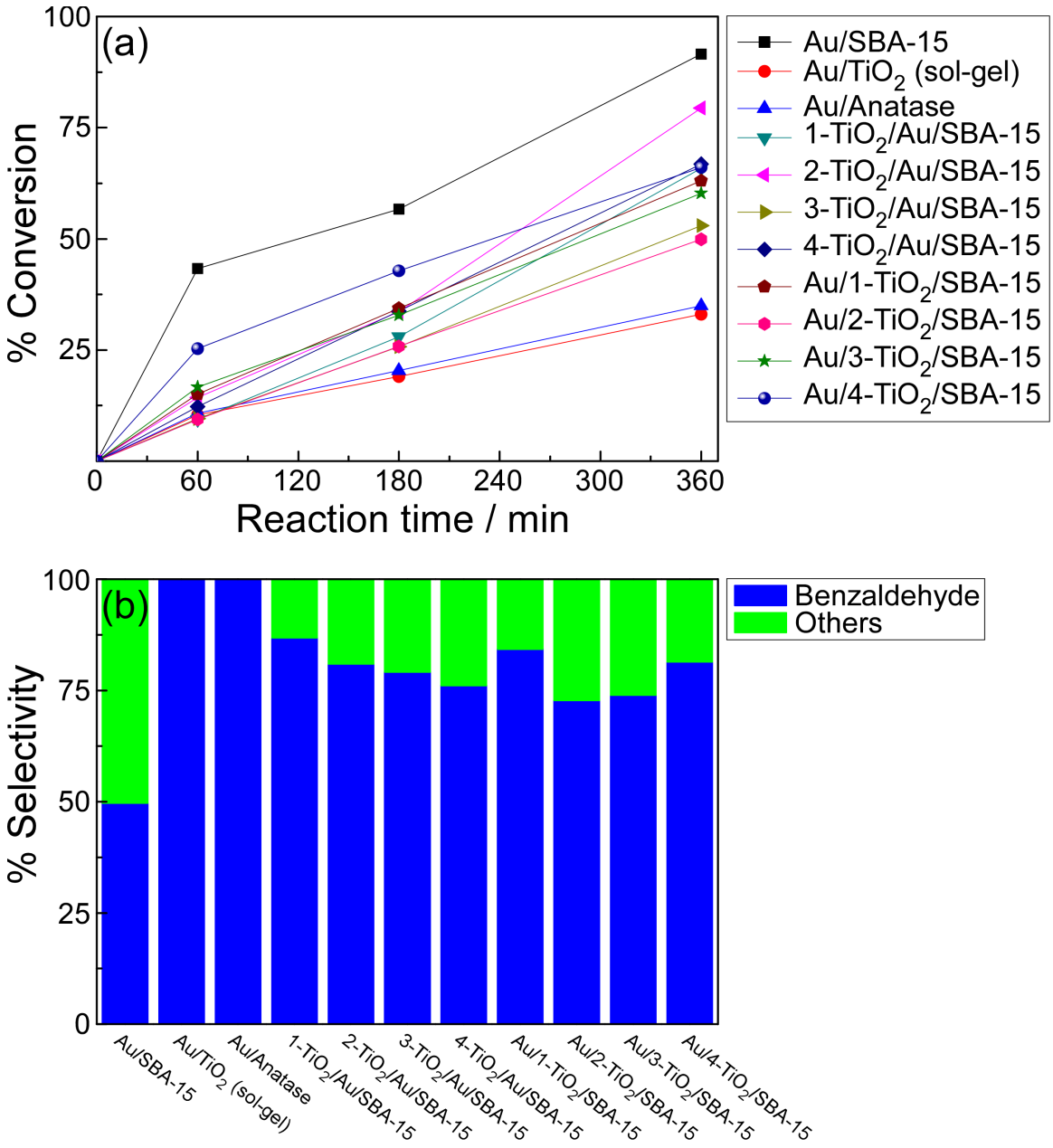

Figure 5.12 (a) % Conversion of benzyl alcohol versus reaction time. (b) % Selectivity of benzaldehyde at t=360 min.

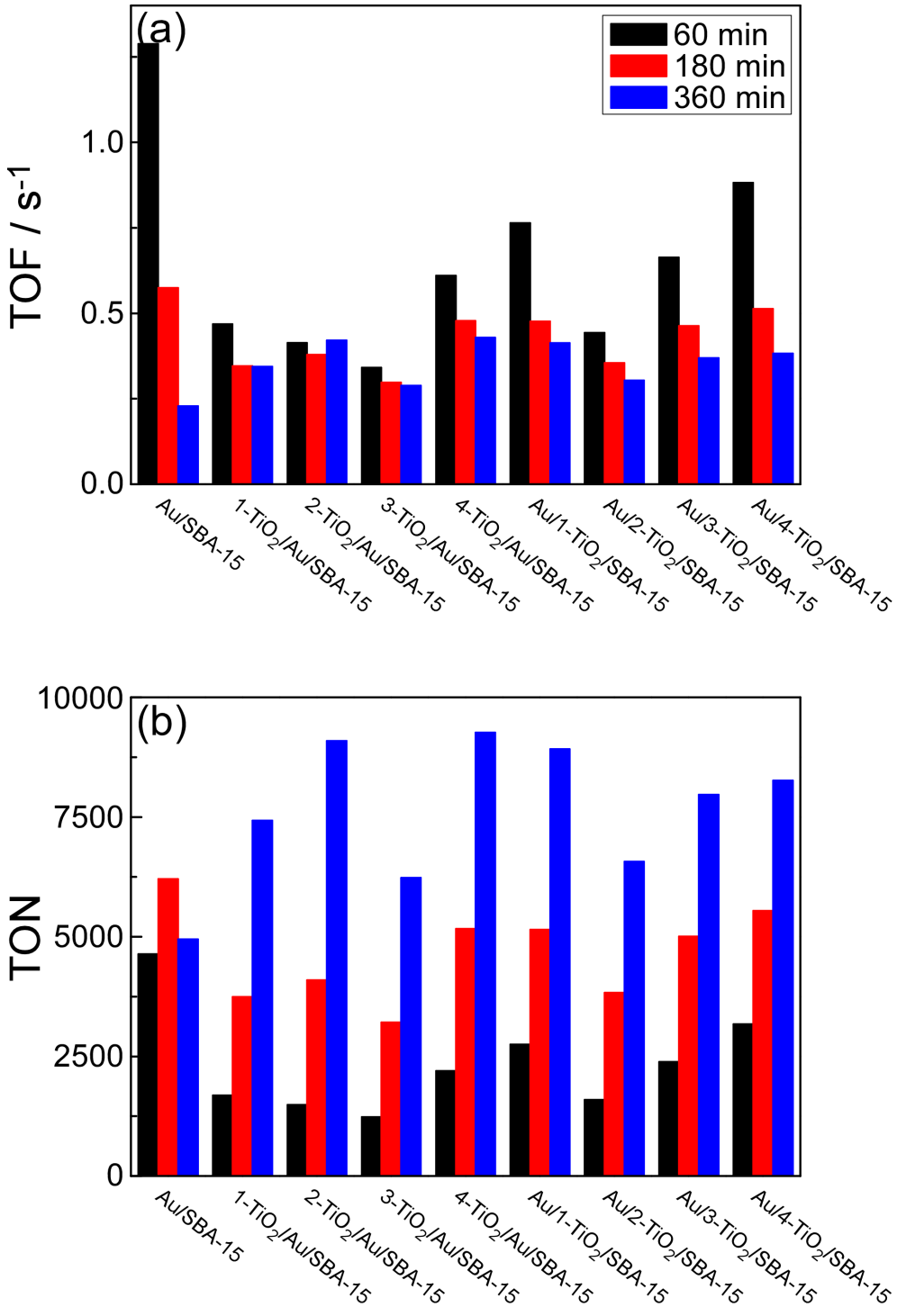

Figure 5.13 (a) TOFs and (b) TONs of benzaldehyde.

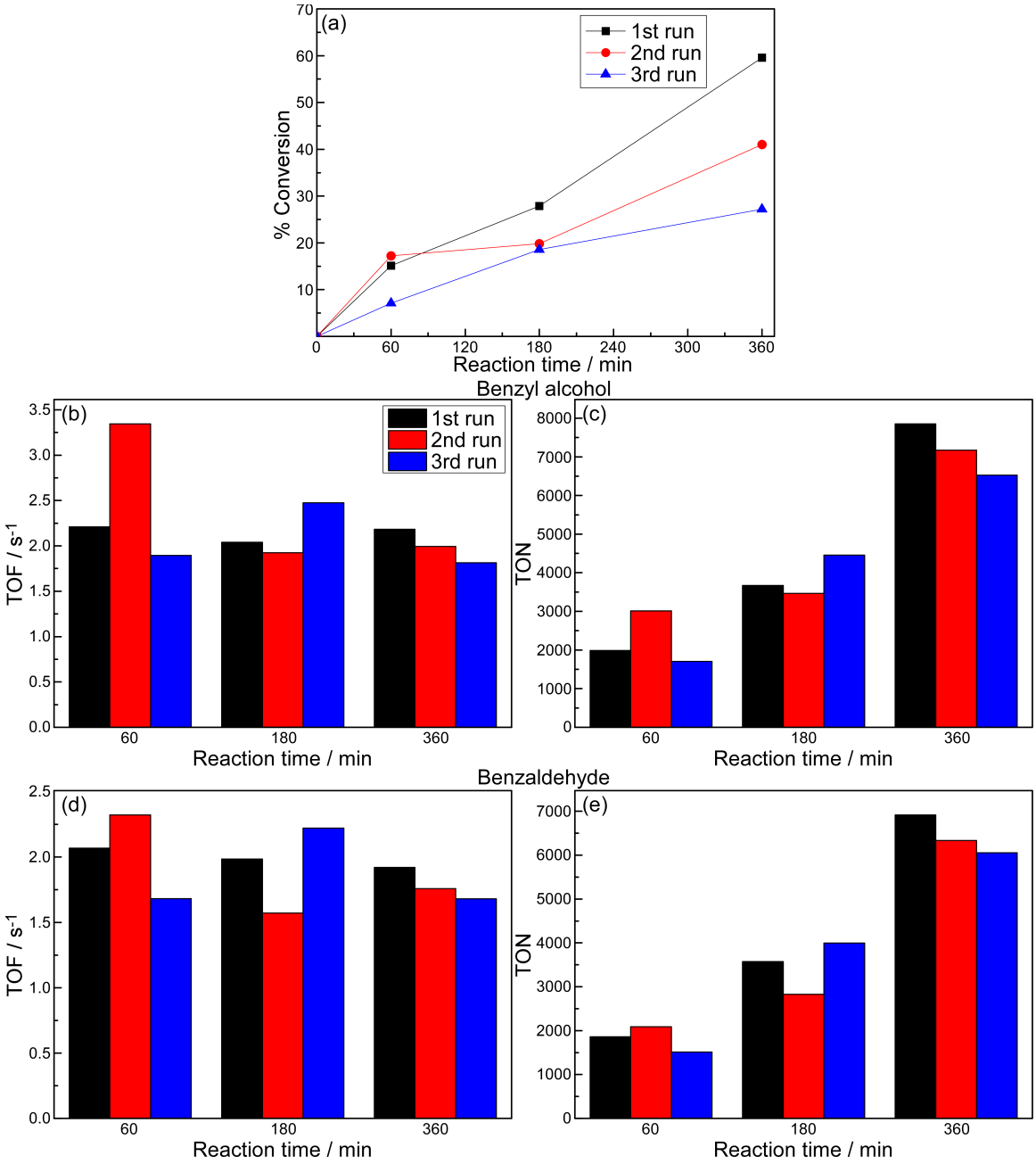

Figure 5.14 (a) % Conversion of benzyl alcohol. TOFs and TONs of benzyl alcohol (b, c) and benzaldehyde (d, e) versus reaction time of Au/4-TiO_2/SBA-15 for 3 catalytic runs.

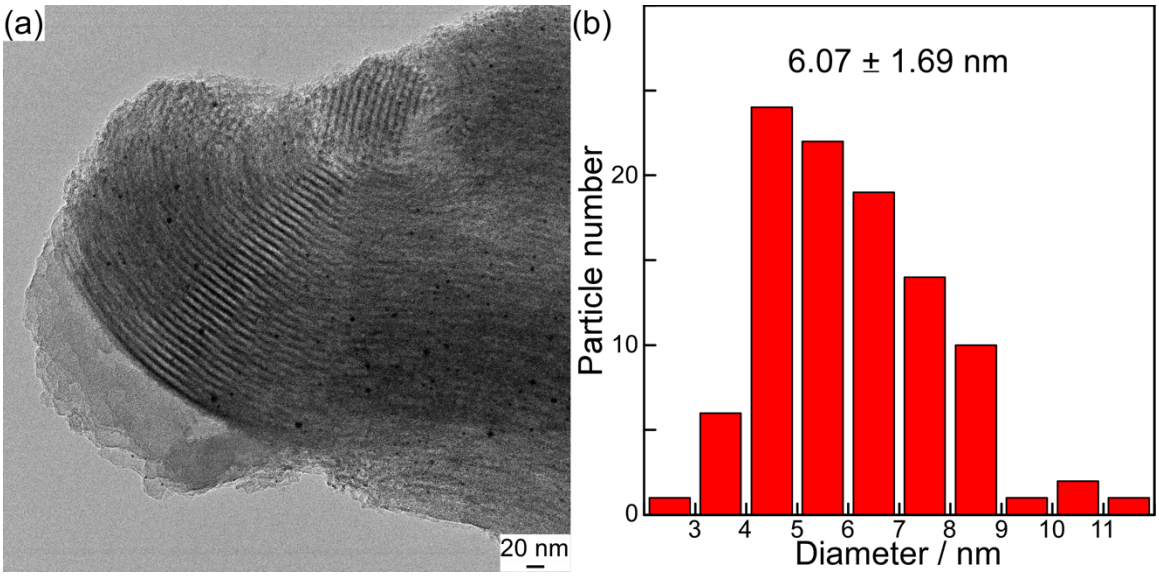

Figure 5.15 (a) TEM image. (b) Au nanoparticle size distributions of Au/4-TiO_2/SBA-15 after 3 catalytic runs.

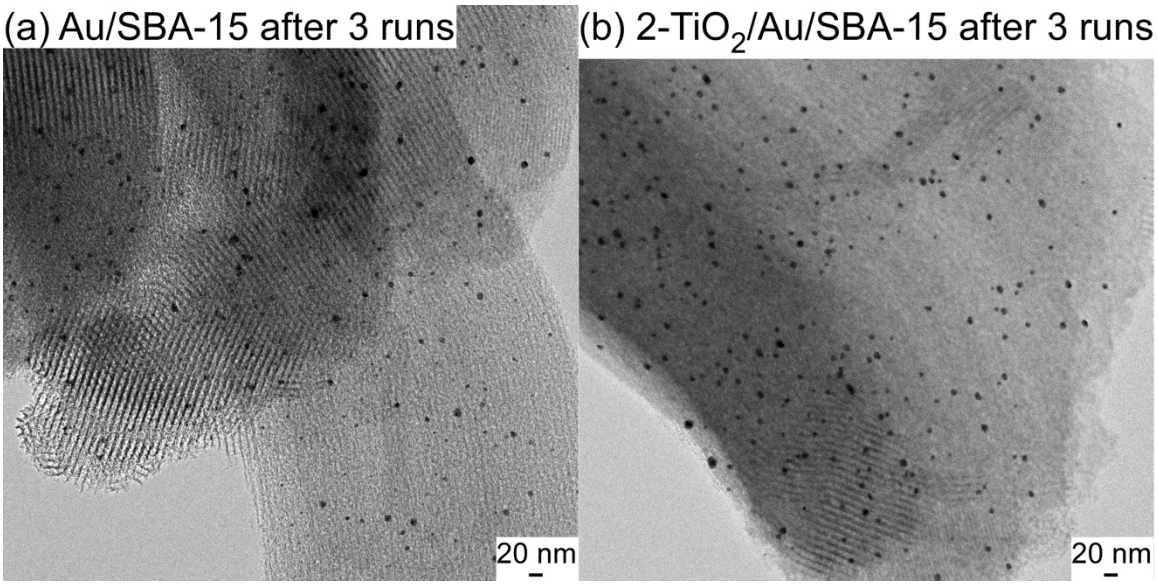

Figure 5.16 TEM images of (a) Au/SBA-15 and (b) 2-TiO_2/Au/SBA-15 after 3 catalytic runs.

The Au/4-TiO_2/SBA-15 was selected to test the reusability by running the reaction for 3 times continuously. The conversion reduction as a function of catalytic runs (Figure 5.14a) was mainly due to the loss of catalyst (~4.4 mg each run). As seen in Figure 5.14b to e, the TOFs and TONs almost remain at the same values after 3 catalytic runs, and even increase a little for the second run at 60 min. TEM images verify that the Au nanoparticles are stable and do not sinter after 3 catalytic runs. The diameter of Au nanoparticles is approximately 6.07 nm after 3 catalytic runs. Diameter fluctuation, compared with Figure 5.4 h, is because that the catalysts were prepared from different batches.

Au/SBA-15 and 2-TiO_2/Au/SBA-15 were also tested for reusability, but just for 240 min each run. The TEM images (Fig. 5.16) show that the Au nanoparticles are still stable and well-dispersed in the pores of SBA-15.

The kinetic data and TEM images confirm that the supported Au nanocatalysts also show remarkable stability. The encapsulation of Au nanoparticles inside the pores of SBA-15 and the ALD-TiO_2 films indeed improve the stability of the catalyst and prevent sintering of the Au nanoparticles.

5.3.4 Size control of Au nanoparticle

Oxidation reactions are generally considered to take place at the perimeter interface between the Au nanoparticles and support. The TOFs sharply increased when the diameter of Au nanoparticles decreased from 5 nm to 2 nm[82]. Therefore, it is critical to decrease the Au nanoparticle size to maximize the active sites.

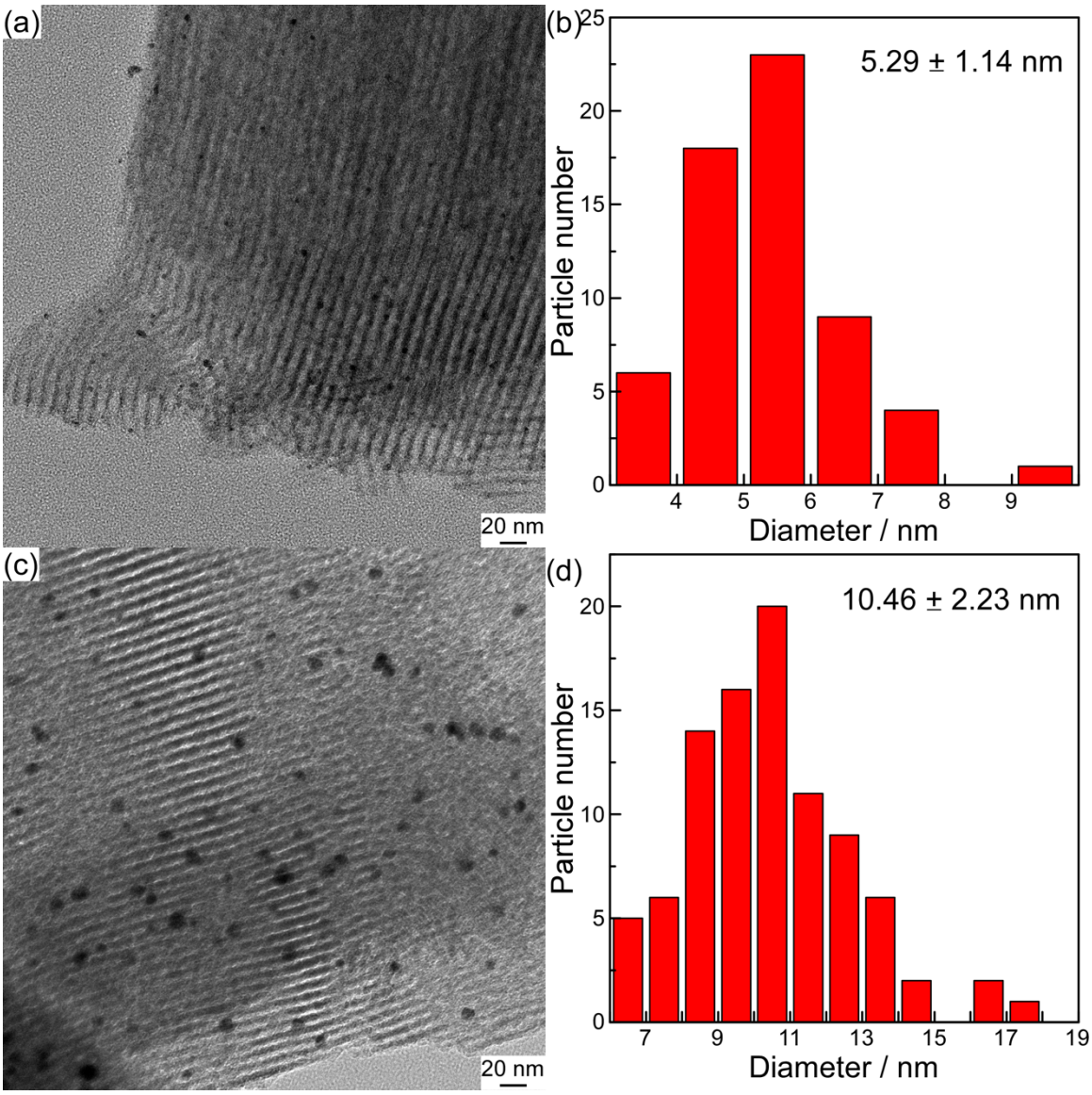

Figure 5.17 TEM images and Au nanoparticle size distributions of Au/SBA-15 functionalized with APTES (a, b) and reduced by $NaBH_4$ (c, d)

We tried to functionalize SBA-15 with APTES before depositing Au nanoparticles or reduce $[Au(en)_2]^{3+}$ with a stronger reducing agent – $NaBH_4$. However, it seems that both methods are not successful. The Au diameter of Au/SBA-15 functionalized with APTES is approximately 5.29 nm (Figure 5.17a and b), and the Au diameter of Au/SBA-15 reduced by $NaBH_4$ is approximately 10.46 nm (Figure 5.17c and d).

5.4 Conclusions

Supported Au nanocatalysts were successfully synthesized using $Au(en)_2Cl_3$ precursor. This method is effective for SBA-15 support, but less effective for TiO_2 modified SBA-15 support. The Au nanoparticle size of Au/(1-4)-TiO_2/SBA-15 is slightly larger than other catalysts. The Au nanoparticles were uniformly dispersed and incorporated in the pores of SBA-15.

The CO adsorption on Au is much weaker than on Pt, as the desorption temperatures are over 100 ^oC lower. The IR signals located at approximately 2187, 2171 and 2070-2150 cm^{-1} are assigned to CO adsorption on TiO_2, OH groups and Au nanoparticles, respectively. The peak intensities decrease as a function of temperature. The CO desorption on Au nanoparticles is complicated, since the two peaks between 2070 and 2150 cm^{-1} are associated with CO adsorption on Au^0 and $Au^{\delta+}$.

The ICP-OES results verify that the measured Au loadings are consistent with the nominal values, and TiO_2 loadings are very close to the values in Chapter 3 and 4.

The catalytic performance was investigated by hydrogenation of CAL and oxidation of benzyl alcohol. Similar to Pt nanocatalysts, the addition of TiO_2 films improves the

selectivity toward COL production. However, the overall reactivity and selectivity of Au are worse than Pt nanocatalysts. For oxidation reaction, all the catalysts show 100% selectivity toward benzaldehyde production at t=180 min. All the catalysts behave similarly for the benzyl alcohol oxidation reaction. Although the addition of TiO_2 films does not enhance the reactivity and selectivity, the stability of the supported Au nanocatalysts is still good.

Chapter 6 Conclusions and future works

6.1 Conclusions

In this work, amorphous TiO_2 films were deposited onto mesoporous SBA-5 support via ALD. The pore diameter decreases as a function of the number of ALD cycles, and the pore size distributions are sharp, indicating the layer-by-layer growth of the TiO_2 films. The film growth rate is approximately 1 Å per cycle. The mesoporous structure of SBA-15 is retained even after 10 ALD cycles. Furthermore, new acidic sites were created as probed by CO and pyridine IR absorption spectra, which is critical for the catalytic reactions. The as-prepared TiO_2 films are reducible, as demonstrated by EPR spectra, leading to SMSI effect and oxygen vacancies. NMR spectra indicate that the ALD process occurs preferentially at isolated silanol groups. The surface property of SBA-15 was modified by the TiO_2 films. The ALD process was well understood and we believe other oxide films, such as CeO_2, Al_2O_3, ZrO_2, etc. can be prepared by ALD and similar surface properties and catalytic performance can be obtained.

Then the Pt nanoparticles and TiO_2 films were deposited onto SBA-15 in two possible sequences. The Pt/SBA-15 was first synthesized using a PVP assisted colloidal method. PVP can be removed by calcination, and the Pt nanoparticles are still well-dispersed inside the pores of SBA-15. Subsequently, the (1-4)-TiO_2/Pt/SBA-15 catalysts were synthesized by depositing TiO_2 films via ALD onto the as-prepared Pt/SBA-15 support. The Pt/(1-4)-TiO_2/SBA-15 catalysts were synthesized using a DP method. After the deposition of Pt and TiO_2 films, the geometrical structure of the support was not destroyed, and the Pt

nanoparticles were uniformly dispersed in the pores of SBA-15 and TiO_2/SBA-15. Moreover, CO molecules can adsorb on TiO_2 sites and Pt atop sites. The CO adsorption on TiO_2 is much weaker than on Pt. For (1-4)-TiO_2/Pt/SBA-15 catalysts, the peak intensities of CO adsorption on Pt decrease and peak intensities of CO adsorption on TiO_2 increase with increasing number of ALD cycles, because the Pt nanoparticles were partially covered by TiO_2 films. Since the Pt nanoparticles were not covered by TiO_2 films for Pt/(1-4)-TiO_2/SBA-15, these catalysts show stronger CO-Pt signal. Finally, the catalytic performance was evaluated by hydrogenation of CAL and CO oxidation. 94% of CAL conversion, 41% of COL selectivity at t=300 min, and 0.65 s^{-1} of TOF of COL at t=120 min can be achieved by 1-TiO_2/Pt/SBA-15 catalyst. The addition of TiO_2 films can improve the selectivity toward COL production, which is attributed to the creation of acidic sites and the changes of reactant adsorption modes. For CO oxidation, Pt/4-TiO_2/SBA-15 catalyst shows the highest TOF (5.7 s^{-1}) of CO_2 at t = 60 s. All the (1-4)-TiO_2/Pt/SBA-15 and Pt/(1-4)-TiO_2/SBA-15 catalysts show better reactivity than Pt/SBA-15. Oxygen vacancies created in the interface between the reducible TiO_2 films and Pt nanoparticles is responsible for the enhanced reactivity.

Finally, the supported Au nanocatalysts were prepared in the same way. A gold cationic complex precursor $[Au(en)_2]^{3+}$ was synthesized and used for the preparation of Au/SBA-15, (1-4)-TiO_2/Au/SBA-15 and Au/(1-4)-TiO_2/SBA-15 catalysts. The Au nanoparticles were well-dispersed and incorporated inside the pores of SBA-15 and TiO_2/SBA-15 support. The pore size distributions are sharp too, and pore diameter decreases linearly with increasing number of ALD cycles. Furthermore, CO adsorption on TiO_2 and Au can be

identified by IR absorption spectra. However, the CO-Au IR spectra are more complicated than CO-Pt. CO molecules probably adsorb on both Au^0 and $Au^{\delta+}$ sites, but further evidence is lacking. In addition, the catalytic performance was investigated by hydrogenation of CAL and oxidation of benzyl alcohol. Similar to Pt nanocatalysts, the addition of TiO_2 films improve the selectivity toward COL production. However, the Au nanocatalyts show relatively worse reactivity and selectivity than Pt nanocatalysts. 1-TiO_2/Au/SBA-15 catalyst exhibits 65% of CAL conversion and 42% of COL selectivity at t=300 min. For oxidation of benzyl alcohol, all the catalysts show 100% benzaldehyde selectivity at t=180 min. 56% conversion of benzyl alcohol and 100% selectivity of benzaldehyde at t=180 min, and 91% conversion of benzyl alcohol and 50% selectivity of benzaldehyde at t=360 min can be achieved by Au/SBA-15 catalyst. It appears that the addition of TiO_2 films does not enhance the catalytic performance for benzyl alcohol oxidation.

Moreover, the TiO_2 loadings measured by ICP-OES are in good agreement with each other set of TiO_2 coated samples, indicating excellent reproducibility of ALD experiment. The measured Pt or Au loadings are very close to the nominal values.

It is worth mentioning that the reusability of the supported Pt or Au nanocatalysts is remarkable. After 3 continuous catalytic runs, the nanoparticles are still well-dispersed in the pores of SBA-15. No visible morphology change and sintering of the nanoparticles are observed. The enhanced stability can be attributed to the encapsulation of noble metal nanoparticles inside the pores of SBA-15, and the immobilization of nanoparticles by TiO_2 films as well as the SMSI effect.

6.2 Future works

Compared with published papers, our catalysts do not show much better performance, especially supported Au nanocatalyst. For example, Zheng and co-workers prepared amines capped Pt_3Co catalyst for hydrogenation of CAL[83]. 95% selectivity toward COL production and 100% conversion of CAL can be achieved. Hutchings and co-workers employed Au-Pd/TiO_2 catalysts for oxidation of benzyl alcohol[47]. Very high TOFs (up to 75 s^{-1}), as well as 74.5 % of benzyl alcohol conversion and 91.6% of benzaldehyde selectivity at t=8 h, can be obtained. Therefore, more suitable catalytic reactions are needed. WGS reaction, gas-phase hydrogenation reactions, or other oxidation reactions might be good choices.

Since our catalysts are highly stable even after 500 ^oC calcination and recycling experiments, it is worth trying catalytic reactions which are carried out over 600 ^oC, such as dry reforming reaction[84], decomposition of ammonia[85], etc. It is promising that our catalysts would be stable and sintering-resistant under really high temperature conditions.

References

(1) Cuenya, B. R. Synthesis and Catalytic Properties of Metal Nanoparticles: Size, Shape, Support, Composition, and Oxidation State Effects. *Thin Solid Films* **2010**, *518* (12), 3127–3150.

(2) Moshfegh, A. Z. Nanoparticle Catalysts. *J. Phys. D. Appl. Phys.* **2009**, *42* (23), 233001.

(3) Centeno, M. A.; Reina, T. R.; Ivanova, S.; Laguna, O. H.; Odriozola, J. A. Au/CeO_2 Catalysts: Structure and CO Oxidation Activity. *Catalysts* **2016**, *6* (10), 158.

(4) Mitsudome, T.; Kaneda, K. Gold Nanoparticle Catalysts for Selective Hydrogenations. *Green Chem.* **2013**, *15* (10), 2636–2654.

(5) Narayanan, R. Recent Advances in Noble Metal Nanocatalysts for Suzuki and Heck Cross-Coupling Reactions. *Molecules* **2010**, *15* (4), 2124–2138.

(6) Roldan Cuenya, B.; Behafarid, F. Nanocatalysis: Size- and Shape-Dependent Chemisorption and Catalytic Reactivity. *Surf. Sci. Rep.* **2015**, *70* (2), 135–187.

(7) Zhao, J.; Jin, R. Heterogeneous Catalysis by Gold and Gold-Based Bimetal Nanoclusters. *Nano Today* **2018**, *18*, 86–102.

(8) Xu, D.; Lv, H.; Liu, B. Encapsulation of Metal Nanoparticle Catalysts Within Mesoporous Zeolites and Their Enhanced Catalytic Performances: A Review. *Front. Chem.* **2018**, *6*, 550.

(9) Davidson, M.; Ji, Y.; Leong, G. J.; Kovach, N. C.; Trewyn, B. G.; Richards, R. M. Hybrid Mesoporous Silica/Noble-Metal Nanoparticle Materials—Synthesis and Catalytic Applications. *ACS Appl. Nano Mater.* **2018**, *1* (9), 4386–4400.

(10) An, K.; Alayoglu, S.; Musselwhite, N.; Plamthottam, S.; Melaet, G.; Lindeman, A. E.; Somorjai, G. A. Enhanced CO Oxidation Rates at the Interface of Mesoporous Oxides and Pt Nanoparticles. *J. Am. Chem. Soc.* **2013**, *135* (44), 16689–16696.

(11) Rioux, R. M.; Song, H.; Hoefelmeyer, J. D.; Yang, P.; Somorjai, G. A. High-Surface-Area Catalyst Design: Synthesis, Characterization, and Reaction Studies of Platinum Nanoparticles in Mesoporous SBA-15 Silica. *J. Phys. Chem. B* **2005**, *109* (6), 2192–2202.

(12) Li, Y.; Zaera, F. Sensitivity of the Glycerol Oxidation Reaction to the Size and Shape of the Platinum Nanoparticles in Pt/SiO_2 Catalysts. *J. Catal.* **2015**, *326*, 116–126.

(13) Xie, C.; Niu, Z.; Kim, D.; Li, M.; Yang, P. Surface and Interface Control in Nanoparticle Catalysis. *Chem. Rev.* **2020**, *120* (2), 1184–1249.

(14) Chen, J.; Lim, B.; Lee, E. P.; Xia, Y. Shape-Controlled Synthesis of Platinum Nanocrystals for Catalytic and Electrocatalytic Applications. *Nano Today* **2009**, *4* (1), 81–95.

(15) Leong, G. J.; Schulze, M. C.; Strand, M. B.; Maloney, D.; Frisco, S. L.; Dinh, H. N.; Pivovar, B.; Richards, R. M. Shape-Directed Platinum Nanoparticle Synthesis: Nanoscale Design of Novel Catalysts. *Appl. Organomet. Chem.* **2014**, *28* (1), 1–17.

(16) Lee, I.; Joo, J. B.; Yin, Y.; Zaera, F. Au@Void@TiO_2 Yolk–Shell Nanostructures as Catalysts for the Promotion of Oxidation Reactions at Cryogenic Temperatures. *Surf. Sci.* **2016**, *648*, 150–155.

(17) Wang, G.; Cao, Y.; Zhang, Z.; Xu, J.; Lu, M.; Qian, G.; Duan, X.; Yuan, W.; Zhou, X. Surface Engineering and Kinetics Behaviors of Au/Uncalcined TS-1 Catalysts for Propylene Epoxidation with H_2 and O_2. *Ind. Eng. Chem. Res.* **2019**, *58* (37), 17300–17307.

(18) Zhu, Y.; Qian, H.; Drake, B. A.; Jin, R. Atomically Precise $Au_{25}(SR)_{18}$ Nanoparticles as Catalysts for the Selective Hydrogenation of α,β-Unsaturated Ketones and Aldehydes. *Angew. Chemie Int. Ed.* **2010**, *49* (7), 1295–1298.

(19) Tauster, S. J.; Fung, S. C.; Garten, R. L. Strong Metal-Support Interactions. Group 8 Noble Metals Supported on Titanium Dioxide. *J. Am. Chem. Soc.* **1978**, *100* (1), 170–175.

(20) Tauster, S. J. Strong Metal-Support Interactions. *Acc. Chem. Res.* **1987**, *20* (11), 389–394.

(21) Liu, J. (Jimmy). Advanced Electron Microscopy of Metal–Support Interactions in Supported Metal Catalysts. *ChemCatChem* **2011**, *3* (6), 934–948.

(22) Goodman, D. W. "Catalytically Active Au on Titania:" Yet Another Example of a Strong Metal Support Interaction (SMSI)? *Catal. Letters* **2005**, *99* (1), 1–4.

(23) Carrettin, S.; Concepción, P.; Corma, A.; López Nieto, J. M.; Puntes, V. F. Nanocrystalline CeO_2 Increases the Activity of Au for CO Oxidation by Two Orders of Magnitude. *Angew. Chemie Int. Ed.* **2004**, *43* (19), 2538–2540.

(24) Zanella, R.; Giorgio, S.; Shin, C.-H.; Henry, C. R.; Louis, C. Characterization and Reactivity in CO Oxidation of Gold Nanoparticles Supported on TiO_2 Prepared by Deposition-Precipitation with NaOH and Urea. *J. Catal.* **2004**, *222* (2), 357–367.

(25) Luengnaruemitchai, A.; Osuwan, S.; Gulari, E. Comparative Studies of Low-Temperature Water–Gas Shift Reaction over Pt/CeO_2, Au/CeO_2, and Au/Fe_2O_3 Catalysts. *Catal. Commun.* **2003**, *4* (5), 215–221.

(26) Panagiotopoulou, P.; Kondarides, D. I. Effect of Morphological Characteristics of TiO_2-Supported Noble Metal Catalysts on Their Activity for the Water–Gas Shift Reaction. *J. Catal.* **2004**, *225* (2), 327–336.

(27) Centi, G.; Iaquaniello, G.; Perathoner, S. Can We Afford to Waste Carbon Dioxide? Carbon Dioxide as a Valuable Source of Carbon for the Production of Light Olefins. *ChemSusChem* **2011**, *4* (9), 1265–1273.

(28) Rodriguez, J. A.; Ma, S.; Liu, P.; Hrbek, J.; Evans, J.; Pérez, M. Activity of CeO_x and TiO_x Nanoparticles Grown on Au(111) in the Water-Gas Shift Reaction. *Science (80-.).* **2007**, *318* (5857), 1757 LP – 1760.

(29) Zhang, J.; Medlin, J. W. Catalyst Design Using an Inverse Strategy: From Mechanistic Studies on Inverted Model Catalysts to Applications of Oxide-Coated Metal Nanoparticles. *Surf. Sci. Rep.* **2018**, *73* (4), 117–152.

(30) Wang, L.; Wang, L.; Meng, X.; Xiao, F.-S. New Strategies for the Preparation of Sinter-Resistant Metal-Nanoparticle-Based Catalysts. *Adv. Mater.* **2019**, *31* (50), 1901905.

(31) Lu, J.; Elam, J. W.; Stair, P. C. Synthesis and Stabilization of Supported Metal Catalysts by Atomic Layer Deposition. *Acc. Chem. Res.* **2013**, *46* (8), 1806–1815.

(32) Weng, Z.; Zaera, F. Sub-Monolayer Control of Mixed-Oxide Support Composition in Catalysts via Atomic Layer Deposition: Selective Hydrogenation of Cinnamaldehyde Promoted by (SiO_2-ALD)-Pt/Al_2O_3. *ACS Catal.* **2018**, *8* (9), 8513–8524.

(33) Lu, J.; Fu, B.; Kung, M. C.; Xiao, G.; Elam, J. W.; Kung, H. H.; Stair, P. C. Coking- and Sintering-Resistant Palladium Catalysts Achieved Through Atomic Layer Deposition. *Science (80-.).* **2012**, *335* (6073), 1205 LP – 1208.

(34) O'Neill, B. J.; Jackson, D. H. K.; Crisci, A. J.; Farberow, C. A.; Shi, F.; Alba-Rubio, A. C.; Lu, J.; Dietrich, P. J.; Gu, X.; Marshall, C. L.; Stair, P. C.; Elam, J. W.; Miller, J. T.; Ribeiro, F. H.; Voyles, P. M.; Greeley, J.; Mavrikakis, M.; Scott, S. L.; Kuech,

T. F.; Dumesic, J. A. Stabilization of Copper Catalysts for Liquid-Phase Reactions by Atomic Layer Deposition. *Angew. Chemie - Int. Ed.* **2013**, *52* (51), 13808–13812.

(35) George, S. M. Atomic Layer Deposition: An Overview. *Chem. Rev.* **2010**, *110* (1), 111–131.

(36) Niemelä, J.-P.; Marin, G.; Karppinen, M. Titanium Dioxide Thin Films by Atomic Layer Deposition: A Review. *Semicond. Sci. Technol.* **2017**, *32* (9), 93005.

(37) Johnson, R. W.; Hultqvist, A.; Bent, S. F. A Brief Review of Atomic Layer Deposition: From Fundamentals to Applications. *Mater. Today* **2014**, *17* (5), 236–246.

(38) González, M. D.; Salagre, P.; Mokaya, R.; Cesteros, Y. Tuning the Acidic and Textural Properties of Ordered Mesoporous Silicas for Their Application as Catalysts in the Etherification of Glycerol with Isobutene. *Catal. Today* **2014**, *227*, 171–178.

(39) Hensen, E. J. M.; Poduval, D. G.; Magusin, P. C. M. M.; Coumans, A. E.; van Veen, J. A. R. Formation of Acid Sites in Amorphous Silica-Alumina. *J. Catal.* **2010**, *269* (1), 201–218.

(40) Ungureanu, A.; Dragoi, B.; Hulea, V.; Cacciaguerra, T.; Meloni, D.; Solinas, V.; Dumitriu, E. Effect of Aluminium Incorporation by the "pH-Adjusting" Method on the Structural, Acidic and Catalytic Properties of Mesoporous SBA-15. *Microporous Mesoporous Mater.* **2012**, *163*, 51–64.

(41) Miikkulainen, V.; Leskelä, M.; Ritala, M.; Puurunen, R. L. Crystallinity of Inorganic Films Grown by Atomic Layer Deposition: Overview and General Trends. *J. Appl. Phys.* **2013**, *113* (2).

(42) Zhang, L.; Zhou, M.; Wang, A.; Zhang, T. Selective Hydrogenation over Supported Metal Catalysts: From Nanoparticles to Single Atoms. *Chem. Rev.* **2020**, *120* (2), 683–733.

(43) Wang, M.-M.; He, L.; Liu, Y.-M.; Cao, Y.; He, H.-Y.; Fan, K.-N. Gold Supported on Mesostructured Ceria as an Efficient Catalyst for the Chemoselective Hydrogenation of Carbonyl Compounds in Neat Water. *Green Chem.* **2011**, *13* (3), 602–607.

(44) Gutiérrez, V.; Nador, F.; Radivoy, G.; Volpe, M. A. Highly Selective Copper Nanoparticles for the Hydrogenation of α,β-Unsaturated Aldehydes in Liquid Phase. *Appl. Catal. A Gen.* **2013**, *464–465*, 109–115.

(45) Sharma, A. S.; Kaur, H.; Shah, D. Selective Oxidation of Alcohols by Supported Gold Nanoparticles: Recent Advances. *RSC Adv*. **2016**, *6* (34), 28688–28727.

(46) Vinod, C. P.; Wilson, K.; Lee, A. F. Recent Advances in the Heterogeneously Catalysed Aerobic Selective Oxidation of Alcohols. *J. Chem. Technol. Biotechnol.* **2011**, *86* (2), 161–171.

(47) Enache, D. I.; Edwards, J. K.; Landon, P.; Solsona-Espriu, B.; Carley, A. F.; Herzing, A. A.; Watanabe, M.; Kiely, C. J.; Knight, D. W.; Hutchings, G. J. Solvent-Free Oxidation of Primary Alcohols to Aldehydes Using Au-Pd/TiO_2 Catalysts. *Science (80-.).* **2006**, *311* (5759), 362 LP – 365.

(48) Mobley, J. K.; Crocker, M. Catalytic Oxidation of Alcohols to Carbonyl Compounds over Hydrotalcite and Hydrotalcite-Supported Catalysts. *RSC Adv*. **2015**, *5* (81), 65780–65797.

(49) Soubaihi, R. M. Al; Saoud, K. M.; Dutta, J. Critical Review of Low-Temperature CO Oxidation and Hysteresis Phenomenon on Heterogeneous Catalysts. *Catalysts* **2018**, *8* (12), 660.

(50) Xanthopoulou, G.; Novikov, A.; Knysh, Y.; Amosov, A. Nanocatalysts for Low-Temperature Oxidation of CO: Review. *Eurasian Chem. J.* **2015**, *17* (1 SE-Articles).

(51) Ishida, T.; Murayama, T.; Taketoshi, A.; Haruta, M. Importance of Size and Contact Structure of Gold Nanoparticles for the Genesis of Unique Catalytic Processes. *Chem. Rev.* **2020**, *120* (2), 464–525.

(52) Liu, K.; Wang, A.; Zhang, T. Recent Advances in Preferential Oxidation of CO Reaction over Platinum Group Metal Catalysts. *ACS Catal.* **2012**, *2* (6), 1165–1178.

(53) Lee, I.; Zaera, F. Catalytic Oxidation of Carbon Monoxide at Cryogenic Temperatures. *J. Catal.* **2014**, *319*, 155–162.

(54) Weng, Z.; Chen, Z.; Qin, X.; Zaera, F. Sub-Monolayer Control of the Growth of Oxide Films on Mesoporous Materials. *J. Mater. Chem. A* **2018**, *6* (36), 17548–17558.

(55) Zaera, F. Infrared Absorption Spectroscopy of Adsorbed CO: New Applications in Nanocatalysis for an Old Approach. *ChemCatChem* **2012**, *4* (10), 1525–1533.

(56) Piccolo, L.; Daly, H.; Valcarcel, A.; Meunier, F. C. Promotional Effect of H_2 on CO Oxidation over Au/TiO_2 Studied by Operando Infrared Spectroscopy. *Appl. Catal. B Environ.* **2009**, *86* (3), 190–195.

(57) Boccuzzi, F.; Chiorino, A.; Manzoli, M. FTIR Study of the Electronic Effects of CO Adsorbed on Gold Nanoparticles Supported on Titania. *Surf. Sci.* **2000**, *454–456*, 942–946.

(58) Zaki, M. I.; Hasan, M. A.; Al-Sagheer, F. A.; Pasupulety, L. In Situ FTIR Spectra of Pyridine Adsorbed on SiO_2–Al_2O_3, TiO_2, ZrO_2 and CeO_2: General Considerations for the Identification of Acid Sites on Surfaces of Finely Divided Metal Oxides. *Colloids Surfaces A Physicochem. Eng. Asp.* **2001**, *190* (3), 261–274.

(59) Ammari, F.; Lamotte, J.; Touroude, R. An Emergent Catalytic Material: Pt/ZnO Catalyst for Selective Hydrogenation of Crotonaldehyde. *J. Catal.* **2004**, *221* (1), 32–42.

(60) Weng, Z.; Zaera, F. Atomic Layer Deposition (ALD) as a Way to Prepare New Mixed-Oxide Catalyst Supports: The Case of Alumina Addition to Silica-Supported Platinum for the Selective Hydrogenation of Cinnamaldehyde. *Top. Catal.* **2019**, *62* (12), 838–848.

(61) Brunet-Bruneau, A.; Fisson, S.; Gallas, B.; Vuye, G.; Rivory, J. Optical Properties of Mixed TiO_2-SiO_2 Films, from Infrared to Ultraviolet. In *Proc.SPIE*; 1999; Vol. 3738.

(62) Ingo, G. M.; Dirè, S.; Babonneau, F. XPS Studies of SiO_2-TiO_2 Powders Prepared by Sol-Gel Process. *Appl. Surf. Sci.* **1993**, *70–71*, 230–234.

(63) Cattaneo, A. S.; Ferrara, C.; Villa, D. C.; Angioni, S.; Milanese, C.; Capsoni, D.; Grandi, S.; Mustarelli, P.; Allodi, V.; Mariotto, G.; Brutti, S.; Quartarone, E. SBA-15 Mesoporous Silica Highly Functionalized with Propylsulfonic Pendants: A Thorough Physico-Chemical Characterization. *Microporous Mesoporous Mater.* **2016**, *219*, 219–229.

(64) Luan, Z.; Fournier, J. A.; Wooten, J. B.; Miser, D. E. Preparation and Characterization of (3-Aminopropyl)Triethoxysilane-Modified Mesoporous SBA-15 Silica Molecular Sieves. *Microporous Mesoporous Mater.* **2005**, *83* (1), 150–158.

(65) Liu, A. M.; Hidajat, K.; Kawi, S.; Zhao, D. Y. A New Class of Hybrid Mesoporous Materials with Functionalized Organic Monolayers for Selective Adsorption of Heavy Metal Ions. *Chem. Commun.* **2000**, No. 13, 1145–1146.

(66) Liu, N.; Xu, M.; Yang, Y.; Zhang, S.; Zhang, J.; Wang, W.; Zheng, L.; Hong, S.; Wei, M. $Au^{\delta-}$–Ov–Ti^{3+} Interfacial Site: Catalytic Active Center toward Low-Temperature Water Gas Shift Reaction. *ACS Catal.* **2019**, *9* (4), 2707–2717.

(67) Tang, H.; Su, Y.; Zhang, B.; Lee, A. F.; Isaacs, M. A.; Wilson, K.; Li, L.; Ren, Y.; Huang, J.; Haruta, M.; Qiao, B.; Liu, X.; Jin, C.; Su, D.; Wang, J.; Zhang, T. Classical Strong Metal–Support Interactions between Gold Nanoparticles and Titanium Dioxide. *Sci. Adv.* **2017**, *3* (10), e1700231.

(68) Borodziński, A.; Bonarowska, M. Relation between Crystallite Size and Dispersion on Supported Metal Catalysts. *Langmuir* **1997**, *13* (21), 5613–5620.

(69) Bazin, P.; Saur, O.; Lavalley, J. C.; Daturi, M.; Blanchard, G. FT-IR Study of CO Adsorption on Pt/CeO_2: Characterisation and Structural Rearrangement of Small Pt Particles. *Phys. Chem. Chem. Phys.* **2005**, *7* (1), 187–194.

(70) Zhu, Y.; Zaera, F. Selectivity in the Catalytic Hydrogenation of Cinnamaldehyde Promoted by Pt/SiO_2 as a Function of Metal Nanoparticle Size. *Catal. Sci. Technol.* **2014**, *4* (4), 955–962.

(71) Lee, I.; Zhang, Q.; Ge, J.; Yin, Y.; Zaera, F. Encapsulation of Supported Pt Nanoparticles with Mesoporous Silica for Increased Catalyst Stability. *Nano Res.* **2011**, *4* (1), 115–123.

(72) Handjani, S.; Marceau, E.; Blanchard, J.; Krafft, J.-M.; Che, M.; Mäki-Arvela, P.; Kumar, N.; Wärnå, J.; Murzin, D. Y. Influence of the Support Composition and Acidity on the Catalytic Properties of Mesoporous SBA-15, Al-SBA-15, and Al_2O_3-Supported Pt Catalysts for Cinnamaldehyde Hydrogenation. *J. Catal.* **2011**, *282* (1), 228–236.

(73) Widmann, D.; Behm, R. J. Activation of Molecular Oxygen and the Nature of the Active Oxygen Species for CO Oxidation on Oxide Supported Au Catalysts. *Acc. Chem. Res.* **2014**, *47* (3), 740–749.

(74) Carrettin, S.; Hao, Y.; Aguilar-Guerrero, V.; Gates, B. C.; Trasobares, S.; Calvino, J. J.; Corma, A. Increasing the Number of Oxygen Vacancies on TiO_2 by Doping with Iron Increases the Activity of Supported Gold for CO Oxidation. *Chem. – A Eur. J.* **2007**, *13* (27), 7771–7779.

(75) Tsai, C.-H.; Xu, M.; Kunal, P.; Trewyn, B. G. Aerobic Oxidative Esterification of Primary Alcohols over Pd-Au Bimetallic Catalysts Supported on Mesoporous Silica Nanoparticles. *Catal. Today* **2018**, *306*, 81–88.

(76) Zhu, H.; Liang, C.; Yan, W.; Overbury, S. H.; Dai, S. Preparation of Highly Active Silica-Supported Au Catalysts for CO Oxidation by a Solution-Based Technique. *J. Phys. Chem. B* **2006**, *110* (22), 10842–10848.

(77) Liu, H.; Kozlov, A. I.; Kozlova, A. P.; Shido, T.; Asakura, K.; Iwasawa, Y. Active Oxygen Species and Mechanism for Low-Temperature CO Oxidation Reaction on a TiO_2-Supported Au Catalyst Prepared from $Au(PPh_3)(NO_3)$ and As-Precipitated Titanium Hydroxide. *J. Catal.* **1999**, *185* (2), 252–264.

(78) Wang, Y.; Widmann, D.; Heenemann, M.; Diemant, T.; Biskupek, J.; Schlögl, R.; Behm, R. J. The Role of Electronic Metal-Support Interactions and Its Temperature Dependence: CO Adsorption and CO Oxidation on Au/TiO_2 Catalysts in the Presence of TiO_2 Bulk Defects. *J. Catal.* **2017**, *354*, 46–60.

(79) Panayotov, D.; McEntee, M.; Burrows, S.; Driscoll, D.; Tang, W.; Neurock, M.; Morris, J. Infrared Studies of Propene and Propene Oxide Adsorption on Nanoparticulate Au/TiO_2. *Surf. Sci.* **2016**, *652*, 172–182.

(80) Guillemot, D.; Borovkov, V. Y.; Kazansky, V. B.; Polisset-Thfoin, M.; Fraissard, J. Surface Characterization of Au/HY by ^{129}Xe NMR and Diffuse Reflectance IR Spectroscopy of Adsorbed CO. Formation of Electron-Deficient Gold Particles inside HY Cavities. *J. Chem. Soc. Faraday Trans.* **1997**, *93* (19), 3587–3591.

(81) Tran-Thuy, T.-M.; Chen, C.-C.; Lin, S. D. Spectroscopic Studies of How Moisture Enhances CO Oxidation over Au/BN at Ambient Temperature. *ACS Catal.* **2017**, *7* (7), 4304–4312.

(82) Okumura, M.; Fujitani, T.; Huang, J.; Ishida, T. A Career in Catalysis: Masatake Haruta. *ACS Catal.* **2015**, *5* (8), 4699–4707.

(83) Wu, B.; Huang, H.; Yang, J.; Zheng, N.; Fu, G. Selective Hydrogenation of α,β-Unsaturated Aldehydes Catalyzed by Amine-Capped Platinum-Cobalt Nanocrystals. *Angew. Chemie Int. Ed.* **2012**, *51* (14), 3440–3443.

(84) Pakhare, D.; Spivey, J. A Review of Dry (CO_2) Reforming of Methane over Noble Metal Catalysts. *Chem. Soc. Rev.* **2014**, *43* (22), 7813–7837.

(85) Xie, P.; Yao, Y.; Huang, Z.; Liu, Z.; Zhang, J.; Li, T.; Wang, G.; Shahbazian-Yassar, R.; Hu, L.; Wang, C. Highly Efficient Decomposition of Ammonia Using High-Entropy Alloy Catalysts. *Nat. Commun.* **2019**, *10* (1), 4011.